

**University of Alberta**

**APPLICATION OF CFRP LAMINATES IN THE RETROFIT  
OF MASONRY DEEP BEAMS**

by

Zhangcheng Hao



A thesis submitted to the Faculty of Graduate Studies and Research  
in partial fulfillment of the requirements for the degree of

**MASTER OF SCIENCE**

In

**Structural Engineering**

**Department of Civil and Environmental Engineering**

**Edmonton, Alberta**

**Fall, 2007**



Library and  
Archives Canada

Bibliothèque et  
Archives Canada

Published Heritage  
Branch

Direction du  
Patrimoine de l'édition

395 Wellington Street  
Ottawa ON K1A 0N4  
Canada

395, rue Wellington  
Ottawa ON K1A 0N4  
Canada

*Your file* *Votre référence*  
*ISBN: 978-0-494-33253-5*  
*Our file* *Notre référence*  
*ISBN: 978-0-494-33253-5*

#### NOTICE:

The author has granted a non-exclusive license allowing Library and Archives Canada to reproduce, publish, archive, preserve, conserve, communicate to the public by telecommunication or on the Internet, loan, distribute and sell theses worldwide, for commercial or non-commercial purposes, in microform, paper, electronic and/or any other formats.

The author retains copyright ownership and moral rights in this thesis. Neither the thesis nor substantial extracts from it may be printed or otherwise reproduced without the author's permission.

#### AVIS:

L'auteur a accordé une licence non exclusive permettant à la Bibliothèque et Archives Canada de reproduire, publier, archiver, sauvegarder, conserver, transmettre au public par télécommunication ou par l'Internet, prêter, distribuer et vendre des thèses partout dans le monde, à des fins commerciales ou autres, sur support microforme, papier, électronique et/ou autres formats.

L'auteur conserve la propriété du droit d'auteur et des droits moraux qui protègent cette thèse. Ni la thèse ni des extraits substantiels de celle-ci ne doivent être imprimés ou autrement reproduits sans son autorisation.

---

In compliance with the Canadian Privacy Act some supporting forms may have been removed from this thesis.

Conformément à la loi canadienne sur la protection de la vie privée, quelques formulaires secondaires ont été enlevés de cette thèse.

While these forms may be included in the document page count, their removal does not represent any loss of content from the thesis.

Bien que ces formulaires aient inclus dans la pagination, il n'y aura aucun contenu manquant.

  
**Canada**

## ABSTRACT

It is often necessary to create openings in existing masonry walls, to allow for transport of people and/or cargo. The construction of lintels in existing masonry walls requires erecting a frame to support the intended lintel prior to removing the region below it. It is not possible to insert longitudinal or web reinforcement in such cases. Besides, it is desirable to have little or no disruption of traffic (pedestrian or otherwise) once the lintel is created.

In light of the above, the application of fibre reinforced polymers (FRP) (in this case, Carbon FRP plates) enables not only to retain but also augment the use of the existing masonry structure. It cuts costs both in time and in machinery. In the technique presented here, CFRP plates were bonded onto the surface of the masonry blocks to form a deep masonry beam without using any temporary supports that otherwise interfere in the functioning of the building. The flexural response of a deep masonry lintel strengthened with i) steel rebar and ii) externally bonded CFRP plates was investigated under 3-point quasi-static loading. The amount and layout of the steel reinforcement and the CFRP were varied to result in eight different configurations.

The test results were compared to examine whether the externally bonded CFRP plates are capable of being an alternative to steel rebars. The crack patterns and failure modes were further analyzed to study the effects of the test variables on the flexural and shear capacity as well as on the system ductility. In addition, this study will also improve our understanding of the behaviour of deep masonry beams under 3-point loads, and verify the validity of the Strut-and-Tie Model in fully grouted masonry specimens. Also, four mechanical models to predict the beam carrying capacity were discussed.

## ACKNOWLEDGEMENTS

The author would like to express his acknowledgements to Dr. Alaa Elwi, Dr. Roger Cheng and Dr. Vivek Bindiganavile for their academic support and active encouragement during the investigation.

This research was funded by Natural Sciences and Engineering Research Council (NSERC), the ISIS Canada (a Network of Centres of Excellence) and the University of Alberta. The author also acknowledges the donation of the CFRP plates from Sika Canada.

The assistance and technical support by laboratory technicians Richard Helfrich, Larry Burden and Sean Watt throughout the experimental program is also gratefully acknowledged.

In the end, the author would like to thank all the supports from his friends and his family members.

## TABLE OF CONTENTS

<b>1. INTRODUCTION .....</b>	<b>1</b>
1.1 Problem Statement.....	1
1.2 Objectives and Scope.....	2
1.3 Organization of the Thesis.....	3
<b>2. LITERATURE REVIEW .....</b>	<b>4</b>
2.1 Introduction.....	4
2.2 Strengthening Deep Beams with FRP.....	4
2.3 External Strengthening for Masonry Structures .....	6
2.4 Bond Between FRP and Cementitious Substrate.....	8
2.5 Summary.....	10
<b>3. EXPERIMENTAL PROGRAM .....</b>	<b>16</b>
3.1 Introduction.....	16
3.2 Material Properties for the Components of a Deep Masonry Beam.....	16
3.2.1 Individual Masonry Unit.....	16
3.2.2 Mortar .....	17
3.2.3 Grout .....	17
3.2.4 Masonry Assemblages .....	18
3.2.5 Carbon Fibre Reinforced Polymer (CFRP) plates .....	19
3.2.6 Carbon Fibre Reinforced Polymer Sheets.....	20
3.2.7 Steel Reinforcement.....	21
3.3 Test Specimens .....	21
3.3.1 Description.....	21
3.3.2 Specimen Details .....	22
3.4 Application of CFRP.....	24

3.4.1	CFRP Plates .....	24
3.4.2	CFRP Sheets .....	24
3.5	Test Set-Up .....	25
3.6	Instrumentation .....	27
3.7	Test Procedure .....	29
<b>4.</b>	<b>TEST RESULTS.....</b>	<b>56</b>
4.1	Introduction.....	56
4.2	Load-Displacement Response.....	56
4.2.1	Beam 1 (Control beam).....	56
4.2.2	Beam 2 (Reinforced with two No.15 steel rebars).....	57
4.2.3	Beam 3 (Reinforced with longitudinal and web steel rebars).....	58
4.2.4	Beam 4 (Strengthened with two CFRP plates of 100 mm width).....	59
4.2.5	Beam 5 (Strengthened with two pieces of 50mm wide CFRP plates).....	61
4.2.6	Beam 6 (Strengthened with two pieces of 50mm wide CFRP plates).....	62
4.2.7	Beam 7 (Strengthened with CFRP plates and steel reinforcement).....	63
4.2.8	Beam 8 (Strengthened with CFRP plates and sheets).....	64
4.3	Strain Behaviour .....	65
4.3.1	Beam 1 .....	66
4.3.2	Beam 2 .....	66
4.3.3	Beam 3 .....	67
4.3.4	Beam 4 .....	67
4.3.5	Beam 5 .....	68
4.3.6	Beam 6 .....	69
4.3.7	Beam 7 .....	69
4.3.8	Beam 8 .....	70
4.4	Crack Pattern and Failure modes .....	70

4.4.1	Beam 1 .....	71
4.4.2	Beam 2 .....	71
4.4.3	Beam 3 .....	72
4.4.4	Beam 4 .....	72
4.4.5	Beam 5 .....	73
4.4.6	Beam 6 .....	74
4.4.7	Beam 7 .....	74
4.4.8	Beam 8 .....	75
<b>5.</b>	<b>ANALYSIS AND DISCUSSION.....</b>	<b>101</b>
5.1	Introduction.....	101
5.2	Discussion of Test Results .....	101
5.2.1	Ultimate Strength.....	101
5.2.2	Ductility .....	102
5.2.3	Stiffness.....	103
5.2.4	Other comparisons .....	105
5.3	Behaviour of Masonry Deep Beams .....	105
5.4	Mechanical Model .....	106
5.4.1	Introduction.....	106
5.4.2	Load Capacity Prediction for Masonry Deep Beams .....	107
5.5	Conclusion .....	113
<b>6.</b>	<b>SUMMARY, CONCLUSIONS AND RECOMMENDATIONS.....</b>	<b>121</b>
6.1	Summary .....	121
6.2	Conclusions.....	121
6.3	Recommendations.....	123
	<b>REFERENCES.....</b>	<b>124</b>

## LIST OF TABLES

Table 3-1 Compressive Strength of Individual Masonry Unit.....	31
Table 3-2 Compressive Strength of Mortar Cubes .....	32
Table 3-3 Compressive Strength of Grout Prism.....	33
Table 3-4 Results of the Grouted Masonry Prism Test.....	34
Table 3-5 Test Results For CFRP Plates.....	35
Table 3-6 Material Properties of Steel Reinforcement Coupons .....	36
Table 5-1 Reinforcing Method and Anchorage Application for Specimens .....	115
Table 5-2 Comparison of Test Results.....	116
Table 5-3 Predictions for Load Capacity of Specimens .....	117

## LIST OF FIGURES

Figure 2-1 Sketch of the Testing Arrangement in the Laboratory.....	12
Figure 2-2 Layout of GFRP and CFRP for the Specimens (After Foster, 2005).....	13
Figure 2-3 GFRP Layout for the Specimens (After Kuzik, 1999).....	14
Figure 2-4 CFRP Layout for the Specimens (After Miao, 2005) .....	15
Figure 3-1 Layout of Strain Gauges on CFRP Plate Coupons.....	37
Figure 3-2 Test Behaviour of Sika S1012 Coupons .....	38
Figure 3-3 Test Behaviour of Sika S512 Coupons .....	38
Figure 3-4 Detail of Beam 2 .....	39
Figure 3-5 Detail of Beam 3 .....	39
Figure 3-6 Detail of Beam 4 .....	40
Figure 3-7 Detail of Beams 5 and 6.....	41
Figure 3-8 Detail of Beam 7 .....	42
Figure 3-9 Detail of Beam 8 .....	43
Figure 3-10 Test Set-up .....	44
Figure 3-11 Side View of Test Set-up .....	45
Figure 3-12 Anchorage System for CFRP.....	46
Figure 3-13 The Layout of LVDTs and Load Cells .....	47
Figure 3-14 The Layout of Demec Gauge Points .....	48
Figure 4-1 Load-Displacement of Beam 1.....	77
Figure 4-2 Load-Displacement of Beam 2.....	77
Figure 4-3 Load-Displacement of Beam 3.....	78
Figure 4-4 Load-Displacement of Beam 4.....	78
Figure 4-5 Load-Displacement of Beam 5.....	79
Figure 4-6 Load-Displacement of Beam 6.....	79
Figure 4-7 Load-Displacement of Beam 7.....	80
Figure 4-8 Load-Displacement of Beam 8.....	80
Figure 4-9 Load - Strain on Bottom Steel Reinforcement of Beam 2 .....	81
Figure 4-10 Load-Strain on Bottom Steel Reinforcement of Beam 3 .....	81
Figure 4-11 Load- Strain on CFRP Plates of Beam 4.....	82

Figure 4-12 Load-Strain on CFRP Plates of Beam 5.....	82
Figure 4-13 Load-Strain on CFRP Plates of Beam 6.....	83
Figure 4-14 Load-Strain on CFRP Plates of Beam 7.....	83
Figure 4-15 Load-Strain on CFRP Plates of Beam 8.....	84
Figure 5-1 Load-Midspan Displacement Curves for Beam 2, 4 , 5 and 6 .....	118
Figure 5-2 Load-Midspan Displacement For Beam 3, 7 and 8.....	118
Figure 5-3 Load-Midspan Displacement for Beam 1, 2 and 3 .....	119
Figure 5-4 Load-Midspan Displacement for Beam 4, 7 and 8 .....	119
Figure 5-5 Toughness of Specimens up to Peak Load.....	120

## LIST OF IMAGES

Image 3-1 Capped Individual Masonry Unit Specimens.....	49
Image 3-2 Construction of Grout Prism Specimens .....	49
Image 3-3 Test set-up for Grouted Masonry Prism .....	50
Image 3-4 Typical Failure Mode of Grouted Masonry Prisms.....	50
Image 3-5 Typical Failure Mode of CFRP Plate Coupon.....	51
Image 3-6 Loading Frame.....	51
Image 3-7 Top Loading System.....	52
Image 3-8 Bottom Reaction Assembled System .....	52
Image 3-9 Out-of-Plane Bracing System.....	53
Image 3-10 Anchorage System for CFRP Plates at Supports.....	54
Image 3-11 Test Set-up.....	55
Image 4-1 Crack Pattern of Beam 1.....	85
Image 4-2 Crack Pattern of Beam 2.....	85
Image 4-3 Spalling Area of Beam 2 .....	86
Image 4-4 Crack Pattern of Beam 3 at the Load of 400 kN .....	86
Image 4-5 Crack Pattern of Beam 3 at the load of 480 kN.....	87
Image 4-6 Crack Pattern of Beam 3 at Failure .....	87
Image 4-7 Contact Between the End of Beam 3 And South End Restraint.....	88
Image 4-8 Crushing at the Top Load Point for Beam 3.....	89
Image 4-9 Crack Pattern of Beam 4 at the Load of 300 kN .....	89
Image 4-10 Crack Pattern of Beam 4 at the Load of 500 kN .....	90
Image 4-11 Crack Pattern of Beam 4 at Failure .....	90
Image 4-12 Debonding Between CFRP Plate and Masonry Surface of Beam 4.....	91
Image 4-13 Crack Pattern of Beam 5 at the Load of 150 kN .....	91
Image 4-14 Crack Pattern of Beam 5 at Failure .....	92
Image 4-15 Peeling off at the End of Beam 5.....	92
Image 4-16 Debonding at the Mid-span of Beam 5.....	93
Image 4-17 Crack Pattern of Beam 6 at the Load of 150 kN .....	93
Image 4-18 Crack Pattern of Beam 6 at the Load of 350 kN .....	94

Image 4-19 Crack Pattern of Beam 6 at Failure .....	94
Image 4-20 Peeling off at the End of Beam 6.....	95
Image 4-21 Crack Pattern of Beam 7 at the load of 300 kN.....	95
Image 4-22 Crack Pattern of Beam 7 at the Load of 450 kN .....	96
Image 4-23 Crack Pattern of Beam 7 at the Load of 650 kN .....	96
Image 4-24 Crack Pattern of Beam 7 at Failure .....	97
Image 4-25 Peeling off at the End of Beam 7.....	97
Image 4-26 Crack Pattern of Beam 8 at the Load of 250 kN .....	98
Image 4-27 Crack Pattern of Beam 8 at the Load of 300 kN .....	98
Image 4-28 Crack Pattern of Beam 8 at the Load of 450 kN .....	99
Image 4-29 Crack Pattern of Beam 8 at the Load of 550 kN .....	99
Image 4-30 Crack Pattern of Beam 8 at Failure .....	100

## LIST OF ABBREVIATIONS AND SYMBOLS

### Abbreviation

ASTM	American Society for Testing and Materials
ACI	American Concrete Institute
ASCE	American Society of Civil Engineers
CFRP	Carbon Fibre Reinforced Polymer
CSA	Canadian Standards Association
GFRP	Glass Fibre Reinforced Polymer
FRP	Fibre Reinforced Polymer
HSS	Hollow Structural Section
kN	Kilo Newton
LVDT	Linear Variable Differential Transformer
m	Meter
mm	Millimeter
MPa	Mega Pascal
MTS	Material Testing System
N	Newton
W	Wide Flange Beam Designation
URM	Unreinforced Masonry

## Symbols

$a$	= shear span length, (mm)
$A_{cs}$	= effective cross-sectional area of concrete strut, ( $\text{mm}^2$ )
$A_{ct}$	= area of concrete section along diagonal strut, ( $\text{mm}^2$ )
$A_s$	= area of longitudinal tension bars, ( $\text{mm}^2$ )
$A_{st}$	= area of reinforcement in tension tie, ( $\text{mm}^2$ )
$A_{str}$	= cross-sectional area of the diagonal strut, ( $\text{mm}^2$ )
$A_v$	= cross-sectional area of web reinforcement, ( $\text{mm}^2$ )
$A_w$	= area of web reinforcement, ( $\text{mm}^2$ )
$b_w$	= web width of beam, (mm)
$d$	= distance from extreme compression fiber to centroid of tension, (mm)
$d_w$	= distance from beam top to intersection of web reinforcement with line connecting support center and load center (mm)
$E_c$	= calculated modulus of elasticity of coupon CFRP composite, (MPa)
$E_s$	= modulus of elasticity of steel bars, (MPa)
$f_c'$	= concrete cylinder strength, (MPa)
$f_{ct}$	= concrete tensile stress
$f_{cu}$	= compressive stress of strut, (MPa)
$f_m'$	= compressive strength of masonry, (MPa)
$f_y$	= yield stress of steel reinforcement, (MPa)
$f_{yh}$	= yield stress of horizontal steel reinforcement, (MPa)
$f_{yv}$	= yield stress of vertical steel reinforcement, (MPa)
$f_{yw}$	= yield strength of web reinforcement, Mpa
$l_c$	= height of top node, (mm)
$n$	= the ratio of steel to concrete elastic moduli
$s$	= spacing of shear reinforcement measured parallel to the longitudinal axis of the member, (mm)
$V_r$	= shear resistance, (kN)
$V_{dc}$	= strut capacity against diagonal crushing of concrete
$V_{ds}$	= resistance of inclined strut to diagonal splitting, (kN)
$V_m$	= shear strength contributed by masonry, (kN)
$V_n$	= predicted nominal shear strength, (kN)
$V_s$	= shear resistance of shear reinforcement, (kN)

$z_s$	= lever arm of $T_s$ to center of concrete stress block at top load point, (mm)
$\epsilon_s$	= tension strain in tension tie
$\Phi_m$	= resistance factor for masonry
$\Phi_c$	= resistance factor for concrete
$\rho_h$	= horizontal web reinforcement ratio
$\rho_v$	= vertical web reinforcement ratio
$\rho_f$	= longitudinal reinforcement ratio
$\lambda$	= factor to account for low density concrete masonry units
$\theta_s$	= smallest angle between the compressive strut and the adjoining tensile ties
$\theta_w$	= angle between web reinforcement and horizontal axis of beams at intersection of reinforcement and diagonal strut

# 1. INTRODUCTION

## 1.1 Problem Statement

Masonry, using stone blocks, earthen bricks or concrete blocks, has been the principal construction practice for almost ten millennia. Therefore, these buildings have formed an important connection with the history of civilization. Along with the progress of society and the development of economy, many old buildings require to be repaired and retrofitted to adapt to their current multipurpose use. Furthermore, as labour and construction costs go up, more and more building owners are inclined towards retrofitting the existing buildings so as to reduce their financial burden. Often it is necessary to change the internal layout or external walls of the building in order to satisfy particular requirement.

One of the familiar techniques required in masonry structures is to make a large opening on an existing load bearing masonry wall so that large amounts of cargo or pieces of equipment can be conveyed. Whereby, the lintel over the opening needs to be strengthened for the sake of carrying the load from the wall above.

In conventional design, a steel or reinforced concrete beam can be put over the opening to become a lintel. However, the increase in the weight, intensive labour during application and the subsequent maintenance due to corrosion of the steel material may eventually increase the overall cost. Besides, installation of beams on an existing masonry wall may cause cracks. Thus, a related research need arises in order to find an alternate method for the conventional solution.

The research on Fibre Reinforced Polymer (FRP) used in construction retrofit is the most popular one, and has generated considerable worldwide interest. As an alternative to conventional retrofitting materials, FRP composites possess many attractive characteristics such as high strength-to-weight and stiffness-to-weight ratios, durability in adverse environments, impact resistance, ease in installation, perfect adaptability to the original shape of the structural element, low labour and low machinery costs. Based on recent research activity, Fibre Reinforced Polymers (FRP) have demonstrated remarkable characteristics to work with all kinds of structural members, such as bridges, tunnels,

pipelines, underwater structures and historic erections, and are known to significantly improve the strength, performance and durability of constructed facilities.

Recently, more and more studies regarding masonry members strengthened with FRP composites have been carried out. However, there is very little available information related to strengthening masonry deep beams with FRP materials. Thus, a study for externally strengthening masonry deep lintels shall be brought forward to satisfy the specific retrofitting requirement on the existing masonry buildings.

This research is to verify if FRP sheets are capable of replacing steel to externally strengthen the masonry lintels. By virtue of this method, FRP sheets can be simply bonded onto the surface of the masonry blocks to form a deep masonry beam without using any temporary supports that otherwise interfere with the functioning of the building. Although the fibres and resins used in FRP systems are relatively expensive compared with traditional materials like steel and concrete, labour and equipment costs associated with the installation of FRP sheets are normally lower. Moreover, such a system makes little change to the original appearance since the FRP sheets is very thin.

## **1.2 Objectives and Scope**

The broad objective of this research was to investigate the flexural response of a deep masonry lintel strengthened with a) steel rebar and b) externally bonded CFRP (Carbon Fibre Reinforced Polymer) sheets under a 3-point quasi-static loading, and compares the test results to find out whether the externally bonded CFRP sheets are capable of being an alternative to steel rebar or not; The load–displacement response of the specimens was examined to study the effects of variables such as the amount and layout of steel reinforcement and CFRP on the flexural and shear capacity as well as on the system ductility. This research is intended to lead to an understanding of the behaviour of deep masonry beams under 3-point loads, and verify the validity of the Strut-and-Tie Model in fully grouted masonry specimens. In addition, the crack patterns and failure modes were identified during the test to allow for future optimization.

The scope of this research comprised of the testing and analysis of 8 full-scale fully grouted masonry deep beams strengthened with different materials such as internal steel

reinforcement and external bonded CFRP plates or fabric.

### **1.3 Organization of the Thesis**

Chapter 2 introduces a review of the related researches with regard to the cement-based beams strengthened with different materials.

Chapter 3 presents the testing program in this study. It contains the descriptions regarding the materials, the specimens, test set-up, instrumentation layout and testing procedures.

Chapter 4 describes the experimental observations and results, including the load-midspan displacement behaviour, strain behaviour, failure modes and crack patterns, for each reinforcing scheme.

In Chapter 5, an analysis of the test results is presented; the comparison between different specimens is conducted and several mechanical models are provided to predict the shear capacities of specimens.

Finally, in Chapter 6, the summary and conclusions of this study as well as some recommendations for further study are presented.

## 2. LITERATURE REVIEW

### 2.1 Introduction

The use of FRP composites in concrete started in 1985, and several studies exist (Saadatmanesh *et al.* 1991, Ritchie *et al.* 1991, Daniali *et al.* 1994, Toutanil *et al.* 1998, Tavakkolizadeh *et al.* 2003, etc.) on applying the FRP to concrete structures such as beams, columns and slabs. Of late, investigating the use of FRP for rehabilitation of masonry structures has evoked great interest, in particular, the use of FRP laminates to improve the in-plane shear capacity and out-of-plane resistance of masonry walls. However, little attention has been paid to the research on retrofitting the masonry lintel by using FRP laminates. This chapter will review the related studies carried out.

### 2.2 Strengthening Deep Beams with FRP

Based on the author's knowledge, there is no research related to retrofit of masonry deep beams so far. Whereas, the studies regarding the retrofit of reinforced concrete deep beams have been carried out for a long time. These studies have built the basis for commencing research in masonry structures although the difference between the two material responses, i.e. that of concrete and masonry, is to be expected in the structural response.

Zhang *et al.* (2004) studied the effect of externally bonded reinforcement such as carbon fiber reinforced polymer laminates on reinforced concrete deep beams with shear deficiencies. Sixteen deep beams without steel shear reinforcement were built to investigate the shear behavior of deep beams. All beams were strengthened externally with CFRP laminates at various orientations except for reference beams and tested under different loading conditions.

The shear span to effective depth ratio ( $a/d$ ) effect on shear strengthening of deep beams using CFRP laminates was studied. When  $a/d$  decreased, the shear strength of the beam was found to increase and the shear contribution of CFRP laminates varied depending on the CFRP configuration. Meanwhile, the shear behavior and modes of failure of the concrete deep beams were investigated after reinforcing with CFRP laminates. Three

kinds of failure modes were proposed and discussed: 1) “Shear-tension” failure, which was due to the sliding between CFRP laminates and concrete substrate; 2) “Diagonal-tension” failure, which was caused by the propagation of an inclined crack through the compressive region; 3) “Shear-compression” failure, which was due to the crushing of the concrete in the compressive region above the inclined crack.

Moreover, this research compared the effect of various CFRP types and shear reinforcement configurations on the shear behaviour of the deep beam. It was evident that the use of anchorage by means of U-shape CFRP wrapping scheme can greatly increase the shear capacity of beams with CFRP shear reinforcement, and for the strip CFRP configurations, the load capacity of deep beams strengthened by 45° CFRP strips with respect to the beam axis had the largest increment. The test results obtained from each group revealed that the load resistance and ductility of the concrete deep beam were improved significantly. Finally, based on experiments and analytical studies, a design approach for evaluating the shear strengthening of concrete deep beams using CFRP laminates was proposed and it gave very good estimates for the shear strength of reinforced concrete deep beams as compared with the present experimental results.

It is noteworthy that the effective stress of the CFRP laminates at beam failure was less than that of the ultimate tensile stress in this study, thus a stress reduction factor was applied to reduce the ultimate tensile stress in the CFRP laminates when calculating the shear strength of the beam.

According to the available methods of analysis and design for reinforced concrete deep beams, addition of web reinforcement beyond the minimum amount provides only a small strength gain. In order to confirm the effectiveness and feasibility of strengthening structurally deficient deep beams by using an externally bonded fibre reinforced polymer (FRP) system on the beam web, six identical beams were constructed and tested to failure by Islam *et al.* (2002).

One of these beams was tested as the reference, while the remaining five beams were tested after being strengthened externally with different strengthening materials such as carbon fibre wrap, strip or grids. The experimental results indicated that all the specimens

demonstrated a nearly linear response up to about 80% of ultimate load and strengthening by external bonding of FRP system resulted in an increase in stiffness, but the increments were different due to the different layouts of these FRP systems. Based on the observation of cracking behaviour, externally bonded FRP systems postponed the appearance of the first crack and provided restraint to the widening of diagonal cracks. All of the beams failed in shear. The ultimate strength of beams strengthened with FRP systems increased significantly by 24% ~ 43% as compared with the control beam. Test results showed that a strengthening scheme by external bonding of FRP system was possible and practicable.

Furthermore, Islam *et al.* (2002) illustrated that externally bonded FRP reinforcement could be regarded as similar to the conventional internal reinforcement by taking into account the behaviour of the bond between the FRP material and the concrete surface. Usually, the full strength of the bonded FRP material could not be achieved due to the premature debonding failure. Thus, the effective strain value for the FRP material or using a limiting shear stress for the bonded concrete was suggested to be used in any suitable strength prediction method for the structure. Meanwhile, the existing calculation methods such as ACI Code (1998), CIRIA Guide 2 (1977), and Mau and Hsu's explicit method (1989) to predict the shear strength of concrete deep beams strengthened with FRP materials were discussed and the conclusion was that none of these methods could readily be used for predicting the improved load carrying capacities of strengthened deep beams.

Moreover, the application of FRP materials on regular concrete beams has been investigated quite extensively in the past, and the results of these investigations demonstrate the effectiveness of different types of FRP systems.

### **2.3 External Strengthening for Masonry Structures**

Strengthening masonry structures externally has elicited a worldwide interest in the last 20 years. Lots of researchers have extensively investigated the behaviour of various strengthened structures whether in laboratories or in fields, and these studies have made the retrofit and rehabilitation of old buildings possible. The materials used externally to

strengthen and rehabilitate the masonry members are usually high-strength steel plates, glass fibre reinforced polymer (GFRP) and carbon fibre reinforced polymer (CFRP).

Magnusson *et al.* (1984) provided a renovation technique for old masonry buildings, where large openings were required to be created in load bearing masonry walls. This method was devised by consulting engineers Jacobson and Widmark (1984). In this method, two steel plates were mounted on both sides of the opening and tightened by post-tensioned bolts to provide a friction joint between the plates and the wall above the opening, as shown in Figure 2-1. Four masonry beams with different spans were tested in the laboratory under four-point load. Also, four lintel beams of a 70-year-old building were examined in order to collect the field experiment data.

Test results showed that the stiffness and the ultimate load-carrying capacity of the lintels were lower than expected. The failure was caused by buckling of the strengthening plates in the centre of the span, and the beam with a large ratio of opening to beam height gave a considerably lower load carrying capacity. In all the experiments, the failure was ductile and the lintels had sufficient residual strength to carry themselves; visible crack formation in a service state was sufficiently low. The risk for this method was that the load-carrying mechanism, which counted on the friction between the plates and the masonry surface, could be lost easily because of either bad workmanship, the loss of tension due to bolt creep or the propagation of cracks. Moreover, this strengthening method could not be generalized due to the progressive corrosion of steel.

Compared with the method using steel plates to reinforce existing masonry structures, using FRP is more competitive since FRP possesses many advantages as mentioned before (including lightweight, high strength to weight ratio and electromagnetic neutrality). Many studies related to the strengthening of unreinforced masonry walls with different types of fibre reinforced polymer to improve the load capacity have been implemented and are described in the following.

Kuzik *et al.* (1999) studied the out-of-plane response of eight masonry walls externally reinforced with glass fibre reinforced polymer (GFRP) under fully reversed cyclic loading, as seen in Figure 2-2. The test results indicated that the overall flexural performance of the strengthened specimens was excellent and the strengthening system

increased the capacity of resisting the out-of-plane cyclic loading; the amount of GFRP significantly affected the stiffness and ultimate strength of the walls.

Foster *et al.* (2005) carried out a series of tests to investigate several repair and retrofit methods for existing unreinforced masonry structures, with rigid diaphragms, subjected to quasi-static lateral loading. GFRP wet lay-up, GFRP and CFRP near surface mounted rods and bars, and GFRP grid systems were adopted as the strengthening materials, as shown in

Figure 2-3. The experimental program showed that FRP composite laminates could restore and significantly enhance the seismic performance of unreinforced masonry structures in both damaged and undamaged configurations. Multiple FRP systems were utilized and all were well below ultimate strain values for each respective laminate at failure of the masonry building specimens.

Miao *et al.* (2005) investigated the behaviour of four masonry shear walls with the central opening strengthened by externally bonded CFRP, as seen in Figure 2-4, under monotonic in-plane load and constant vertical load. The effect of parameters such as the amount and layout of CFRP on the strength, stiffness and ductility were examined. The experimental results showed that the load capacity and ultimate displacement of walls strengthened with CFRP sheets, both increased significantly; the utilization of CFRP sheets postponed the appearance of the first crack. It was found that this method was convenient, effective and reliable.

In summary, the use of FRP as a material to retrofit and rehabilitate the existing masonry structures seems to be effective and feasible.

#### **2.4 Bond Between FRP and Cementitious Substrate**

The technique of utilizing FRP composites in upgrading and strengthening civil structures externally has been accepted gradually all over the world. It is required that the bond mechanism between FRP composites and substrates should be understood well since most investigations have shown that the structures strengthened externally with FRP composites failed by debonding between the FRP composites and the substrates before the strengthening material reached its ultimate strength. While there is no data on

the bond between FRP and concrete block masonry, some results regarding the bonding between FRP composites and cement-based substrates are listed here.

Lorenizs *et al.* (2001) performed a study related to the bond of FRP laminates to concrete substrates. Some of the factors expected to affect the bond, namely, bonded length, concrete strength, number of plies, ply width and surface preparation, were taken into account during the tests. Results showed that beyond the effective length, the CFRP sheet did not affect the ultimate load since the entire load was transferred to a certain point at which localized joint failure occurred and it caused the effective bond length to shift until the CFRP sheet was completely peeled from the concrete. Based on this investigation, it appears that the concrete strength did not affect the ultimate load because failure occurred at the concrete-epoxy interface. Also, the width of the sheet did not influence the bond strength, while the surface preparation of the concrete could significantly affect the average bond strength.

Chen and Teng (2001) provided a simple model to evaluate the ultimate bond strength for FRP and steel plates bonded to concrete. The ultimate bond strength of the joint was expressed as follows:

$$p_u = 0.427 \beta_p \beta_L \sqrt{f_c'} b_p L_e \quad (2.1)$$

Where

$$L_e = \sqrt{\frac{E_p t_p}{\sqrt{f_c'}}} \quad (2.2)$$

$$\beta_L = 1 \text{ if } L \geq L_e; \quad \beta_L = \sin \frac{\pi L}{2L_e} \text{ if } L < L_e \quad (2.3)$$

$$\beta_p = \sqrt{\frac{2 - b_p/b_c}{1 + b_p/b_c}} \quad (2.4)$$

$E_p$  = Young's modulus of the bonded plate;

$t_p$  = thickness of the bonded plate;

$L_e$  = the effective bond length;

$L$  = the actual bond length;

$b_p/b_c$  = the width ratio of the bonded plate to the concrete member.

From the formula above, it is clear that there was a critical bond length, beyond which, any increase in the bond length does not increase the anchorage strength. In addition, the ratio of the width of the bonded plate to that of the concrete member has a significant effect on the ultimate bond strength. In contrast to the conclusion obtained by Lorenizs *et al.* (2001), Chen and Teng (2001) pointed out that the bond strength depended strongly on the concrete strength.

Numerous studies related to the bond between FRP composites and concrete have been carried out recently, but very little work has been undertaken in the area of masonry structures.

Aiello and Sciolti (2005) conducted one such study regarding the analysis of the bond performance between FRP sheets and typical natural stones. Two commercially available CFRP sheets and two different types of masonry blocks (naples tuff and leccese stone) were used in the first stage of the analysis. In order to evaluate the distribution within the CFRP reinforcement at each load step up to debonding of FRP from the stone blocks, electrical resistance strain gauges were bonded to the sheet surface in the longitudinal and transverse directions. Bond tests were carried out varying the bond length of the reinforcement, the kind of FRP sheet, the type of stone, strengthening procedure, the specimen geometry and the type of bond test. On the basis of experimental and analytical results, this study showed that the transfer mechanism between the stone masonry and the fiber reinforcement was similar to that obtained for the case of a concrete substrate. However, the type of substrate had a great influence both at ultimate and at service conditions. In particular, the bond performance depended not only on the mechanical properties but also on other physical properties of the masonry blocks. Furthermore, the application of transverse FRP strips did not show any improvement, whether in terms of bond strength or strain values.

## **2.5 Summary**

A review of the literature indicates that the use of FRP composites as a type of strengthening strategy for existing structures is effective and practicable. Numerous studies have been carried out, which focus on the improvement of reinforced concrete

deep beams by using externally bonded FRP composites lately. However, no research regarding the external strengthening of reinforced masonry deep beams with FRP has been presented. Hence, such a research is required to have a better understanding about the response of masonry deep beams strengthened externally with reinforced material. The research here starts to investigate the effects of external CFRP plates as well as interior steel reinforcement on the behaviour of masonry deep beams under the monotonic 3-point loading.

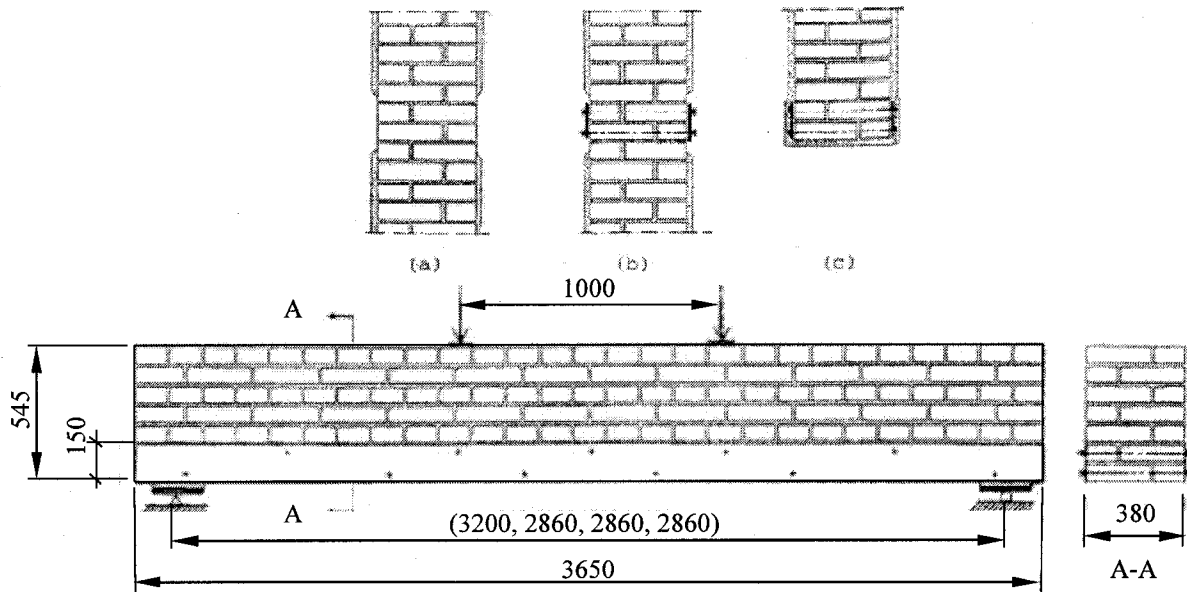


**Figure 2-1 Sketch of the Testing Arrangement in the Laboratory Experiments (After Magnusson, 1984)**

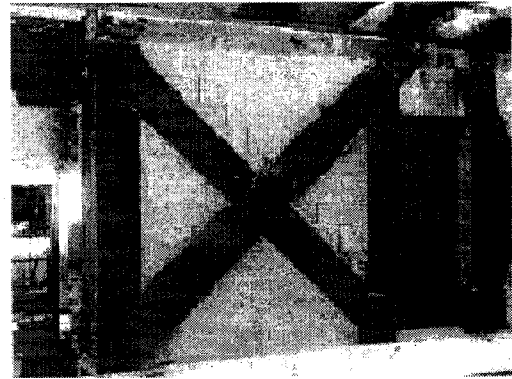
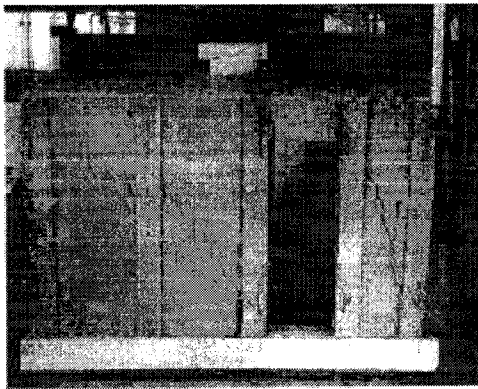
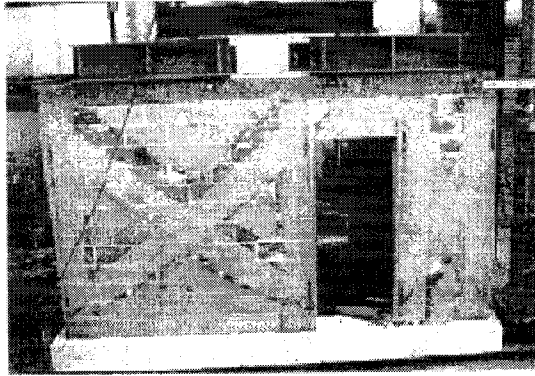
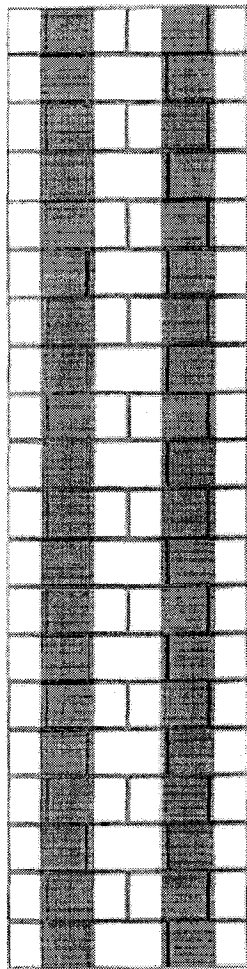
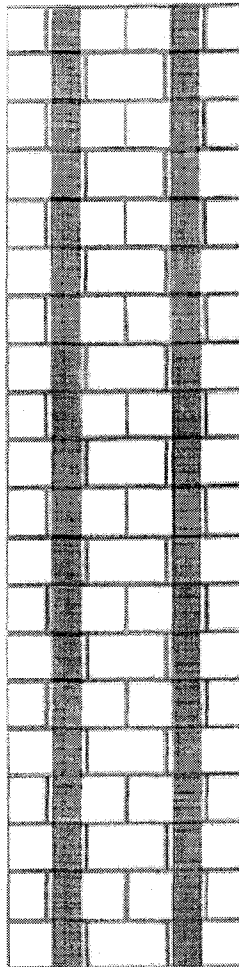


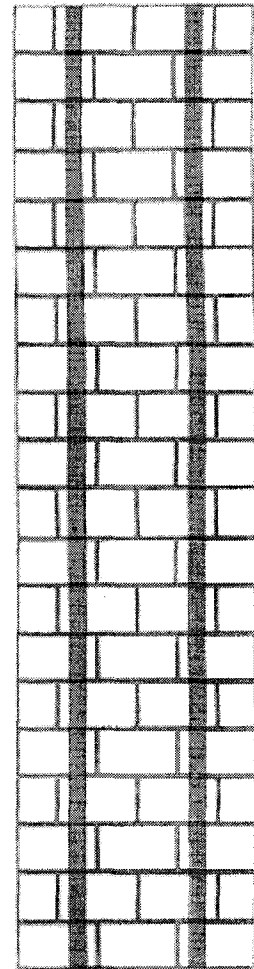
**Figure 2-2 Layout of GFRP and CFRP for the Specimens (After Foster, 2005)**



**2-250mm Wide Sheets**

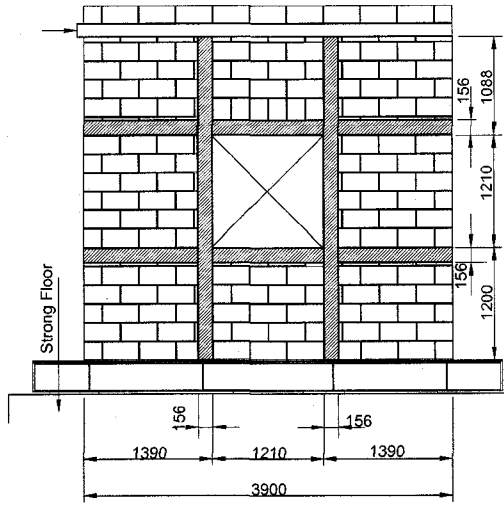


**2-130mm Wide Sheets**

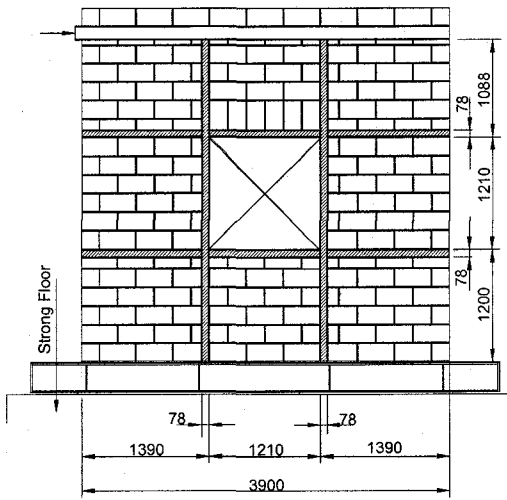


**2-65mm Wide Sheets**

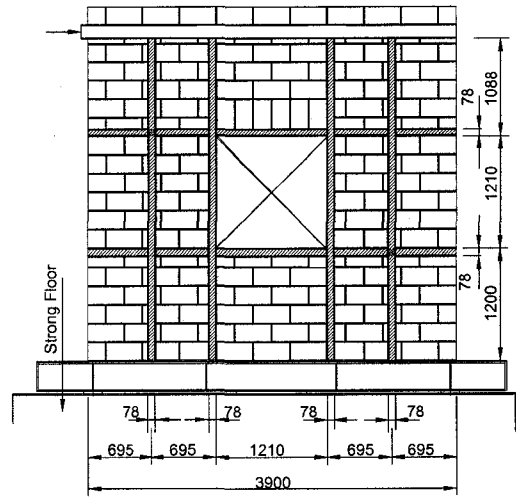
**Figure 2-3 GFRP Layout for the Specimens (After Kuzik, 1999)**



FRP LAYOUT FOR WALL 2



CFRP Layout for Wall 3



CFRP Layout for Wall 4

Figure 2-4 CFRP Layout for the Specimens (After Miao, 2005)

### **3. EXPERIMENTAL PROGRAM**

#### **3.1 Introduction**

Eight full-scale fully grouted masonry deep beams were constructed with identical dimensions but different reinforcing arrangements. These beam specimens consisted of a control beam without any reinforcement and 7 beams strengthened with steel reinforcement or with various amounts and layout of externally bonded CFRP plates and sheets. As shown in Figure 3-4 to Figure 3-9, each beam was 2590 mm long with a rectangular cross-section, 190 mm wide and 990 mm in depth. These specimens were tested under a 3-point quasi-static loading condition. The shear span to beam span ratio ( $a/L$ ) was 0.4. The material properties for the components of the test specimens, the test set-up as well as the details of each specimen are presented in this chapter. The amount and layout of reinforcing steel and CFRP plates were examined as the test parameters in this study.

#### **3.2 Material Properties for the Components of a Deep Masonry Beam**

Masonry systems are composed of masonry units, mortar, reinforcing steel and grout. This combination of materials creates an anisotropic system due to anisotropy of units, joint width, material properties of the mortar, arrangement of bed joints and head joints as well as the quality of workmanship. Therefore, a set of ancillary tests including individual masonry unit, mortar cubes, grout prisms, and masonry assemblages were implemented in order to achieve an accurate masonry description. Also, some tension coupon tests of steel rebar and CFRP plates were executed to obtain the property datum.

##### **3.2.1 Individual Masonry Unit**

Standard hollow concrete masonry blocks with dimension of 200 mm x 200 mm x 400 mm were used in this research. In total, six concrete masonry units were randomly sampled from different pallets and tested in accordance with CSA Standards A165.1-94 and ASTM C140-03 and C1552-03a to determine their compressive strength. As shown in Image 3-1, each sampling unit was capped with high strength gypsum plaster to enable flat and parallel faces. A material testing system with compressive capacity of 6200 kN (MTS-6000) was used to provide an increasing compressive load until the masonry unit

failed. The compressive strength of the individual unit was evaluated by dividing the maximum load by the average net cross-sectional area, (in this case  $36551\text{mm}^2$ ). The results of tests are summarized in Table 3-1. The mean compressive strength of concrete masonry units from the test data was 26 MPa and the standard deviation was 0.74 MPa.

### **3.2.2 Mortar**

Type S mortar was used to build specimens in this test program. There were two different batches of mortar involved to build the specimens since first the batch of mortar was not enough to construct all the specimens. Corresponding to this, two groups of standard 50 mm mortar cubes were sampled from two different batches at the same time as the beam specimens were built. Each group had 8 mortar cubes. A total of 16 mortar cubes were tested conforming to CSA Standard A179-94. A material testing system with compressive capacity of 1000 kN (MTS-1000) was used for the compression tests and the data were collected by a data acquisition system automatically. The compressive strength of mortar was obtained by dividing the failure load by the effective area ( $2500\text{mm}^2$ ). Table 3-2 presents the test results, and the mean compressive strength of mortar in Group 1 was 15 MPa with a standard deviation of 1.12 MPa, while the mean compressive strength in Group 2 was 18 MPa with a deviation of 0.98 MPa. In this experimental program, Beams 1, 2, 3, 6 and 7 were built using the first batch of mortar, while Beams 4, 5 and 8 were built using the second batch of mortar.

### **3.2.3 Grout**

A total of six grout prisms with dimension of 75 mm x 75 mm x 150 mm were built during the construction of the beam specimens. These grout prisms were divided into two groups since the first batch ran out before all the beam specimens were prepared. Therefore, four grout prisms were made from the first batch, while the other two were cast using the second batch of grout. The sampling and testing procedure of grout prisms was in accordance with ASTM C 1019-03. In order to obtain samples that were representative of the nature and condition of the grout, four masonry units, identical to those used in construction and a non-absorbent wood block were employed to form the mould, which simulated the absorption of moisture in the actual masonry. Image 3-2 shows the construction of grout specimens. After a curing period of 125 days, six grout

prisms were capped at top and bottom by using sulfur mixtures and tested in the MTS-1000. The failure load for each specimen was recorded and the mean compressive strength of grout was calculated. The compressive strengths for Group 1 and Group 2 were 34 MPa and 38 MPa, respectively. Table 3-3 presents the test results of the six specimens of grout.

### **3.2.4 Masonry Assemblages**

Masonry is a type of construction where a large number of small modular units are jointed together to form a structure. Therefore, it is not possible to determine the properties of the assembled masonry merely from the properties of the individual unit, mortar and grout. Thus, as per CSA Standard A369-1-M90 and ASTM C 1314-03b, five masonry prisms were built and tested to determine the strength of the masonry assemblage. These masonry prisms were fully grouted to simulate the beam specimens, which were all fully grouted. Each masonry prism was one and a half units wide (590 mm) and five courses high (990 mm). Units in prisms were oriented in the same way as in the beams. All mortar joints were furrowed for the sake of keeping consistency between prism specimens and beam specimens.

Since the first batch of grout and mortar ran out before building the masonry prisms, all the masonry prism specimens were constructed using the second batch of grout and mortar. Any uneven surface at the top due to shrinkage in the grout was flattened using fine sand, and two pieces of  $\frac{3}{4}$  inch thick fiber boards were placed beneath and at the top of each masonry prism before it was placed in the test machine (MTS-6000). These boards acted as the medium to transfer the uniform load from the loading machine head plate to the masonry prism. Two LVDTs were placed at both sides of each masonry prism to measure the uniaxial displacement. Test data were collected by a data acquisition system automatically.

The age of the masonry prisms at the time of testing was 85 days, which is longer than 28 days recommended by ASTM C1314. The typical failure mode of masonry prisms was as follows: the face-shells of masonry blocks in the top two courses spalled away from the grouted cores and vertical cracks were formed at webs and face-shells of the prisms.

The reason for this was the wedging action of the grouted cores. Image 3-3 and Image 3-4 show the test set-up and the typical failure mode of grouted masonry prisms, respectively.

The uniaxial compressive strength of fully grouted masonry prisms was evaluated by dividing the failure load by the effective area of the cross-section, which was measured before test. The elastic modulus of masonry prisms was obtained from the trend line of stress-strain curves with the smallest  $R^2$  value of 0.9927. The data analyzed are summarized in Table 3-4, in which the values of compressive strength and elastic modulus for each prism show significant scatter due to differences in workmanship. Especially, the imperfections in the construction of Specimen 3 were very obvious. The thickness of mortar joints was quite different and the alignment of the units was poor. The ineluctable eccentricity of each prism specimen under the loading machine was another reason for the variability in the test results. The mean value of uniaxial compressive strength of masonry prisms was 18 MPa with a standard deviation of 2.66 MPa and the average modulus of elasticity was 10150 MPa.

### **3.2.5 Carbon Fibre Reinforced Polymer (CFRP) plates**

Two kinds of CFRP plates were involved as externally bonded reinforcement in this experiment, Sika<sup>®</sup> CarboDur<sup>®</sup> S1012 and S512. The epoxy resin used was Sikadur<sup>®</sup> 30, which consisted of Part A and Part B. Plates S1012 and S512 had the same thickness (1.2 mm) but different width (100 mm and 50 mm) respectively. Three coupons for each kind of CFRP plates were sampled as part of this study, and tested till failure in tension using the MTS-1000 machine.

#### ***Sika<sup>®</sup> CarboDur<sup>®</sup> S1012***

The dimension of the coupons was 500 mm long by 80 mm wide. The coupons were cut from 100 mm wide to 80 mm since the width was limited by the head width of the loading machine. The tests were constructed complying with ASTM D 3039/D 3039M-00. In order to introduce the tensile force to the CFRP plate and prevent slippage between the grip face and the coupon, an emery cloth was used in the grip region to increase the friction. The length of the grip zone was 100 mm at each end. Three longitudinal strain

gauges with 5 mm gauge length were stuck onto the middle of the CFRP coupon to obtain the elongation of the specimen, two on the front face across the width and one on the back face of the specimen, as shown in Figure 3-1. This arrangement could also evaluate the system alignment.

The stress-strain behaviour of plate coupons is presented in Figure 3-2, where the strains were taken as the average value of the data obtained from three strain gauges. It can be seen from the curve that CFRP is linearly elastic up to failure. Moreover, the data from three strain gauges showed that the system alignment worked well. The failure initiated with several small strips of broken fibres, followed by catastrophic rupture of the middle part of the specimen. Image 3-5 shows the typical failure mode of CFRP plate coupons. The modulus of elasticity was estimated via a trend-line in the stress-strain curve with the lowest  $R^2$  of 0.9986. Table 3-5 presents the test results of three coupons.

#### ***Sika® CarboDur® S512***

Three coupons with an identical dimension, 500 mm long by 50 mm wide, were selected. The grip method and strain gauge arrangement were same as those in coupons of S1012, and shown in Figure 3-1. Failure mode was completely identical with S1012. The stress-strain behaviour is shown in Figure 3-3. In which, strains were taken as the average of the values of three strain gauges. The modulus of elasticity was estimated via a trend-line in the stress-strain curve with the lowest  $R^2$  of 0.9988. The test results are presented in Table 3-5.

### **3.2.6 Carbon Fibre Reinforced Polymer Sheets**

The CFRP sheet used in this test research was Wabo® MBrace CF130, which is a unidirectional high strength carbon fibre sheet. The epoxy resin includes three components such as viscosity epoxy primer, high viscosity epoxy putty and epoxy encapsulation saturant. Each component consists of two parts: Part A and Part B. Six tension coupons of the fibre sheet were constructed and tested as per ASTM D3039/D 3039M-00 by Miao *et al.* (2005) and the CFRP sheets used in this study were taken from the same roll as was used by Miao and her associates. The detail test procedure and stress-strain curves were presented in Section 3.2.6 of Miao *et al.* (2005) study. Each

coupon was 325 mm long by 25 mm wide and consisted of six layers in the gauge segment and eight layers in the end grip regions. Three strain gauges with gauge length of 5 mm were mounted on each coupon in the longitudinal, transverse and 45° directions to collect the strain data during the test. The stress-strain relationship of the CFRP sheets in tension shows a characteristically linear elastic response in a wide range of stress level. The failure models for all six coupons were identical and all catastrophically ruptured in the gauge region. The mean modulus of elasticity was 68580 MPa with a standard deviation of 3079 MPa.

### **3.2.7 Steel Reinforcement**

Three types of standard deformed reinforcing bars marked as M15W400, B15 and 10W400 respectively, were used to build the beam specimens. The specified yield strength ( $f_y$ ) was 400 MPa. As bottom longitudinal reinforcement, rebar of type B15 was used in Beam 2 and Beam 3, while rebar of type M15W400 was used in Beam 6 and Beam 7. In addition, rebar marked as 10W400 was used as web stirrups in Beam 3 and Beam 7. The reinforcing steel was randomly sampled and prepared according to ASTM A370. Three rods for each kind of rebar were extracted and tested to failure. The MTS-1000 loading machine was selected to perform the tension tests. Each rebar specimen was 355 mm long with a grip length of 90 mm at each end. A 50 mm gauge length extensometer, which was calibrated before using, was mounted onto the middle of the coupon to measure the axial elongation. The test results and the material properties are summarized in Table 3-6. The cross sectional areas taken to calculate the stress for No.10 and No.15 steel rebar were 100 mm<sup>2</sup> and 200 mm<sup>2</sup>, respectively.

## **3.3 Test Specimens**

### **3.3.1 Description**

Eight specimens were designed to achieve the objectives of this research. One was treated as a control beam without any reinforcement. Two of them were reinforced traditionally with steel reinforcement, to investigate the load-displacement response of masonry deep beams, and also, these two beams were considered as benchmarks for the specimens strengthened with FRP laminates. The remaining five beams were designed to explore the

behaviour of masonry deep beams strengthened externally with CFRP laminates. The amount and layout of CFRP plates were investigated as test parameters in these five beams.

Eight full-scale masonry deep beams were constructed by two professional masons. The materials used were 200 mm standard concrete masonry blocks with strength of 15 MPa and type S mortar (as per ASTM). The beam specimen had identical dimensions: 990 mm (5 courses) deep, 2590 mm (6 and a half blocks) long and 190 mm thick with every core fully grouted. According to CSA S304.1-94, No.9 gauge ladder type joint reinforcement was placed at every second course. Running bond was used and mortar joints were furrowed in order to keep consistency between laboratory test and field condition. All specimens were moistly cured and covered with plastic fabric after construction. The plastic fabric was removed after 7 days and the specimens were left to cure under ambient conditions in the laboratory for more than 28 days before testing.

The beam span was 1800 mm and each end had a length about 400 mm to develop the anchorage force for the strengthening material. According to the Clause 12.3.6 of CSA S304.1-94, the specimens here behaved as deep masonry beams with a shear span to beam span ratio ( $a/L$ ) of 0.4. Each specimen was strengthened with a different reinforcing strategy as described in the following section. In order to prevent any local buckling at the regions of loading and support reaction, three stiff steel plates were employed to disperse the forces to the beam, as shown in Figure 3-13.

### **3.3.2 Specimen Details**

Beam 1 was fully grouted but without any reinforcement and was considered as the control beam for this study. Due to a lapse on the part of the masons, there was no joint reinforcement in Beam 1 either.

Beam 2 was reinforced with two No.15 deformed steel rebars at the bottom of the beam. In order to put the longitudinal steel rebars in, the webs of the bottom layer of concrete masonry blocks were cut at mid height to form a continuous trough. For the sake of the anchorage, two standard hooks were formed at both ends of the steel rebar to assure enough development length. Similarly, there was no joint reinforcement inside this beam.

The strength of the steel was taken as  $f_y = 412$  MPa. Two strain gauges were mounted on each rebar under the load point, as shown in Figure 3-4.

Beam 3 was not only reinforced with two No.15 longitudinal steel rebars at the beam bottom, but also reinforced vertically with eleven No.10 steel rebars within the cores as the web reinforcement. All bars had standard hooks at the both ends, and the strengths of the steel were taken as  $f_y = 412$  MPa for No.15 bars and  $f_y = 421$  MPa for No.10 bars, respectively. The layout of steel rebars and strain gauges are shown in Figure 3-5.

Beam 4 was strengthened with only two pieces of Sika® CarboDur® S1012 CFRP plates that were externally bonded longitudinally on both surfaces at the bottom of the beam. Figure 3-6 shows the detail of the layout of CFRP plates and strain gauges.

In order to establish the effect of the amount of FRP reinforcement, Beam 5 was strengthened by half the amount of CFRP used in Beam 4, that is two pieces of Sika® CarboDur® S512 CFRP plates at the bottom of the beam. The application of CFRP plates was identical to Beam 4, as illustrated in Figure 3-7.

In order to study the effect of the sequence of using an anchorage system on the behaviour of the specimen as well as on the bond between the laminate and substrate, Beam 6 was strengthened with the same strengthening strategy as that used in Beam 5, but the instant of introducing the anchorage system was different. Detailed description is presented in Chapter 4, Section 4.4.6 of this thesis.

Similar to Beam 4, Beam 7 was strengthened with a piece of Sika® CarboDur® S1012 CFRP plate that was bonded externally and bonded longitudinally on each surface at the bottom. In addition, a piece of No.10 web rebar with standard hooks at both ends was placed into each vertical masonry core of this beam, as shown in Figure 3-8. This beam was used to study the behaviour of deep beams strengthened with CFRP plates at the bottom of the beam, meanwhile, steel reinforcement within the beam web.

Beam 8 was strengthened externally with two pieces of Sika® CarboDur® S1012 CFRP plates longitudinally at the bottom of the beam and twenty-two pieces of Wabo® MBrace CF130 CFRP sheets vertically as web reinforcement on both surfaces of the specimen.

The position of CFRP sheets was identical with the web steel rebars used in Beam 3 and Beam 7, as shown in Figure 3-9. It is important to note that CFRP sheets were overlapped by the CFRP plates at the intersecting regions.

### **3.4 Application of CFRP**

#### **3.4.1 CFRP Plates**

SiKadur® 30, which is a high modulus and high strength structural epoxy paste, was used as the adhesive to bond the CFRP plates onto the surface of the masonry beams. Prior to applying the epoxy, the masonry surface was cleaned as follows: First, the uneven mortar joints and projections were ground using a power grinder and the foreign particles were removed by using a flat coarse masonry block to rub the specimen surface. Then, the fine dust was blown away using compressed air. The CFRP plates were cut to the required length ( $L = 2610$  mm) and the surface was wiped using acetone until all residual carbon dust was removed.

Sikadur® 30 consists of two components: Part A and Part B. Each component was stirred thoroughly according to Manufacturer's recommendation prior to bringing together. The mix ratio used here was A:B = 3:1 by weight. Since the epoxy paste was applied vertically, fine sand, whose weight is 25% of the total weight of the epoxy, was added into the well-mixed compound of Parts A and B so to decrease the fluidity.

The Sikadur® 30 so prepared was applied onto the masonry substrate and the CFRP plates to a rough thickness of 1.5 mm with a trowel. Within the epoxy open time, in which the epoxy remains fluid, the CFRP plates were placed onto the masonry surface and a hard rubber roller was used to press the laminates into the epoxy resin to keep the glue line within 3 mm. The specimen was left for curing for at least 7 days without disturbance.

#### **3.4.2 CFRP Sheets**

When used with Wabo® MBrace CF130 CFRP sheets, the epoxy resin included three parts, namely, the Wabo® Mbrace primer, the putty and the saturant. Prior to preparing the masonry surface, the CFRP sheets were cut into strips, which were 1000 mm long and

50 mm wide. The procedures for preparing the surface were identical to those for CFRP plates. Masking paper was used to prevent the excess resin when applying the epoxy onto the wall.

The first component of Wabo<sup>®</sup> Mbrace system was the primer and it consists of two parts: Part A and Part B. The mix ratio was 3: 1 (Part A to Part B) by volume in this study. Before the two parts were blended together, each was agitated by means of an electric hand mixer for 2 minutes. The well-mixed primer was applied using a short nap roller and ensured that it penetrated the pores of the masonry surface so as to provide a base with strong bond for the strengthening system.

After 24 hours of curing, the second component, the putty, was applied onto the primed substrate to fill the concave mortar joints by a spring-steel trowel to make the masonry surface smooth and to level small surface defects. Similar to the procedure of mixing the primer, two parts of this component were premixed and then blended together by the mix ratio of 3:1 (Part A to Part B) until a homogeneous mixture was achieved. Another interval of 24 hours was required to ensure that the putty was dry and hardened.

The third part of this epoxy was a saturant, which in twin comprised of two parts, Part A and Part B. The mixing procedure and mix ratio of the saturant were identical with the primer and the putty. The base coat of the saturant was dipped onto the substrate using a medium nap roller, then, the rolled CFRP sheets were extended along the base coat of saturant and pressed into the first coat using a hard rubber roller. To ensure that all CFRP sheets were soaked into the saturant, the second coat of the saturant was applied onto the top of the sheets. Once again, a hard rubber roller was used to smooth the surface of the composite strengthening system. The specimen was left for to cure for eight days before installing of instrumentation.

### **3.5 Test Set-Up**

As shown in Figure 3-10 and Figure 3-11, the test set-up for full-scale deep masonry beams included five portions, i.e. the loading system, the reaction system, an out-of-plane bracing system, the anchorage system and the temporary safety system.

### ***Loading System***

The loading system comprised of two steel columns, an assembled stiff steel beam and a double action compression hydraulic ram with a capacity of 200 kips (890 kN). Two steel columns were fixed onto the strong floor by eight high strength bolts and a built-up HSS beam was bolted to them to provide the reaction force for the hydraulic ram as shown in Image 3-6. The load was applied by connecting the hydraulic ram to two manually operated hydraulic pumps, one for loading and the other for unloading. A flat load cell was attached to the hydraulic ram head at the bottom to measure the compression load. Beneath the load cell, a half steel sphere and a set of knife-edges were used to assure the load vertical. For the sake of preventing local crushing on the top-loading zone due to the load concentration, a stiff bearing plate (400 mm long, 200 mm wide and 70 mm thick) was placed to spread the concentrated load to the specimen. A layer of 5 mm thick gypsum plaster was applied onto the loading region to avoid the stress concentration from surface irregularities. Image 3-7 presents the detail of the top loading system.

### ***Reaction System***

The reaction system sat at the top of a strong steel beam, 380 mm wide and 460 mm high, which was strengthened with six web stiffeners at each side of the web at equal spacing. Each assembled support consisted of a knife-edge, a roller and a flat load cell with a capacity of 100 kips (450 kN), as seen in Image 3-8. Four threaded rods were used to hold all the parts together and to make the alignment easier. The base plate of the anchorage system was mounted on the top of the knife-edge. Moreover, a stiff steel plate (400 mm in length, 200 mm in width and 38 mm in thickness) was used as a bearing plate to ensure against local crushing on the specimen during the test. As before, a layer of gypsum plaster was applied to keep a uniform contact between the bottom of masonry specimen and the bearing plate.

### ***Out-of-Plane Bracing System***

Out-of-plane bracing system was designed to prevent any lateral movement of the specimen caused by an eccentricity of the vertical load. Two horizontal lateral bracing frames were set up perpendicularly to the specimen plane under the location of the top

load to prevent the out-of-plane movement. A steel cylinder roller was installed at the end of the lateral bracing frame to contact with the surface of the specimen and to allow the specimen moving downwards without restraint. The other end of the lateral bracing frame was fixed onto the column to provide the reaction force. Image 3-9 shows the details.

### ***Anchorage System***

Premature failure often happens due to debonding between CFRP laminates and the surface of the rehabilitated structure. Therefore, in this study, an anchorage system was introduced to avoid premature debonding at the support regions, as shown in Figure 3-12. A base steel plate with two vertical steel plates formed a “U-Shape” scheme. Five holes were threaded on each vertical plate to place the bolts, which were then used to squeeze a half-inch thick steel plate that could push the CFRP plate against the masonry wall. This was intended to avoid or other delay the debonding. Again, a layer of plaster was applied between the steel and CFRP plates to obtain a uniform contact surface. Image 3-10 shows the actual anchorage system used during the test.

### ***Temporary Safety System***

Since masonry structures without steel reinforcement possess little ductility under heavy loading, most of the failure modes were expected to be brittle and catastrophic. In order to avoid any harm to operators and any damage to the instrumentation, some temporary protection arrangements were employed. Two stubbed steel columns were fixed at both ends of the specimen at the top of the strong base beam, and a 30 mm space between the stubbed column and each end of the specimen was left to allow the ends of the specimen to move outwards without confinement during the test. In addition, a piece of plywood was placed underneath the specimen and a 60 mm gap between the plywood and the bottom of the specimen was left to allow for flexural deformation of the specimen. These details are shown in Figure 3-10.

## **3.6 Instrumentation**

The following instrumentation was used during testing to monitor the behaviour of the specimen and the loading status. Linear Variable Displacement Transducers (LVDTs)

were used to measure the deflection of the specimen and the change in distance between two supports. Load cells were used to monitor the applied load and reaction loads. The state of strain in steel rebars and CFRP laminates was obtained by sticking strain gauges onto them. All the data were collected through an electronic data acquisition system. Moreover, some Demec gauges were mounted on the surface of the specimen to measure the strain distribution by hand.

### ***Load Cells***

A load cell with a capacity of 200 kips (890 kN) was attached to the bottom of the hydraulic ram to measure the applied load, and two load cells, each with a capacity of 100 kips (450 kN), were put under the knife-edges at two supports to monitor the reaction forces. Based on the equilibrium of applied and reaction loads, the validity of load cells was checked. Figure 3-13 presents the location of load cells.

### ***Linear Variable Displacement Transducers (LVDTs)***

In total, eight LVDTs were used to measure the displacement of the specimen and equipment, as shown in Figure 3-13. Three of them were placed vertically beneath the specimen at mid-span and 1/4 span to obtain the deflections of the specimen, and two LVDTs were arranged between the top load point and bottom supports along the diagonal lines to evaluate the deformation of the diagonal struts that was expected to develop. One LVDT was installed horizontally between two base plates of the knife-edges to monitor the relative displacement of the two supports, and two LVDTs were attached on the support load cells horizontally to measure the movement of each support.

### ***Strain Gauges***

Strain gauges with gauge length of 5mm and resistance of  $120\Omega$  were employed during the test. Some were mounted on the tension and the web rebars to obtain the strain response in steel reinforcement, and the others were placed on the surface of CFRP plates at different locations to monitor the strain profiles along the plates. The layout of the strain gauges was different with the different specimens.

### *Demec Gauges*

Strain gauges are not ideal for measuring the strain on the surface of masonry specimen since masonry is a kind of brittle material and it is hard to predict the propagation of masonry cracks. Moreover, the coarse surface of masonry structures is not suitable for mounting strain gauges. Thus, a series of Demec gauges was used to monitor the strain distribution of the masonry specimens. Two types of Demec gauges were used: 50mm Demec gauge and 200 mm Demec gauge. The 50 mm Demec gauge points were arranged in a shape of a rosette along the diagonal struts to obtain the principal strain. The 200 mm Demec gauge points were installed onto the face shells of the bottom layer of the specimen at mid-span, and some of them were mounted onto the surface of CFRP plates and fabric strips. As one division represents a strain of  $2.5 \times 10^{-5}$  and  $0.81 \times 10^{-5}$  for 50 mm gauge length and 200 mm gauge length, respectively, it was possible to evaluate the strain during a test. Figure 3-14 shows the arrangement of Demec points in detail, where the Demec gauge locations were marked from 1 to 9.

### **3.7 Test Procedure**

Before the specimen was placed into the loading frame, it was placed on top of two strong steel chairs so that all instrumentation including the Demec gauge points and strain gauges could be applied easily. Also, the loading point, support points and centre-line were marked in advance to make the alignment easier. The assembled supports were levelled by adjusting four corner-threaded rods; moreover, the rollers were locked temporarily. Then, the specimen was lifted into the testing position by an overhead crane, and was placed on top of two temporary supports. Following this, the out-of-plane bracing system was placed against the specimen to keep it plumb and prevent it from lateral movement due to any eccentric loading. Using a hand-hold hydraulic jack, a layer of plaster was applied between the bearing plates and the bottom of the specimen. Another layer of plaster was placed between the top bearing plate and the top of the specimen. Once again the plaster helped reduce concentrated stress. Finally, the top knife-edge and the half steel sphere were assembled to form the loading system.

Once the specimen was installed, all LVDTs were placed at their locations and all load cells, strain gauges and LVDTs were led out to connect to a Fluke data acquisition system.

At the same time, the end stoppers and bottom plywood were set in place to ensure safety. The details are shown in Image 3-11. Before starting the test, the initial Demec gauge values were taken and all LVDTs were calibrated. Furthermore, the rollers and corner rods, which were used to hold the support assembly, were released to activate the rollers and supports.

Before starting the test, the load capacity for each beam was predicted by using a Strut-and-Tie model in order to have a better control for applying the load. Vertical load was slowly provided by using a manual hydraulic pump and the data was read at a five-second interval at the beginning, which was switched to three seconds when the load reached 50% of the predicted capacity. The Demec gauge readings were recorded at regular interval of 50 kN. Also, during the loading, a visual inspection was executed and the cracks were marked with corresponding load level on the specimens. All specimens were tested until they catastrophically failed. The loading procedure and the test results for each beam are presented in detail in Chapter 4.

**Table 3-1 Compressive Strength of Individual Masonry Unit**

Specimen Number	Net Cross-Section Area (mm <sup>2</sup> )	Maximum Load (KN)	Strength (MPa)
1	36551	957.9	26.2
2		990.1	27.1
3		932.7	25.5
4		957.6	26.2
5		952.9	26.1
6		1006.4	27.5
		<b>Mean Value</b>	<b>26.4</b>
		Standard Deviation	0.74
		C.O.V	0.03

**Table 3-2 Compressive Strength of Mortar Cubes**

Specimen Number	Group 1		Group 2	
	Max.Load (KN)	Strength (Mpa)	Max.Load (KN)	Strength (Mpa)
1	36.8	14.7	42.2	16.9
2	33.1	13.2	48.3	19.3
3	38.1	15.2	42.11	16.8
4	35.9	14.4	48.3	19.3
5	34.3	13.7	44.1	17.6
6	40.7	16.3	44.9	18.0
7	36.7	14.7	46.9	18.8
8	41.0	16.4	44.9	18.0
Mean		14.8		18.1
Std.dev		1.12		0.98
C.O.V.		0.08		0.05

**Table 3-3 Compressive Strength of Grout Prism**

Specimen Number	Group 1			Group 2		
	Max.Load (KN)	Cross Sectional Area (mm <sup>2</sup> )	Strength (MPa)	Max.Load (KN)	Cross Sectional Area (mm <sup>2</sup> )	Strength (MPa)
1	207.0	5776	35.8	224.3	5719	39.2
2	192.3	5700	33.7	218.1	5891	37.0
3	173.0	5663	30.5			
4	191.7	5681	33.7			
Mean			33.5			38.1
Std.dev			2.18			1.55
C.O.V.			0.07			0.04

**Table 3-4 Results of the Grouted Masonry Prism Test**

Specimen Number	Net Cross Sectional (mm <sup>2</sup> )	Max. Load (KN)	Strength (MPa)	E <sub>m</sub> (MPa)
1	112227	2215.0	19.7	Invalid
2	112100	2129	19.0	8235
3	112290	1503.3	13.4	5624
4	112005	1886.4	16.8	10943
5	112227	2185.5	19.5	15796
		<b>Mean</b>	<b>17.7</b>	<b>10150</b>
		Std.dev	2.66	4346
		C.O.V	0.15	0.43

**Table 3-5 Test Results For CFRP Plates**

Specimen Type	Specimen Number	Max. Load (KN)	Strength (MPa)	$E_m$ (MPa)
<b>SiKa S1012</b>	1	302.2	3152	1956000
	2	284.9	2968	1836000
	3	269.5	2808	1873000
		<b>Mean</b>	<b>3060</b>	<b>1896000</b>
		Std.dev	129.9	84853
		C.O.V	0.01	0.04
	<b>SiKa S512</b>	1	191.6	3193
2		192.5	3208	1928000
3		189.4	3156	1801000
		<b>Mean</b>	<b>3185.8</b>	<b>1870667</b>
		Std.dev	26.81	64392
		C.O.V	0.01	0.03

**Table 3-6 Material Properties of Steel Reinforcement Coupons**

Specimen Type	Specimen Number	Yield Stress (MPa)	Ultimate Stress (MPa)	Modulus of Elasticity (MPa)
10W	1	427	609	212500
	2	410	631	216400
	3	425	608	222300
	<b>Mean</b>	<b>421</b>	<b>616</b>	<b>217067</b>
M15W400	1	413	535	195700
	2	405	531	180900
	3	Invalide	Invalide	Invalide
	<b>Mean</b>	<b>409</b>	<b>533</b>	<b>188300</b>
B15	1	410	666	192900
	2	408	661	191000
	3	417	675	198600
	<b>Mean</b>	<b>412</b>	<b>667</b>	<b>194167</b>

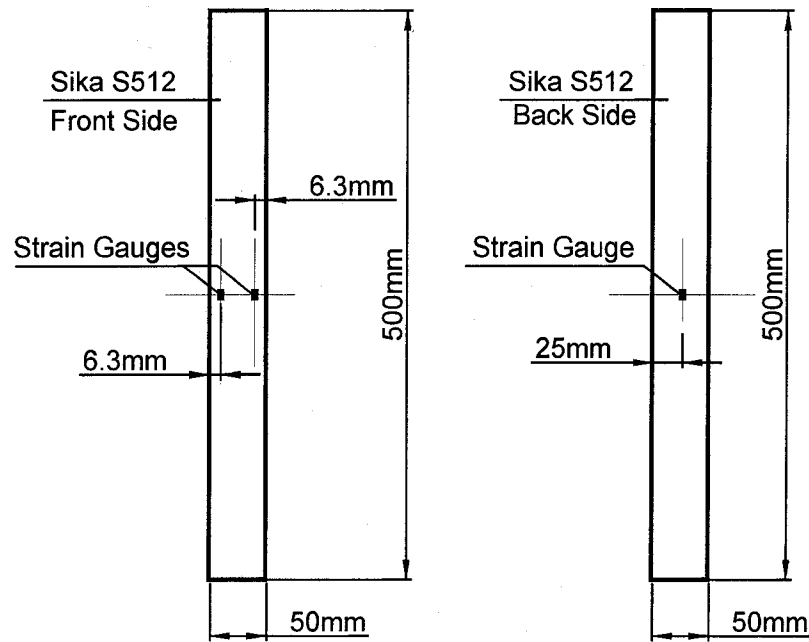
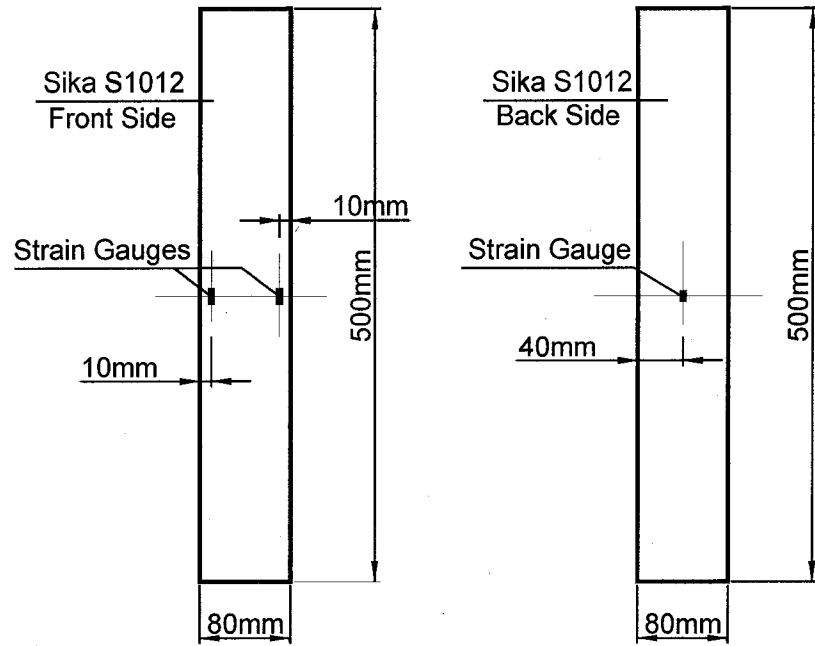


**Figure 3-1 Layout of Strain Gauges on CFRP Plate Coupons**

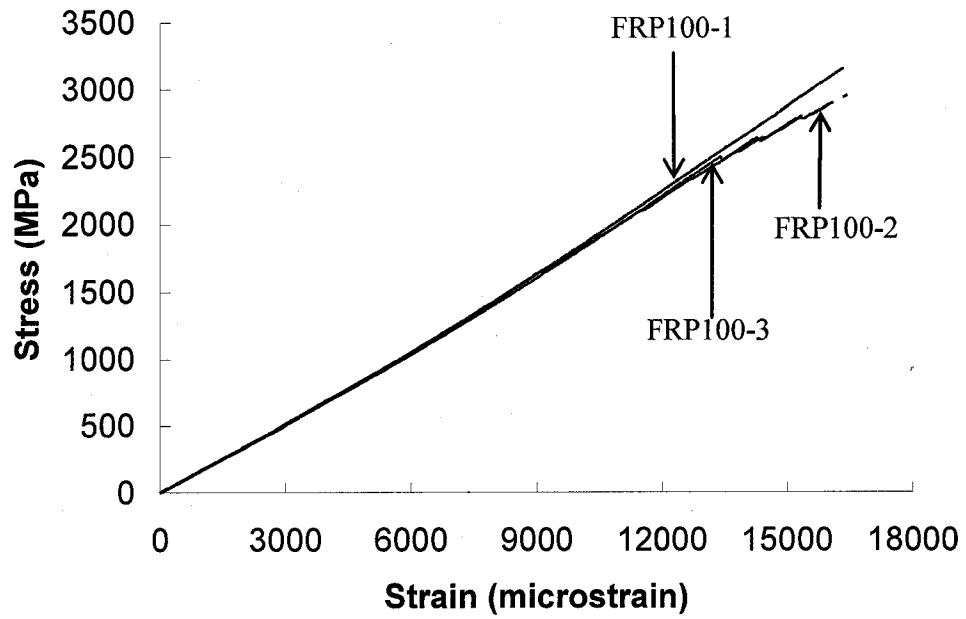


**Figure 3-2 Test Behaviour of Sika S1012 Coupons**

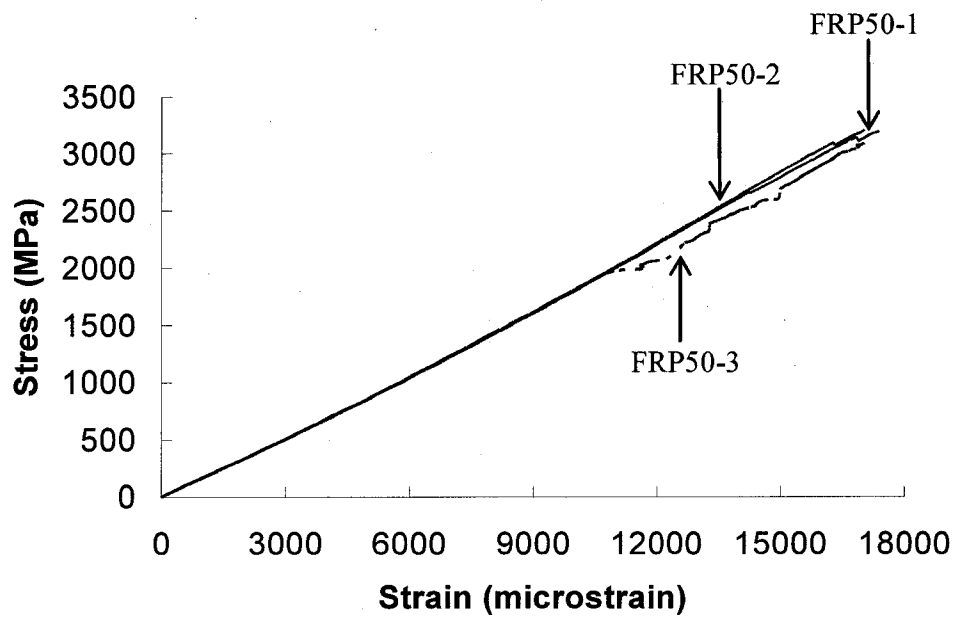


**Figure 3-3 Test Behaviour of Sika S512 Coupons**

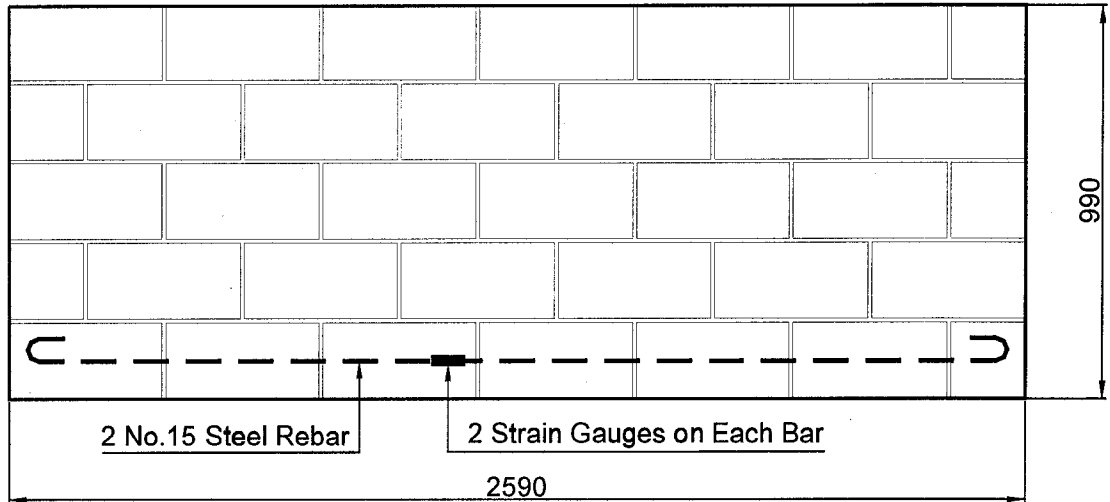


**Figure 3-4 Detail of Beam 2**

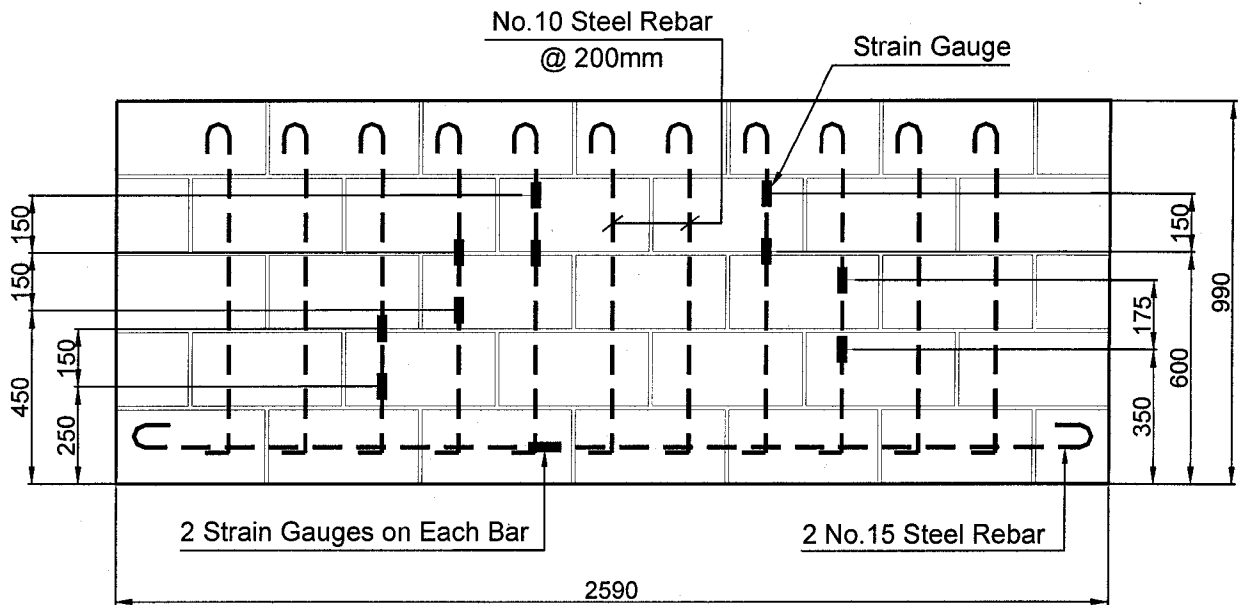
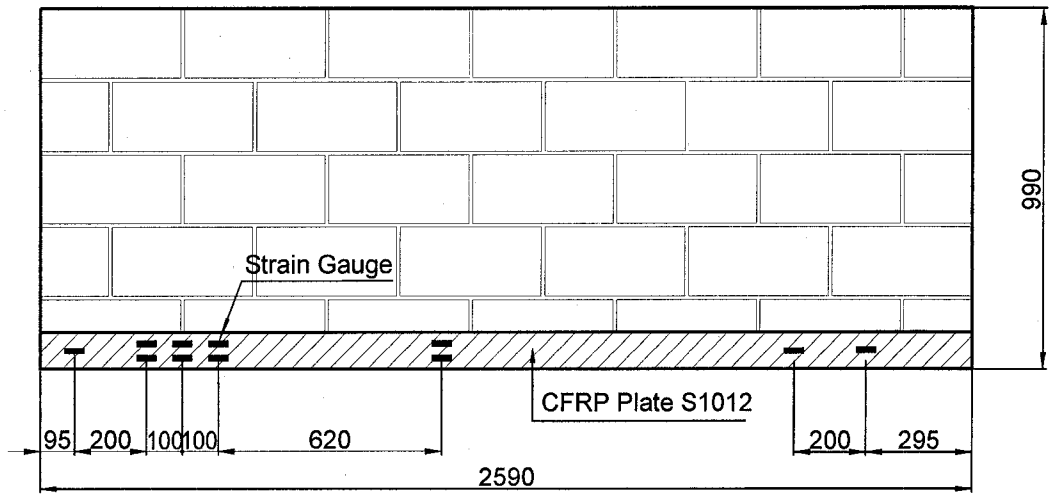
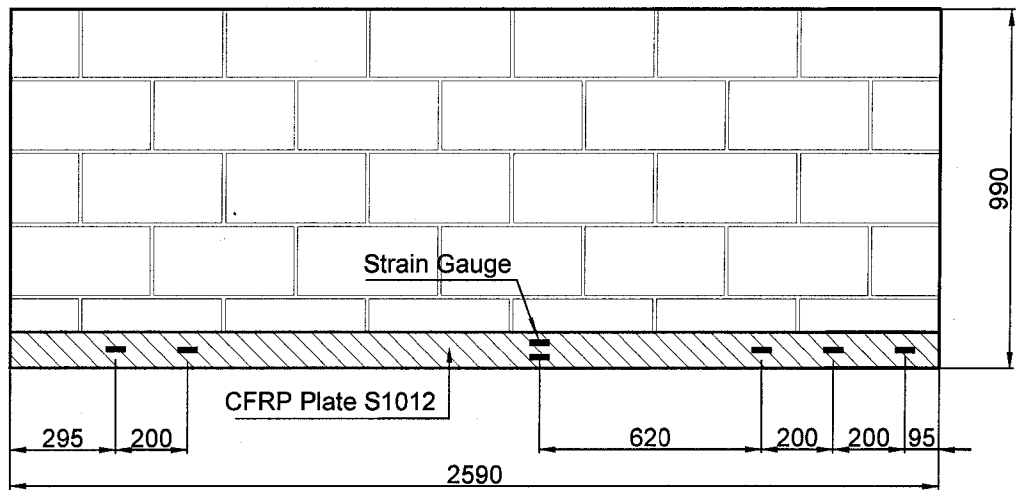


**Figure 3-5 Detail of Beam 3**



Front Face



Back Face

Figure 3-6 Detail of Beam 4

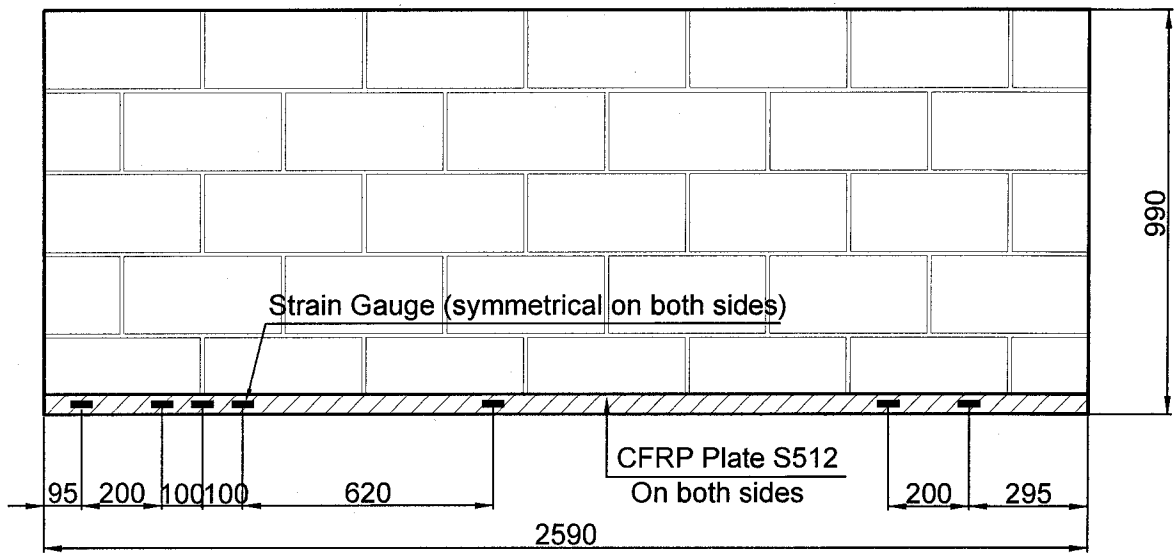
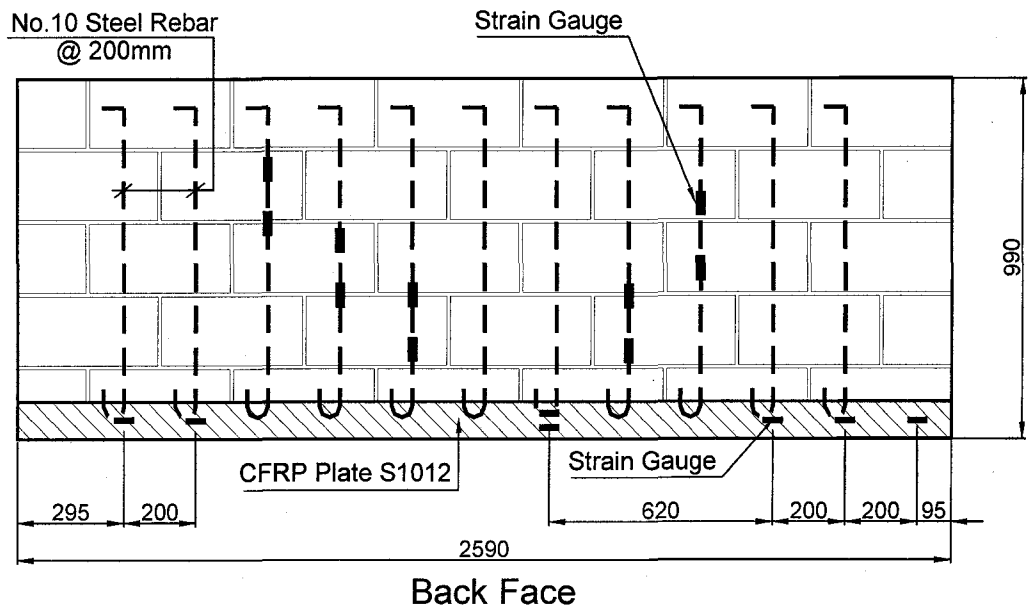
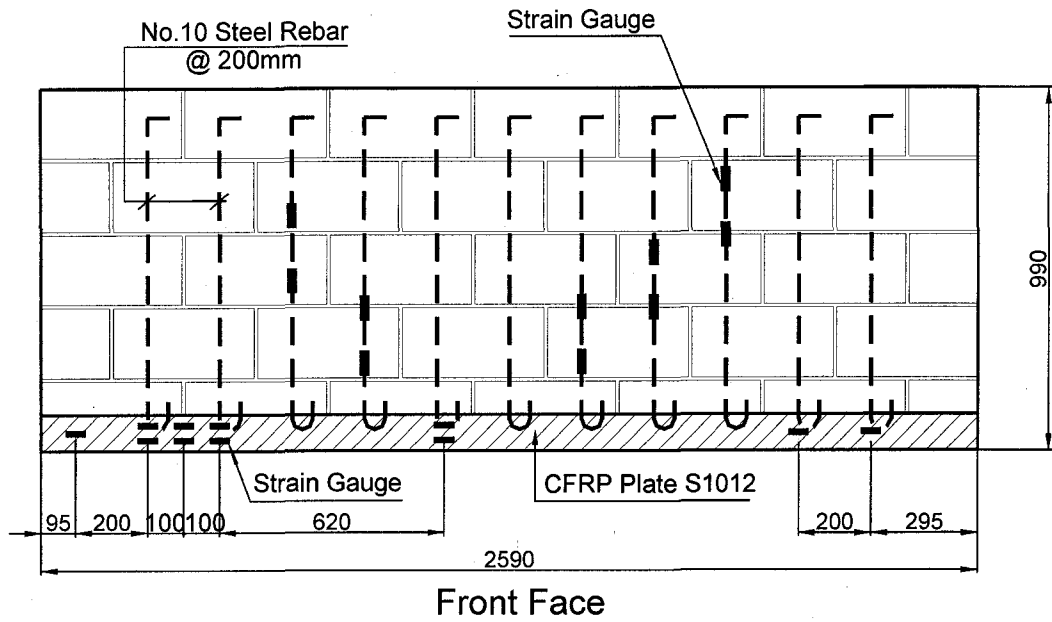
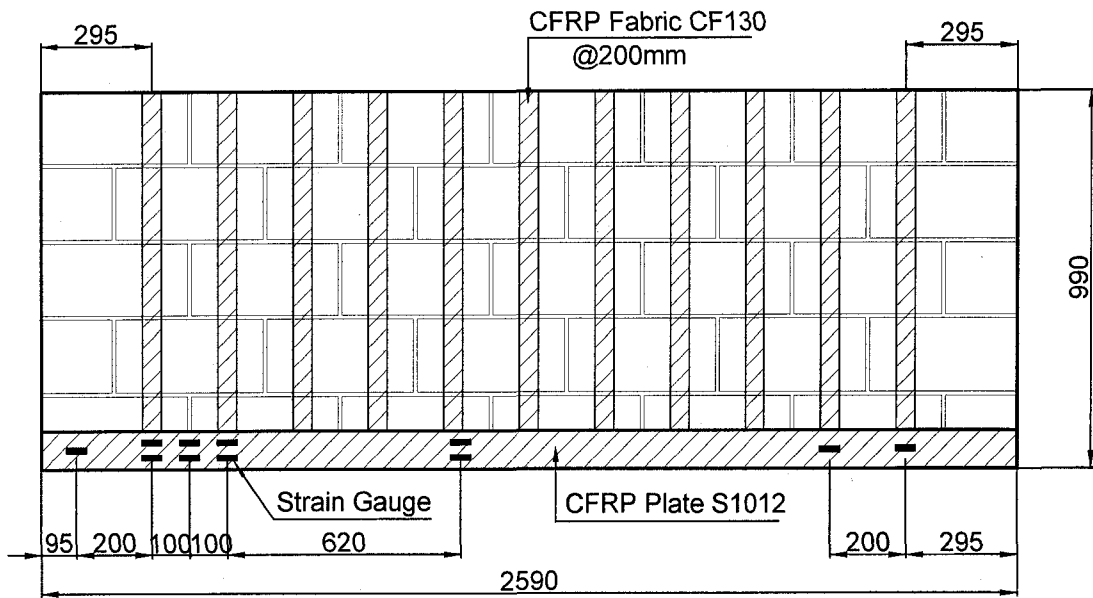


**Figure 3-7 Detail of Beams 5 and 6**

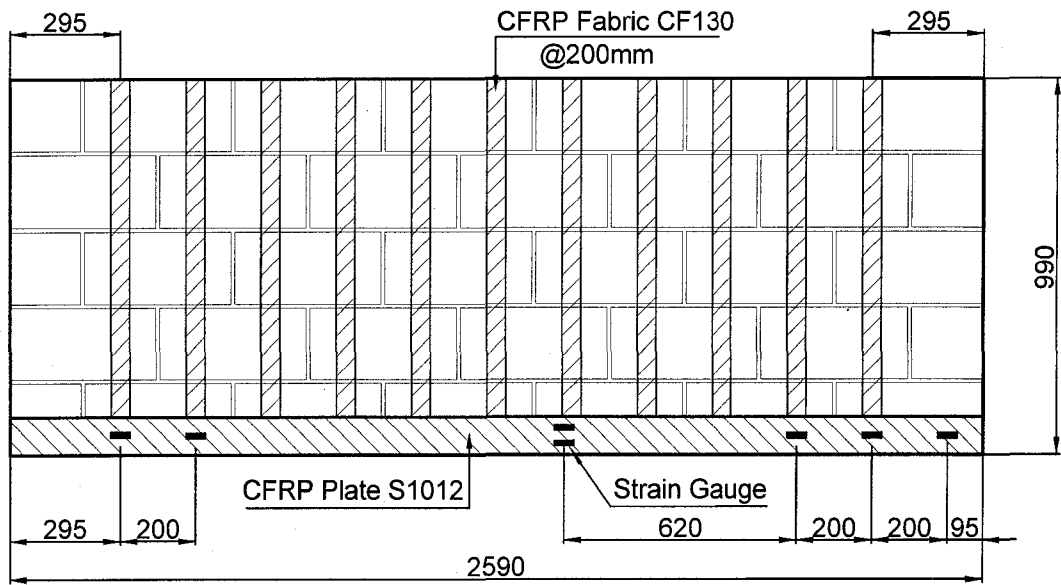


(The layout of strain gauges on the steel reinforcement was same as that in specimen 3)

**Figure 3-8 Detail of Beam 7**



Front Face



Back Face

Figure 3-9 Detail of Beam 8

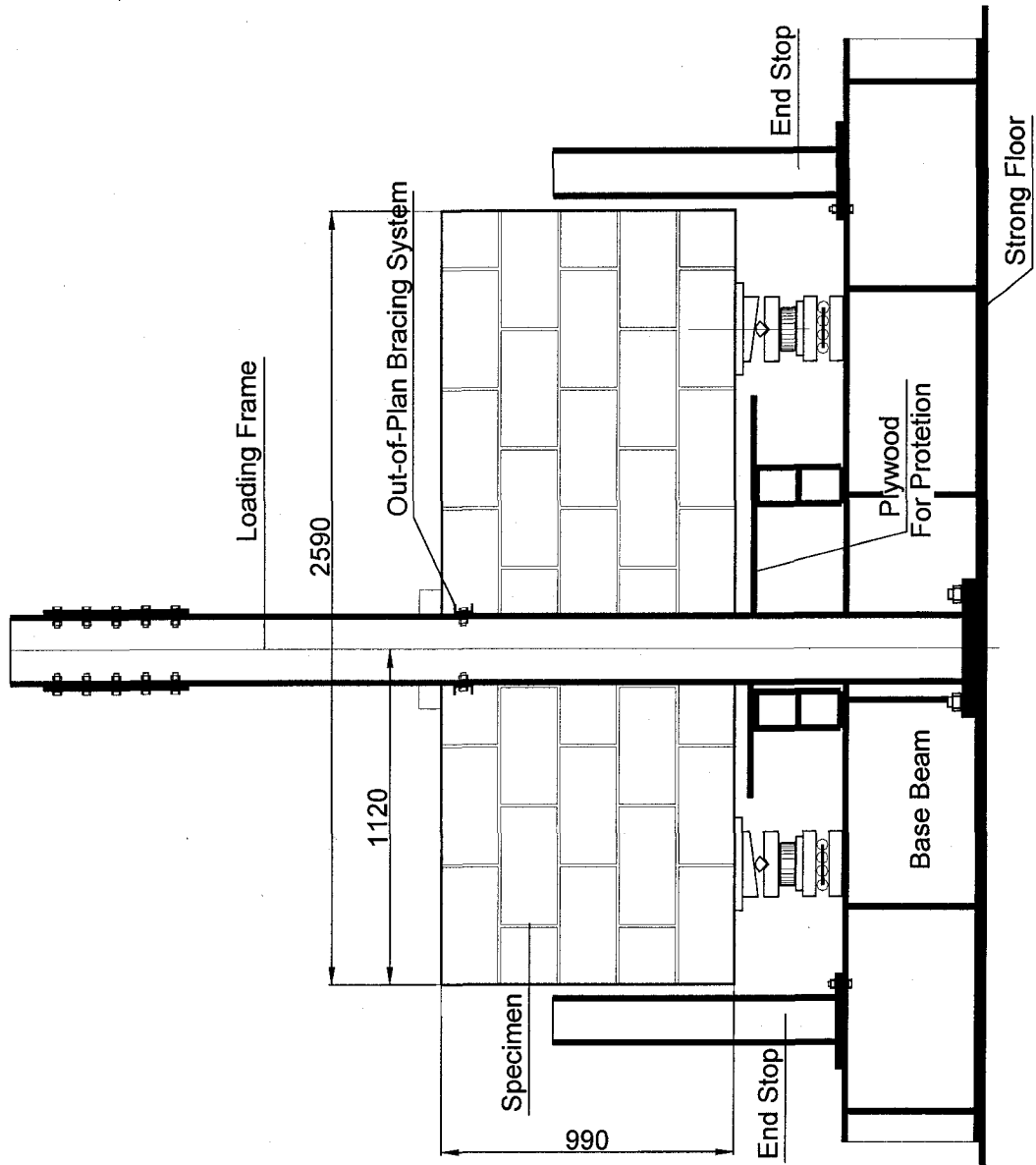


**Figure 3-10 Test Set-up**

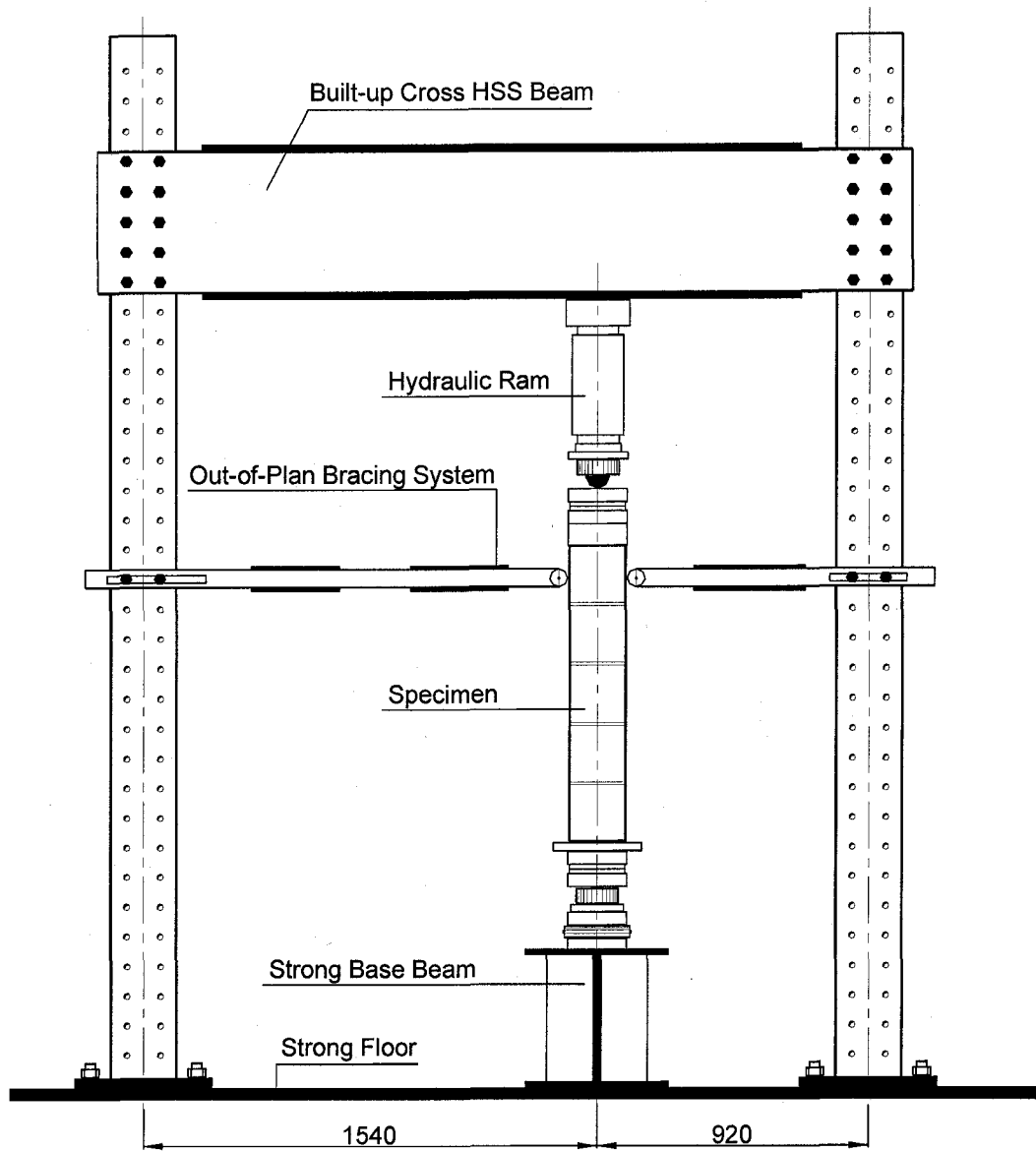


**Figure 3-11 Side View of Test Set-up**

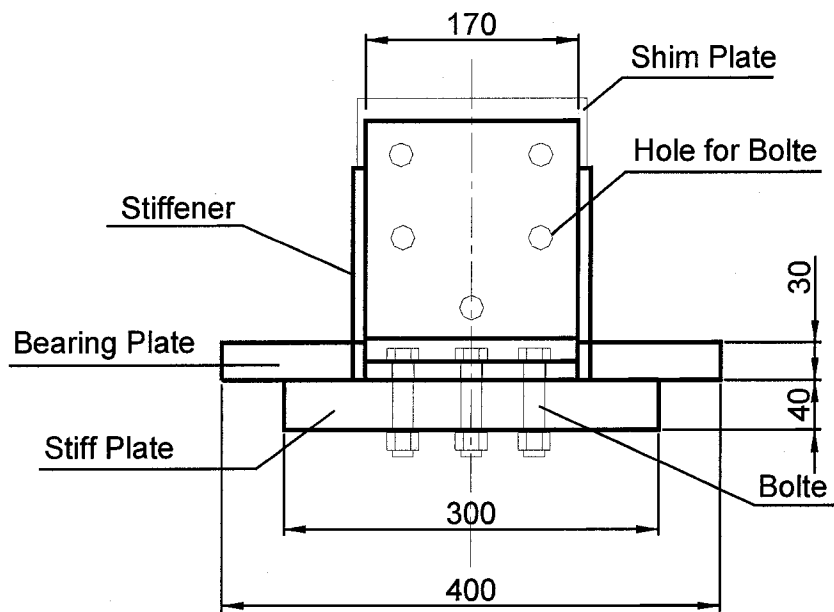
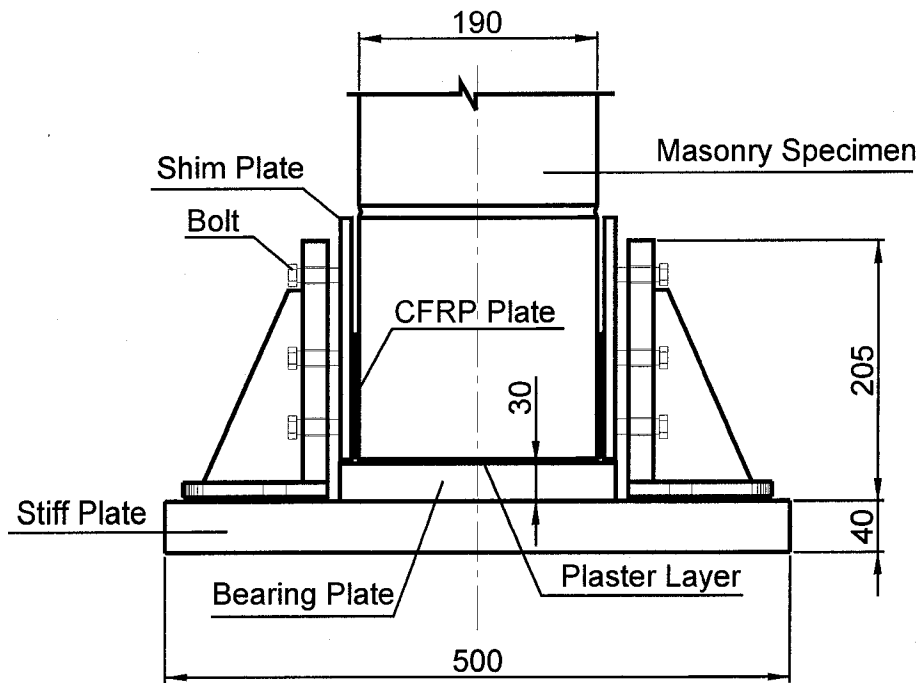


**Figure 3-12 Anchorage System for CFRP**

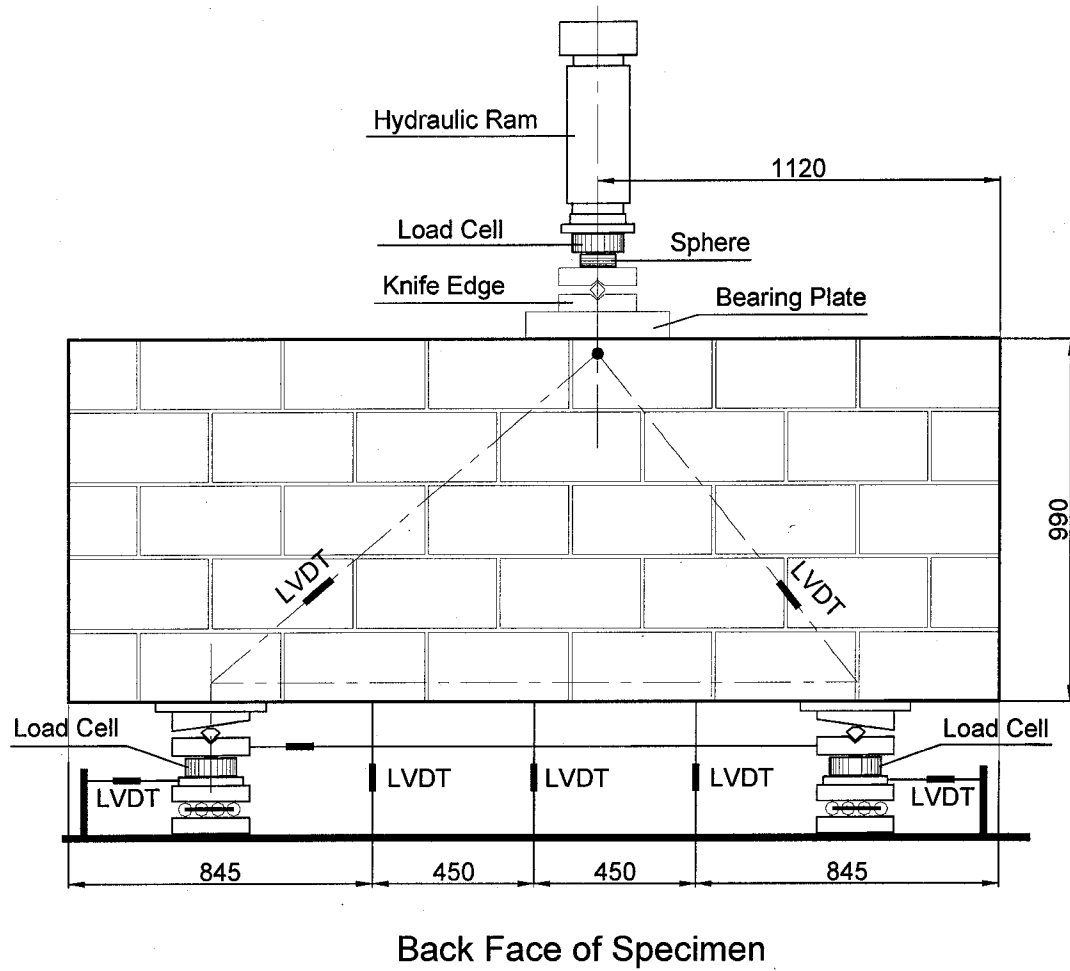


**Figure 3-13 The Layout of LVDTs and Load Cells**

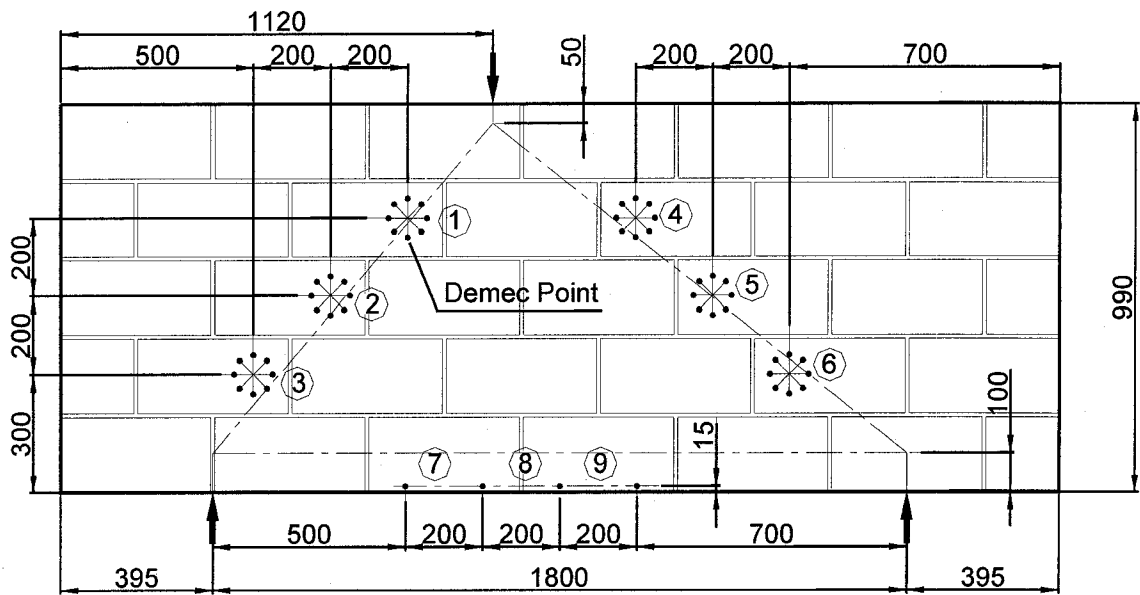


**Figure 3-14 The Layout of Demec Gauge Points**

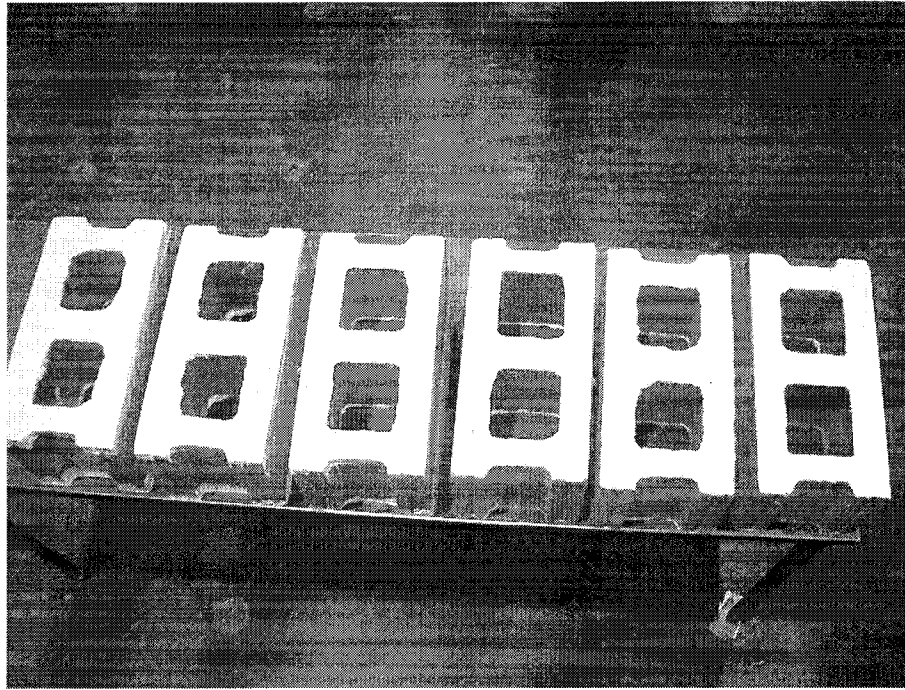


**Image 3-1 Capped Individual Masonry Unit Specimens**

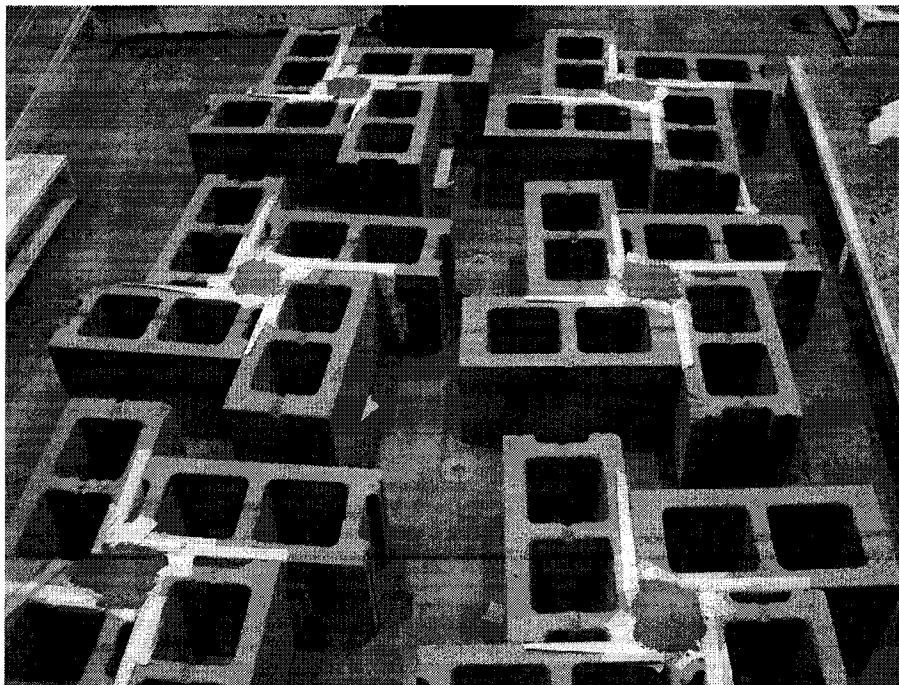


**Image 3-2 Construction of Grout Prism Specimens**

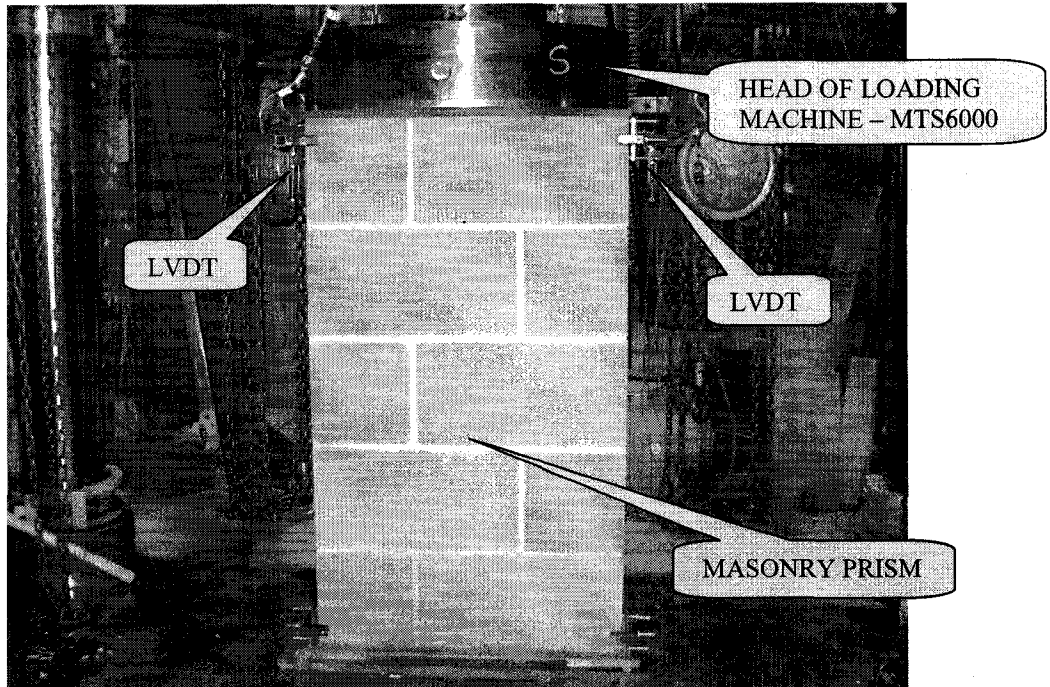


**Image 3-3 Test set-up for Grouted Masonry Prism**

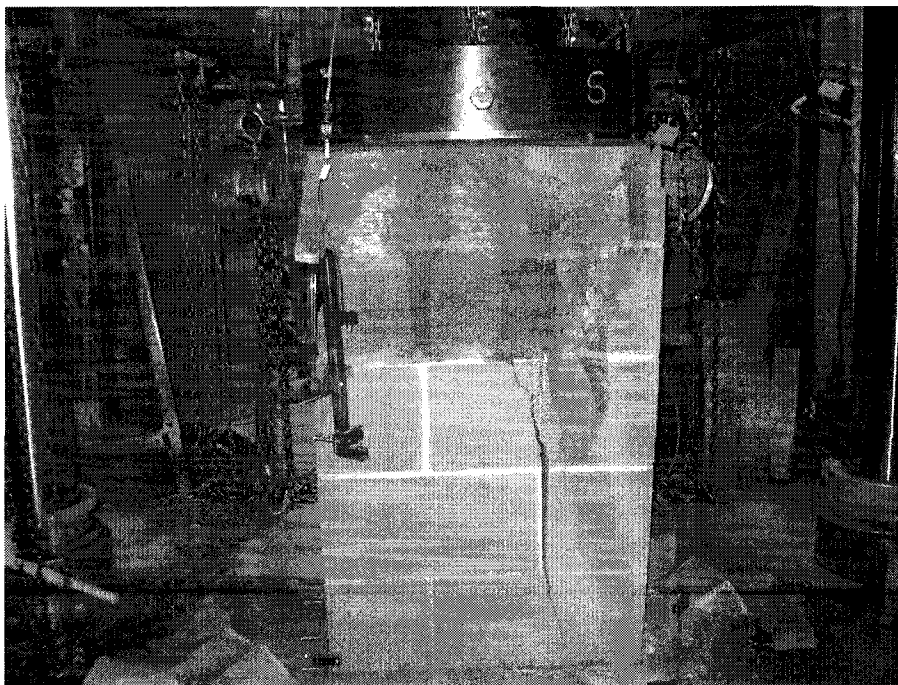


**Image 3-4 Typical Failure Mode of Grouted Masonry Prisms**

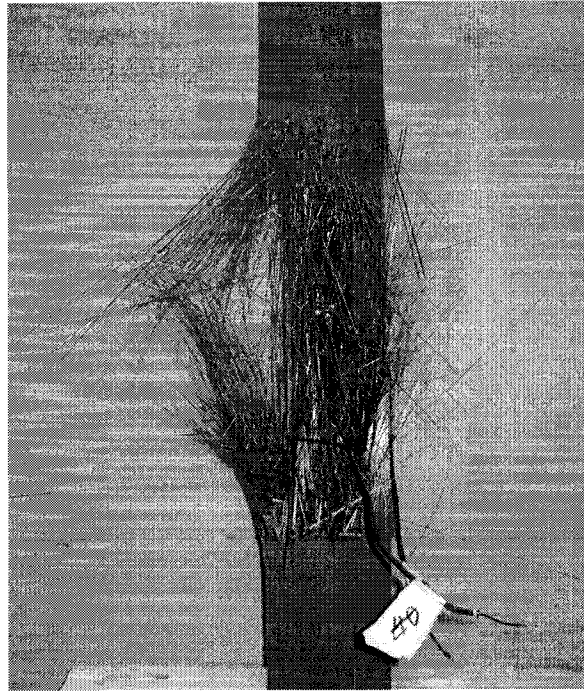


**Image 3-5 Typical Failure Mode of CFRP Plate Coupon**

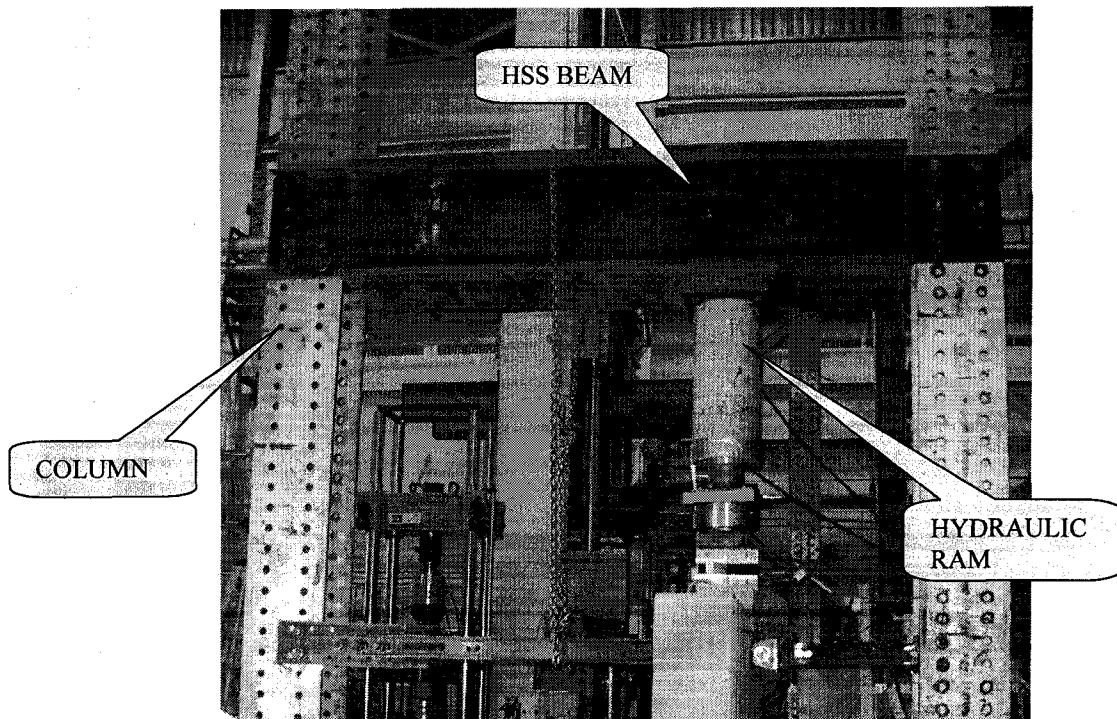


**Image 3-6 Loading Frame**

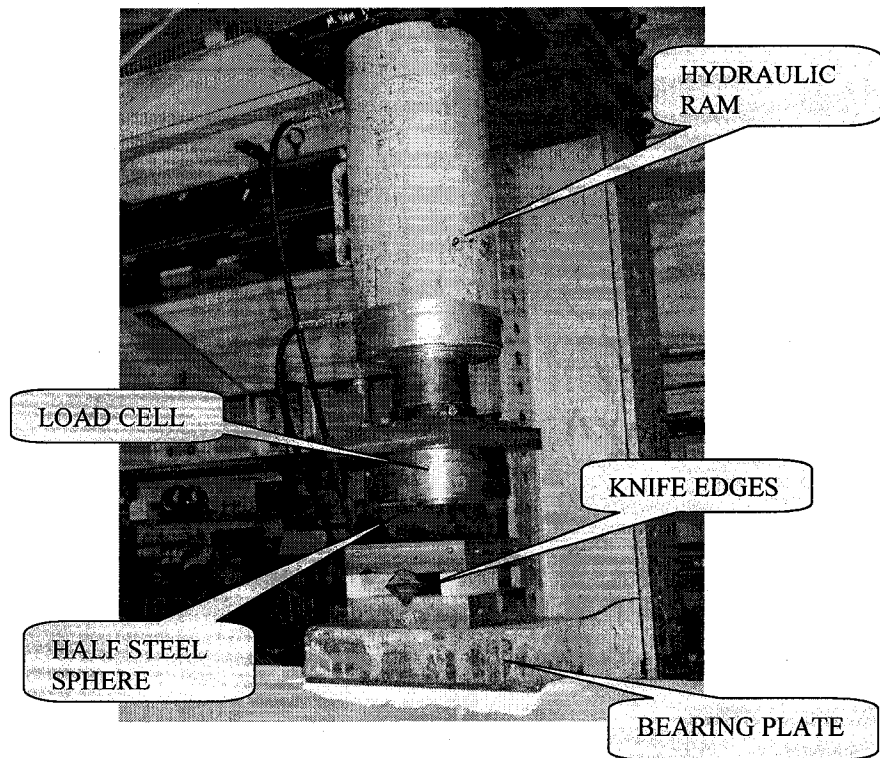


**Image 3-7 Top Loading System**

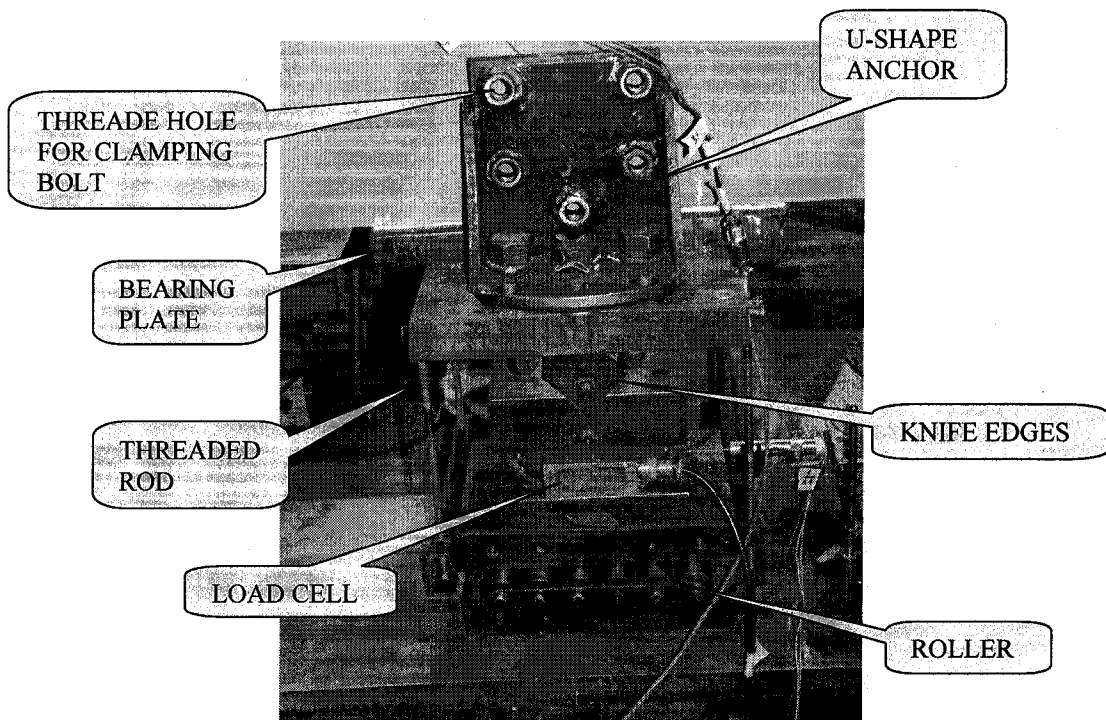


**Image 3-8 Bottom Reaction Assembled System**

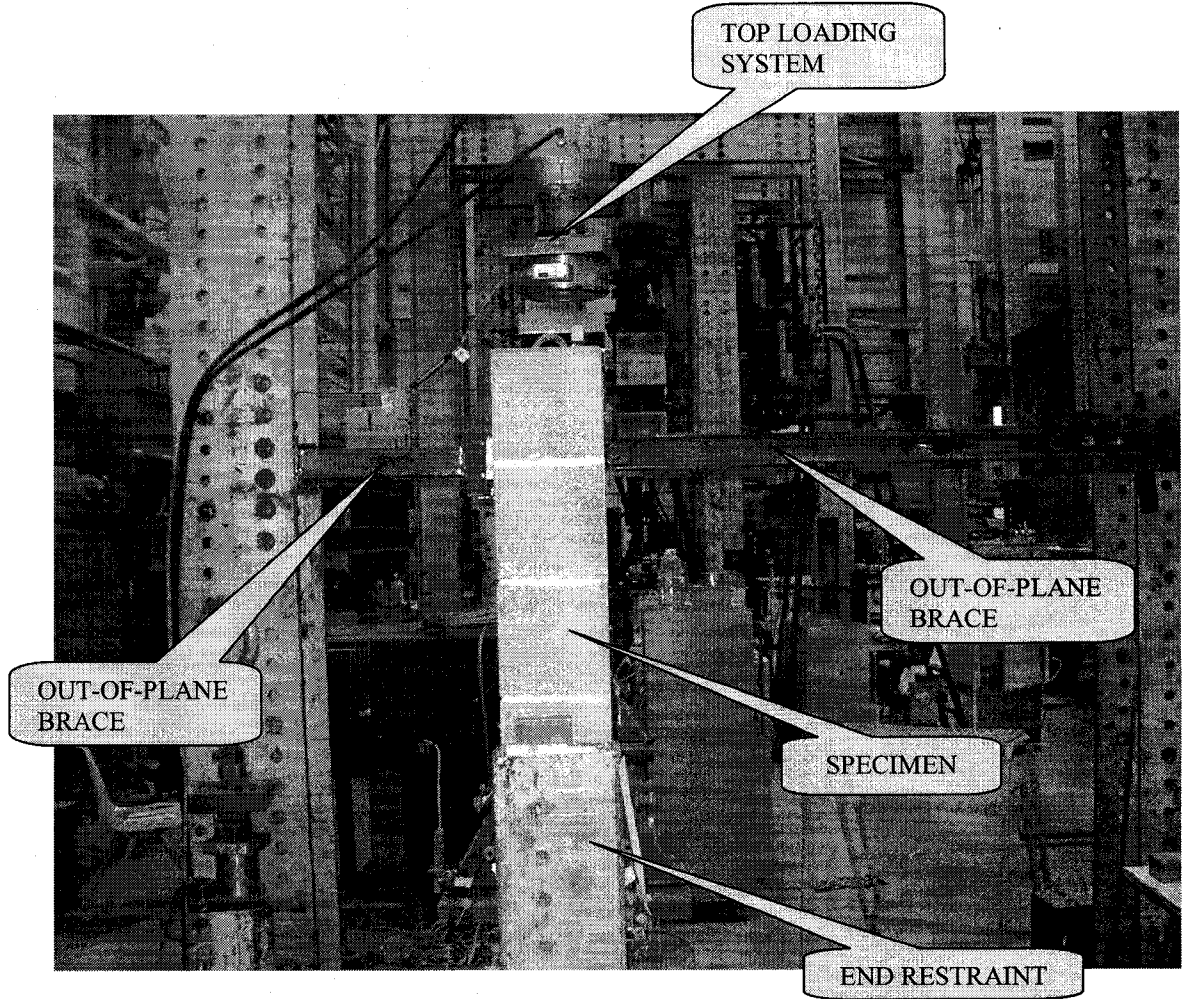
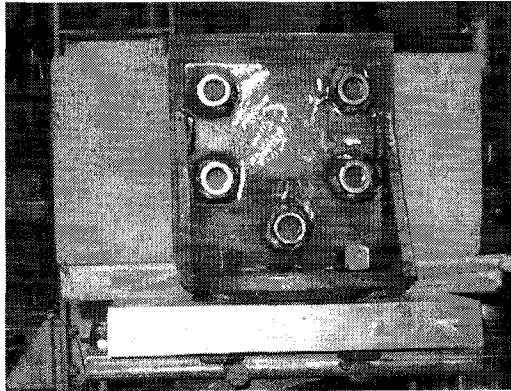
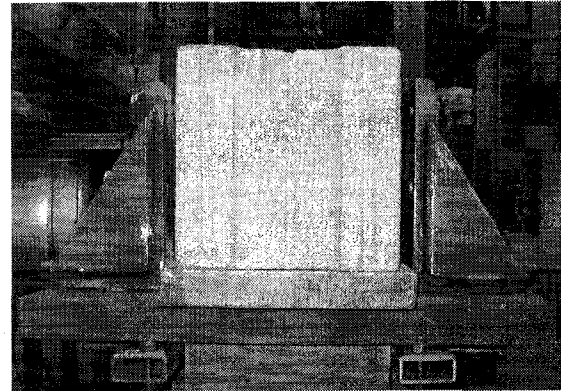


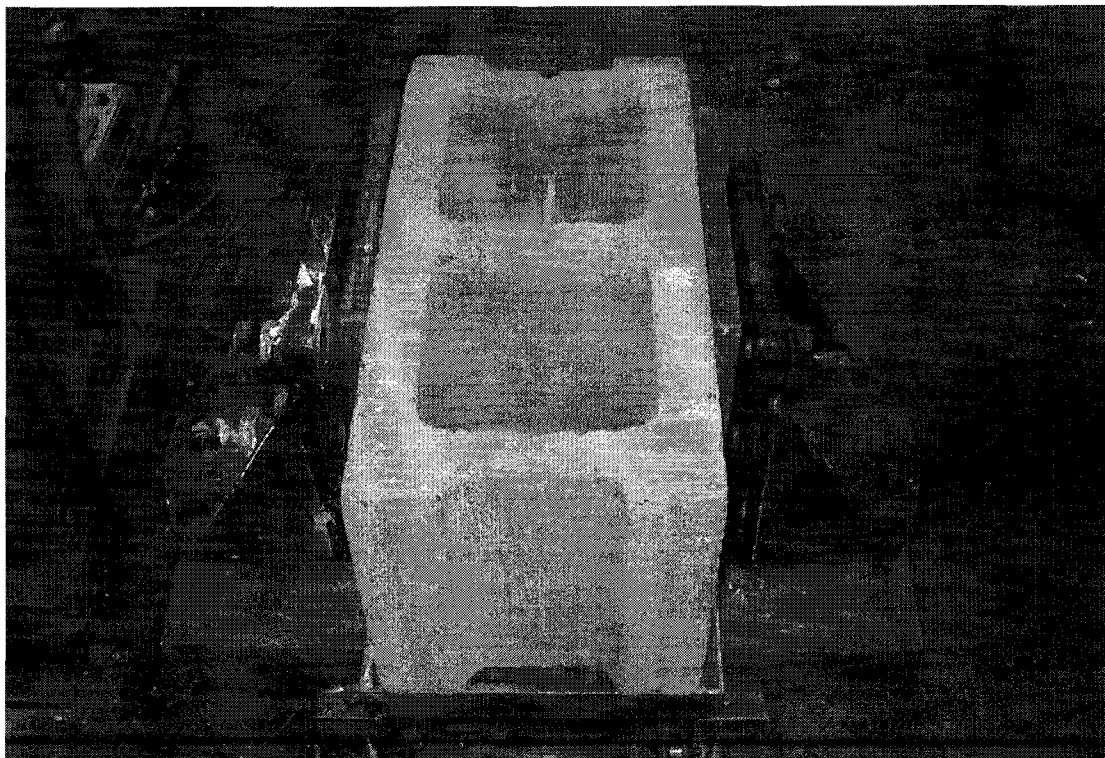
**Image 3-9 Out-of-Plane Bracing System**



**a) Front View of Anchorage System**



**b) Lateral View of Anchorage System**



**c) Top View of Anchorage System**

**Image 3-10 Anchorage System for CFRP Plates at Supports**

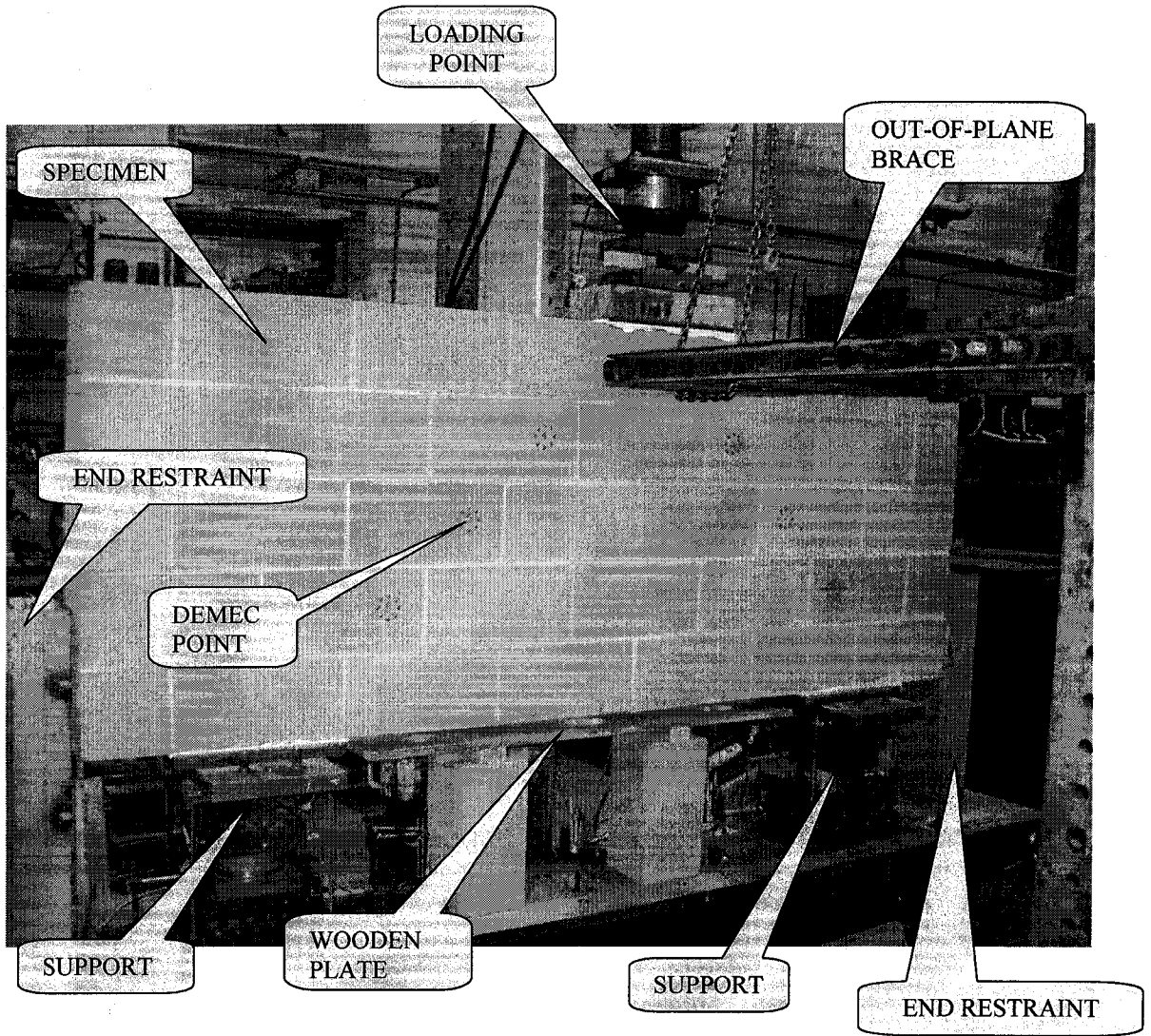


**Image 3-11 Test Set-up**

## 4. TEST RESULTS

### 4.1 Introduction

This chapter describes the observations during the test and the results obtained from the data collection system. The principal outputs of interest are the load-displacement response of the specimens, the tensile and compressive strains on three materials, namely, masonry, steel and CFRP, the system ductility and the overall behaviour of the specimens. In addition, the failure modes and the crack patterns are also identified.

### 4.2 Load-Displacement Response

Figures 4-1 through 4-8 illustrate the load versus mid-span displacement behaviour of eight specimens, respectively.

#### 4.2.1 Beam 1 (Control beam)

Designed as a reference beam for other specimens, Beam 1 was built without any strengthening strategy. During its construction, masons forgot to put joint reinforcement into the mortar joints. The instrumentation used was illustrated in Figure 3-14 and Figure 3-15. Quasi-static loading was applied to the beam monotonously. The Demec gauge reading was taken at intervals of 10 kN. Figure 4-1 shows the load-displacement relationship of Beam 1. Demec gauge values were taken at Point A, B, C, D, E and F. It can be seen that the load decreased a little while the readings were taken. The reason was that the sustaining loading caused a little deformation on the beam during the reading. When the load was reapplied, the stiffness of the specimen remained almost identical as before.

The Load-Displacement curve consists of two phases. The first phase starts from the beginning to Point H, at which the first visual crack appeared along the vertical mortar joint at the mid-span and the corresponding load was 59 kN. Point H to Point G belongs to the second phase. As can be seen, the slope of the line HFG was reduced since the stiffness of the beam was degraded due to the cracks. Furthermore, the deflection increased quickly under a small increment of the load after the crack formed. Shortly thereafter, the beam failed suddenly at a maximum load of 67 kN at Point G as seen in

Figure 4-1. According to the Load-Displacement curve, this beam was basically elastic before it failed and the specimen showed very little ductility, given that the maximum displacement was only 0.2 mm at mid-span. The crack patterns and the corresponding load were marked on the beam, and are presented in Image 4-1.

#### **4.2.2 Beam 2 (Reinforced with two No.15 steel rebars)**

As a regular deep beam, Beam 2 was reinforced with two No.15 steel rebars longitudinally at the bottom of the beam, as shown in Figure 3-4. Figure 4-2 illustrates the behaviour of the load versus mid-span displacement of Beam 2, and the response includes five distinguishing load stages. Demec gauge reading was taken at intervals of 50 kN until Point E. After Point E, the readings were taken according to the crack propagation since the stiffness of the specimen degraded quickly even under small increments of the load.

The first load stage terminated at Point B, and the corresponding load and displacement were 107 kN and 0.3 mm, respectively. Even though there were several tiny cracks observed along the vertical mortar joints at mid-span, the beam was basically elastic within this stage.

From Point B to E, these tiny cracks propagated and became wider with an increase in the load, and some new cracks also appeared, which caused the degradation in the stiffness of the beam. During this stage, the effective stiffness was nearly constant, as demonstrated in Figure 4-2.

At Point E, the first primary diagonal crack formed along the line joining the top loading point and the left support, corresponding to a load of 251 kN. This crack caused deformation increased quickly at mid-span and resulted in a load reduction. After the new mechanism stabilized, the beam could resist increasing loads until Point F, whereupon the second primary diagonal crack along the line connecting the loading point and the right support was observed. Similarly, a big reduction on the load and an increase in displacement were noticed. This loading phase ended at Point G with the load of 300 kN and a displacement of 2.4 mm. As can be seen, the slope of the line E-F-G was much flatter than at the initial stage.

The fourth loading stage started from Point G and ended at Point I, where the slope of the line G-H-I was higher than the line E-F-H. The reason is probably the higher loading rate within this loading stage. There were no new cracks observed except for a widening and extension of existing cracks.

The last segment of the loading started from Point I and ended at Point J. During this stage, the effective stiffness of the beam was rather low and even a slight increment of the load could cause a relatively big displacement at mid-span of the beam. The failure occurred at Point J, which corresponds to the maximum load of 357 kN and a displacement of 3.3 mm. It is evident that the ductility of Beam 2 is much more than that of Beam 1.

#### **4.2.3 Beam 3 (Reinforced with longitudinal and web steel rebars)**

As described in Section 3.3.2, Beam 3 was reinforced with two No.15 longitudinal steel bars and eleven No.10 web steel bars. Figure 4-3 illustrates the relationship of the load and the displacement at mid-span of the beam. There are six phases during the whole loading procedure with reference to the stiffness of the specimen.

The first stage (from Point A to Point B) corresponds to a load of 101 kN and a mid-span displacement of 0.2 mm. During this period, the response was basically linear, and two small vertical cracks along the mid-span mortar joints were observed.

From Point B to C, the response was different from the first phase in that the effective stiffness decreased a little. This was due to crack propagation and the appearance of new cracks. At Point C, (corresponding to a load of 329 kN and a displacement of 1.8 mm), two diagonal cracks formed along the lines between the loading point and the supports. As shown in Figure 4-3, a slight drop from Point C to C' was caused due to the sudden appearance of these two diagonal cracks.

After Point C', one notes the third phase of the response. It can be seen that the line C'D has nearly the same slope as the line BC. The flexural cracks extended slightly upward, whereas the diagonal cracks propagated rather rapidly during this loading stage. This type of crack propagation maintains the stiffness of the specimen. This loading stage ended at

Point D, at a load of 456 kN and a displacement of 3.0 mm. Meanwhile, the former diagonal cracks extended to both the supports and some new diagonal cracks appeared.

A new equilibrium was achieved after a slight decrease in the stiffness from Point D to D'. The slope of the line D'E was flatter since the cracks spread very quickly in this period. When the load approached 477 kN at Point E, all cracks reached the bottom of the top layer of masonry blocks, as shown in Figure 4-3. Furthermore, this distribution of the cracks caused a further degradation in the stiffness of the specimen. It may be seen that the curve has a big drop at Point E in Figure 4-3. After checking the strain, it emerged that the tensile steel reinforcement at the bottom of the beam yield around this load level. As the widths of the cracks got bigger, the stiffness of the beam was further reduced until Point F. The load and mid-span displacement corresponding to Point F were 514 kN and 11.9 mm, respectively. Meanwhile, it was observed that the south end of the beam hit the south end restraint since the cracks at mid-span increased a lot and both supports were pushed outwards, as shown in Image 4-7. This contact provided an unexpected end confinement to the beam and induced it to carry higher loads. As can be seen, Point G shows the maximum load of 536 kN. In order to observe the catastrophic failure, the specimen was unloaded so that the south end restraint could be shifted away from the specimen safely. Thereafter, the specimen was reloaded until final failure. The response of Beam 3 indicates a lot of ductility, as evidenced by the maximum mid-span displacement of the beam (28.4 mm).

#### **4.2.4 Beam 4 (Strengthened with two CFRP plates of 100 mm width)**

As shown in Figure 3-6, a piece of Sika S1012 CFRP plate was externally bonded onto each side of Beam 4 at the bottom. The load versus mid-span displacement behaviour of this beam is presented in Figure 4-4, and the overall response can be divided into 3 sections.

The first section extends from Point A to B, and the behaviour of the beam in this portion is primarily linear. The first crack appeared at the mid-span vertical mortar joint at the load of 136 kN. Due to the propagation of the crack, the stiffness of the beam dropped slightly. When the load approached Point B, the mid-span crack quickly spread towards the loading point. This resulted in a slight decrease in the stiffness at Point B,

corresponding to a load of 186 kN and a deflection of 0.6 mm. There was only a visual crack inspected in this loading stage. It may be seen that externally bonded FRP could delay the emergence of the first crack.

The second loading stage starts from Point B and ended at Point C. Many new cracks emerged during this loading stage: some cracks were along the vertical mortar joints and some just crossed the masonry blocks. All the cracks extended towards the top loading point. It is worth mentioning that the debonding between CFRP plates and the surface of the masonry blocks happened at the region closest to the north support when the load exceeded 260 kN. Similarly, when the load reached 288 kN, delamination occurred at the region closest to the south support. Furthermore, a diagonal crack between the top loading point and the south support formed at Point C with the load of 295 kN as shown in Figure 4-4. The load-displacement response within this loading stage indicates that the stiffness of the specimen reduced gradually along with the propagation of cracks and the increasing of the load. The drop in the load and the increase in the displacement (from Point C to D) heralded the onset of premature failure by further extension of debonding along the CFRP plates.

For the sake of preventing premature failure, an anchorage system was employed to squeeze the CFRP plates onto the masonry surface at both support regions. This system is illustrated in Figure 3-12, wherein each bolt was given a torque of 50 foot-pounds (68 N.m). After tightening the bolts of the anchorage system, the specimen was capable to carry higher loads. As presented in Figure 4-4, a new loading segment starts from Point D and ends at Point E. The maximum load at Point E is 592 kN, and the related mid-span displacement is 6.1 mm. During this loading phase, the existing cracks continued to enlarge and spread, and a few new cracks formed as well. Especially, the debonding extended from one support to the other. Finally, a primary diagonal crack between the loading point and the south support emerged, which ran through the section and resulted in an abrupt failure, whereas, the CFRP plates were in good condition. It can also be seen from this curve that the load-displacement response within this loading stage is basically linear despite the gradual propagation of the cracks. It is evident that effective stiffness of the beam beyond Point D was constant until final failure.

#### **4.2.5 Beam 5 (Strengthened with two pieces of 50mm wide CFRP plates)**

As seen from Section 4.2.4, the CFRP plates used to strengthen Beam 4 were more than enough since the stress and strain on CFRP plates at failure were much lower than the ultimate stress and strain of this material. Therefore, the amount of CFRP adopted in the Beam 5 was reduced to half, resulting in two Sika S512 CFRP plates, as displayed in Figure 3-7.

Figure 4-5 illustrates the response of the load versus the mid-span displacement of Beam 5, and the whole loading procedure comprised of five sections: AB, BC, CD, DE and FG.

The first portion ends at Point B, corresponding to a load of 32 kN and a displacement of 0.2 mm. As may be observed, the slope of line AB is flatter than that of line BC. This may be caused by false displacements under the rather low load level due to a compaction between the specimen and the three loading points.

During the loading region BC, there was no crack observed and the specimen remained basically elastic. The load versus mid-span displacement response was chiefly linear. Point C corresponds to a load of 106 kN and a displacement of 0.4 mm.

The first crack along the mid-span vertical mortar joint was observed at a load of 120 kN, and this crack developed upward about 3 layers as the load increased to 135 kN. This loading phase ended at Point D, where the load was 145 kN and the displacement was 0.8 mm. As noticed, the effective stiffness of the specimen dropped due to the development of cracks.

The fourth loading stage, DE, shows a rather low stiffness since the debonding started at 148 kN at mid-span and extended towards both supports rapidly. The load at Point E increased by only 21 kN over that of Point D, whereas, the displacement increased to 1.5 mm, which was almost twice that at Point D.

It can also be seen that two drops in the load occurred from Point E to Point F. The first drop was caused by the appearance of two inclined cracks beside the primary flexural crack, and the second was due to rapid debonding between the CFRP plates and the specimen. The peak load at this stage was 184 kN.

Now, in order to prevent early failure from delamination of the CFRP plates, an anchorage system was introduced at the load of 170 kN in the support region, and every bolt in these anchors was applied a torque of 50 foot-pounds (68 N.m). As a consequence of introducing the anchorage system, the specimen was able to resist much higher loads, as shown in

Figure 4-5. From Point F to Point G, the load-displacement response was basically linear, and the effective stiffness was higher than that from Point D to E, but, slightly lower than that from Point C to D. The beam failed abruptly due to debonding of CFRP plates as they peeled off from both ends of the masonry surface. This corresponds to Point G, which is at a load of 387 kN and a displacement of 6.1 mm. The reason for this abrupt failure is probably the lack of the clamping force provided by anchors at both support regions.

#### **4.2.6 Beam 6 (Strengthened with two pieces of 50mm wide CFRP plates)**

As described in Section 3.3.2, Beam 6 was also reinforced with two S512 CFRP plates at the bottom, similar to Beam 5. However, unlike Beams 5, the anchorage system was employed at the beginning of the test in Beam 6, in order to delay the premature debonding between the CFRP and the masonry surface. Furthermore, the torque on each bolt to hold the CFRP plates in position was increased to 100 foot-pounds (135 N.m) from the 50 foot-pounds (68 N.m), previously seen for Beam 5. Figure 4-6 shows the relationship between the load and the mid-span displacement for Beam 6. There are three distinguishing sections during the entire loading procedure, as follows.

Initially, up to Point B, the curve follows the slope of line AB very well, and the behaviour of the beam under the load is basically linear. At Point B, with the load at 118 kN, the first crack emerged at mid-span and it caused a slight drop in the load-deflection response.

The second loading stage may be said to start from Point B and end at Point F. Major cracks and debonding were observed during this period. When the load reached 137 kN at Point C, debonding started in the region closest to the south support and two inclined cracks (in the form of steps) appeared, which spread along the mortar joints and cut

through the masonry blocks, then, converged with the primary flexural crack at mid-span. As can be seen in Figure 4-6, the effective stiffness of the specimen was much lower as a result. When the load reached 147 kN at Point D, debonding occurred at the region closest to the north support and progressed slowly towards the north support. This load increment manifests a rapid increase in the midspan displacement beyond Point D for even small load increments. It was reflected on the response curve that the mid-span displacement of beam after Point D was increased rapidly under a small load increment. At Point E with the load at 168 kN, debonding extended into the support region and it caused the load to drop to 159 kN, which relates to Point F in the figure. Comparing with the initial loading stage, the load increased by 50 kN, while the mid-span displacement was about 8 times greater (from 0.3 mm to 2.8 mm) during this loading stage.

From Point F to G in Figure 4-6, the response of the load versus the mid-span displacement during the third loading segment is seen. Here, the behaviour of the beam is chiefly linear and elastic except for a slight reduction on the stiffness of the beam due to the propagation of the cracks. The maximum load was 401 kN at Point G and the related mid-span displacement was 8.6 mm. As with Beam 5, Beam 6 failed suddenly by delamination, with the CFRP plates peeling off at both ends of the beam.

#### **4.2.7 Beam 7 (Strengthened with CFRP plates and steel reinforcement)**

As mentioned in Section 3.3.2, Beam 7 was strengthened with two S1012 CFRP plates at the bottom and eleven No.10 steel rebar in the masonry web cores. As with that in Beam 6, the anchorage system was employed at the beginning, and a torque of 100 foot-pounds (135 N.m) was applied on each clip bolt. The relationship between the load and the displacement of Beam 7 is presented in Figure 4-7. The three main loading stages are distinguished by the three straight lines, namely, line AB, CD, and EF.

Line AB depicts a linear elastic response between the load and the displacement. When load exceeded 58 kN, which corresponds to Point B, the effective stiffness of the specimen was reduced. This can be induced by the formation of interior cracks in the masonry or smaller cracks covered by the CFRP plates, where the tensile stresses are maximum.

Most cracks emerged during the second loading phase, which starts from Point C and ends at Point D. During this phase, a gradual reduction in the effective stiffness of the beam occurs due to the formation and propagation of these cracks. At Point D (Load = 324 kN), debonding between CFRP plates and masonry progressed into both support zones and caused a slight drop in the load between Point D and E, as shown in Figure 4-7.

With the third loading stage between Point E and F, the curve exhibits linear characteristic even though lots of inclined cracks were formed at the mid-span region during this loading stage. At Point F, the load reached 722 kN, and the mid-span displacement was 8.4mm. The final failure load was 730 kN and the beam ruptured at mid-span of the beam because of the debonding the CFRP plates from the surface of the beam at both ends. It can also be seen that the failure is abrupt and brittle.

#### **4.2.8 Beam 8 (Strengthened with CFRP plates and sheets)**

Beam 8 was strengthened with two Sika S1012 CFRP plates at the bottom of the beam and twenty-two CFRP sheets at the web of the beam as shown in Figure 3-9. Before starting the test, each clip bolt of the anchorage system was tightened with a torque of 100 foot-pounds (135 N.m) to prevent premature debonding. As illustrated in Figure 4-8, the behaviour of the beam under a monotonically increasing load can be divided mainly into four distinct phases.

Within the first phase, from the beginning to Point B, the curve was basically linear, and the specimen behaved elastically. The load and displacement related to Point B were 73 kN and 0.5mm, respectively. After Point B, a small reduction in the stiffness of the beam was noticed, and this may be attributed to the formation of small cracks under the CFRP plates.

When the load reached Point C (with the load at 147 kN), the first visible crack appeared at the mid-span vertical mortar joint. It developed upwards and became the primary flexural crack with an increase in the load. Around 240 kN, some small inclined cracks came into view, and debonding emerged at the region closest to the north support at 280 kN. When the load reached 328 kN at Point D, the main diagonal crack formed between the top loading point and the south support, corresponding to a slight lose of stiffness.

There was a gradual drop in the stiffness due to the appearance of cracks and progressive delamination between the CFRP plates and the surface of the masonry during this loading stage.

The third loading stage extends from Point E to Point F. During this period, the load-displacement response is rather linear although there are indications of the emergence of new cracks. This loading stage ends at Point F (Load = 550 kN; displacement = 6.2mm), when a large diagonal crack appeared between the top loading point and the north support. Corresponding to this, a slight increase in the displacement (from 6.2 mm to 6.4 mm) and a significant drop in the load (from 550 kN to 508 kN) were observed from Point F to G.

The last stage of loading extended from Point G until failure. As shown in the curve, the stiffness dropped step by step until the beam lost the ability to carry the load. The failure was abrupt as the two web CFRP sheets peeled off and the cross section of the beam ruptured along the diagonal crack. The maximum load at Point H was 585 kN, and the related displacement at mid-span was 7.5mm.

### **4.3 Strain Behaviour**

Since masonry is not ideally suited for the application of electrical strain gauges, Demec gauge points were employed to monitor the strain distribution on the surface of the masonry. Meanwhile, electrical strain gauges were used to measure the strain profile along steel reinforcement and the CFRP plates.

The ratio of the clear span  $l_n$  (1400 mm) to the overall depth  $d$  (990 mm) is less than 2 for all the specimens. According to CSA A23.3 Cl.10.7.1, the deep beam action must be considered, which means that a significant amount of load is carried directly from the load point to the supports by compression struts. Therefore, the critical locations of the specimens are two diagonal struts and the region between the two supports. As illustrated in Figure 3-14, the “rosette” of Demec gauge points (position 1~6) were located roughly along the lines joining the load point and the supports, and 200 mm Demec gauge points (position 7~9) were arranged at the extreme bottom edge at mid span.

### **4.3.1 Beam 1**

As Beam 1 had no strengthening material within, the readings taken from the Demec gauges in diagonal struts show that the principal compressive stresses and the principal tensile stresses were rather low. According to the strut-and-tie model, the tensile force was carried by the lowest layer of masonry blocks, grout and mortar joint, all of which have little capacity to carry the tensile force. Crack formation took place at 60 kN and the beam failed immediately with a load of 67 kN. At location 8, the readings of the Demec gauge, which were mounted on two different masonry blocks, gave a much bigger value than the ones at locations 7 and 9. The reason is that a crack formed along the vertical mortar joint between two Demec gauge points at location 8. The readings of Demec gauges at locations 7 and 9 on the other hand were nearly constant, which means the changes on strain and stress over there were very slight.

### **4.3.2 Beam 2**

Since two M15 steel rebars were placed at the bottom of the specimen to strengthen the beam, the load capacity and the ductility of Beam 2 were significantly improved. As seen from Demec gauges at location 2, the strain perpendicular to the line joining the load point and the left support underwent a big jump after the crack formed and crossed this rosette. Whereas, the readings on Demec gauges at positions 1,3,4,5 and 6 showed very little change. When the load reached 84 kN, the reading on the Demec gauge at location 8 increased substantially when the first crack crossed the mortar joint in between. At the load of 150 kN, two new flexural cracks appeared across the Demec gauges at locations 7 and 9 respectively. As a result, the readings of the Demec gauges at Locations 7 and 9 increased significantly.

Figure 4-9 shows the load versus strain response of the bottom steel reinforcement. As it can be seen, the specimen has higher stiffness in the phase AB because there was no crack in the specimen. After point B, the cracks appeared and the bottom tensile force was carried by steel reinforcement only. The response from Point B to C is elastic and indicating that the load was carried by the steel reinforcement. The maximum strain on the steel reinforcement was 2025 microstrains and the corresponding load was 357 kN, which was the maximum load for Beam 2. After point C, the masonry blocks in the

region of the left strut were crushed and the specimen failed. The strain dropped proportionally and there was no plateau in the load-strain response, which means that the steel reinforcement had not yielded when the beam failed.

### **4.3.3 Beam 3**

Based on the data from Demec gauges, the load versus strain response in Beam 3 shows identical relationship with Beam 2. The readings of Demec gauges increased extremely when cracks occurred between Demec gauge points, and the orientation of the strain on the specimen switched once the cracks formed.

The behaviour of load versus strain on the bottom steel reinforcement is illustrated in Figure 4-10. There are four distinguishing stages divided by three points. Within the stage AB, the bottom steel reinforcement and masonry worked together to carry the tensile force, and the specimen exhibited a higher stiffness. After point B, the propagation of cracks caused masonry to fail to carry tension force and all the load was carried by the bottom steel rebars. Hence, the strain on the rebar saw a significant increase even though the load remained almost constant. Point D corresponds to a strain of 2679 microstrains and a load of 476 kN. The bottom steel reinforcement yielded beyond this load as seen in the Figure 4-10.

### **4.3.4 Beam 4**

Beam 4 was strengthened with two 100 mm CFRP plates at its bottom. Similarly, Demec gauges were mounted on the surface of the masonry to observe the strain distribution at different regions of the specimen. According to the data taken, the readings of the Demec gauges, whose orientation was parallel to the lines joining the load point and bottom supports, decreased with an increase in the load. On the other hand, the reading on those Demec gauges, whose orientation was perpendicular to the axes of the compressive struts, increased with an increase in the load. Furthermore, as expected, the appearance of the cracks caused the redistribution of the stress in the specimen. Consequently, the readings of the Demec gauges were affected: some strains got larger while others were reduced.

Figure 4-11 shows the load-strain relationship at different gauge locations along the CFRP plates. Setting the north end of the beam as the reference point, the distances of

each strain gauge measured from this reference point were marked on the X-axis. Each curve represents the distribution of the strain along the CFRP plates at a certain load level. The maximum strain (4995 microstrains) on the CFRP plates occurred at a distance of 2100 mm from the north end of the beam is much lower than the limited tensile strain (14700 microstrains) of the CFRP plate. The strain distribution between the two supports becomes more uniform as the load increases. Moreover, the strain died out very quickly from the inner edge of the support plate to the outer edge. It was noticed that the strains on the FRP plates were very small before the cracks appeared. At a distance of 100 mm from the end of the beam, the strain was close to zero. Clearly, the FRP plates applied at this location do not offer much help although the development length of the CFRP plate was higher than that required.

#### **4.3.5 Beam 5**

There is no large difference in the data from the Demec gauges between the final and the initial readings at the diagonal strut regions. It is because the primary flexural crack at mid-span progressed upwards too quickly and reached the highest mortar joint under a relatively low level of load, in this case 150 kN. Meanwhile, debonding between CFRP plates and masonry started at mid-span and propagated towards the two supports rapidly. There was no crack crossing the Demec gauge points at the diagonal strut regions.

The strain profile of CFRP plates for increasing loads is shown in Figure 4-12. Here, similarly, the X-axis denotes the distance of each strain gauge measured from the north end of the beam. These five plots describe the strain distribution along the CFRP plates under the load of 200 kN, 250 kN, 300 kN, 350 kN and 387 kN, respectively. It is clear that the strain at 100 mm from the north end of the beam is nearly zero, no matter what the load is. The values of the strain at the anchorage regions decrease rapidly, while the strains at mid-span remain relatively high. The maximum strain along the FRP plates was at the inner edge of the south support (equal to 6446 microstrains). The load corresponding to this strain was 387 kN.

### **4.3.6 Beam 6**

The behaviour of Beam 6 is almost the same as Beam 5. The readings from the Demec gauges in the region of the diagonal strut registered very small changes during the test, and there was no crack crossing those Demec gauge points. However, a large increase on the readings of Demec gauges at location 8 was noticed when a vertical crack appeared at the vertical mortar joint.

Figure 4-13 illustrates the distribution of the strain along the bottom CFRP plates under various loads. The maximum strain of 7072 microstrains was located at the mid-span of the beam and the corresponding load was 401 kN. Strains within both end anchorage zones dropped rapidly. Similarly, the strains in the extra developing length of FRP plates were nearly zero. At the time of failure, the tensile strength of CFRP plates (approximate 1.3 GPa) was the way lower than the specified tensile strength (2.8 GPa).

### **4.3.7 Beam 7**

Compared to Beam 4, the data from Demec gauges in the compression struts of Beam 7 present a similar behaviour: the data from the Demec gauges parallel to the axes of the compressive strut dropped with an increase in the load. On the other hand, those perpendicular to the axes of the diagonal strut increased slightly for increasing load. Overall, the readings in the Demec gauges in the strut regions changed only slightly.

The strain distribution along the length of the CFRP plates under different load levels is presented in Figure 4-14. When the load was relatively lower, the values of strain present considerable changes only at the mid-span, while the strains close to the two support regions were affected very slightly. As the load increased, the strain profile between the two supports became more uniform. The maximum strain on the CFRP plates was 7284 microstrains, which occurred under the loading point at the mid-span for a load equal to 730 kN. Similarly, the strains on the CFRP plates dropped very quickly within the anchorage zones, and the tensile strains close to the ends of the beam were nearly zero even though the load was significantly higher.

The data obtained from the strain gauges on the web steel reinforcement shows that the vertical steel reinforcement acted as a tension tie to help the masonry to resist the shear

and the tensile forces at the certain zones. Furthermore, the width of the cracks was relatively smaller due to the existence of web reinforcement. This was as expected.

#### **4.3.8 Beam 8**

The readings of Demec gauges along the compressive struts recorded slight changes before the diagonal cracks crossed the Demec points. The data from the Demec gauges attached to the web CFRP sheets demonstrated that the vertical CFRP sheets did carry some tensile force. These vertical CFRP sheets also caused the web stress distribution to be more uniform and in addition, delayed the emergence of the cracks at the web.

The load versus strain response along the CFRP plates at the bottom of the specimen is illustrated in Figure 4-15, where each curve represents the strain profile under a certain load. As can be seen, at the load of 200 kN, the strain at mid-span reached 1422 microstrains, whereas the strains at the regions close to the two supports were very little (only 42 microstrains). With an increase in the load, the strain progressed gradually towards both the supports from the mid-span. At failure, (with the load equal to 585 kN), the maximum strain recorded at mid-span was 5545 microstrains. The strains on the CFRP plates descend rapidly within the support region.

#### **4.4 Crack Pattern and Failure modes**

Crack patterns and critical locations of all eight specimens are shown in Image 4-1 through Image 4-30. All images shown here were taken from the west side of the specimen during the test. In order to highlight the cracks, they have been marked out along with the corresponding load levels. Crack patterns for the same specimen under different load levels are presented in order to illustrate the propagation of former cracks and the emergence of newer ones. There were several kinds of cracks observed in these photographs, such as the stepped cracks along the mortar joints, crack splitting or spalling in the masonry units, crack splitting in the face shell of masonry blocks from the grouted core, and debonding or peeling off between CFRP plates and the masonry surface. In addition, the failure mode for each specimen is discussed in this section.

#### **4.4.1 Beam 1**

Image 4-1 shows the crack pattern for Beam 1 after failure, where only one primary crack was observed. This crack was inspected at the mid-span vertical mortar joint when the load was about 57 kN. With an increase in the load, this crack grew upward rapidly and split the masonry blocks above until it reached the bottom of the top bearing plate. The beam failed by flexure as the compressive zone of the cross-section disappeared. The failure was brittle and sudden with the corresponding load at 67 kN. Since there was no longitudinal reinforcement in the beam, the strut-and-tie mechanism could not be formed after the beam cracked.

#### **4.4.2 Beam 2**

The crack pattern in Beam 2 after failure is presented Image 4-2. As expected, the crack distribution was in keeping with the typical crack pattern of a deep beam, where the primary cracks are along the diagonal direction since the shear action in the beam web causes compression in the diagonal direction and tension in the direction perpendicular to that. The first three vertical cracks along the lowest mortar joints between two supports were observed at around the load of 84 kN. Then, the primary crack at the mid-span progressed more quickly than the other two cracks along the adjacent mortar joints. When the load reached 150 kN, two more vertical cracks formed by splitting the masonry blocks at bottom of the beam. With an increase in the load, all these cracks progressed towards the load point, and stopped growing when the load reached 220 kN. The first stepped crack was observed in the region close to the north support at the load of 250 kN and it extended towards the loading point by splitting a corner of a masonry unit with an increase of the load. At the load of 283 kN, the second stepped diagonal crack appeared along the line joining the loading point and the south support as showed in Image 4-2. These stepped cracks developed fast and became the primary diagonal cracks. At a load of 350 kN, another inclined crack occurred below the previous diagonal crack.

Failure occurred after the primary diagonal crack developed fully in the strut zone, and the masonry blocks were crushed at the region near the top loading point and spalled at the middle of the strut, corresponding to a load of 357 kN. Image 4-3 clearly displays the

spalling zone in Beam 2. The failure mode of this beam can be defined as the failure of the compression strut.

#### **4.4.3 Beam 3**

Image 4-4, Image 4-5 and Image 4-6 describe the crack patterns in Beam 3 under the load of 400 kN, 480 kN and 536 kN, respectively. The first crack was observed along the mid-span vertical mortar joint at a load of 84 kN. With an increase in the load, several vertical cracks appeared between supports. These cracks initially progressed upward, and then inclined towards the loading point. As increasing in the load, the deep beam action was getting apparent. The compression in the diagonal struts caused tension in the direction perpendicular to the axis of compressive struts. When the load approached 270 kN, the first of the diagonal cracks emerged, which was below the axis of the compression strut. Two primary diagonal cracks along the compression struts were observed at the load of 320 kN, as shown in Image 4-4. The flexural cracks stopped extending at the load of 220 kN and started growing again when the applied load exceeded 450 kN (Image 4-5). Furthermore, diagonal cracks and flexural cracks developed and reached the highest horizontal mortar joint. Meanwhile, lots of small cracks appeared at the bottom layer of masonry blocks.

As seen in Image 4-6, when the maximum load of 536 kN reached, primary cracks were fully developed and this beam failed along with crushing of the top loading zone. The crack pattern at failure is coincident with that of reinforced concrete deep beam. The failure of Beam 3 belongs to a combination of shear-compression failure and flexural failure. Image 4-8 presents a typical crushing of the top-loading zone, in which the face shells of the masonry unit were split from the grouted core.

#### **4.4.4 Beam 4**

The crack patterns in Beam 4 under 3 different load levels (300 kN, 500 kN and 592 kN) are shown in Image 4-9, Image 4-10 and Image 4-11, respectively. The propagation of the cracks can be observed clearly from these photos.

As shown in Image 4-9, the first crack was observed along the mid-span vertical mortar joint at a load of 136 kN. There was no other visible new crack until 200 kN, and only the

first crack proceeded upward and reached the second highest layer of masonry blocks. After 200 kN, three new cracks occurred at the bottom of the beam and extended upward vertically. With an increase in the load, these cracks converged towards the loading point. At a load of 240 kN, two primary inclined cracks were formed along the axes of compression struts due to the tensile stress caused by the compression thrusts between the load and the reactions. Debonding between the CFRP plates and the surface of the masonry was first noticed at a location close to the north support when the load approached 260 kN.

It can be seen in Image 4-10 that the two primary diagonal cracks were developed through the regions between the top loading point and bottom supports at a load of 500 Kk and more debonding along the CFRP plates showed up.

Image 4-11 shows the crack pattern at failure. It is evident that the widths of all the cracks are bigger than before and the region close to the top loading point was crushed. According to the crack pattern, the failure mode may be classified as shear-compression failure. The typical debonding between CFRP plates and masonry is displayed in Image 4-12.

#### **4.4.5 Beam 5**

Image 4-13 shows the crack propagation of Beam 5 at a load level of 150 kN. The first crack, which formed at the mid-span along the vertical mortar joint, was observed when the load reached 120 kN. With an increase in the load, this crack progressed rapidly upward by splitting the masonry units above, and it almost reached the lower mortar joint of the top masonry layer at 150 kN. The initial delamination between CFRP plates and masonry started from the mid-span at the load of 148 kN, and it spread very quickly towards both supports. As can be seen in Image 4-14, debonding developed towards the anchorage system at the supports while the corresponding load was 180 kN. Thanks to the anchorage system, the debonding stopped and the beam was able to resist the increasing applied load. As the load increased, there was no other visible crack and only the flexural crack at mid-span became progressively wider.

Failure occurred suddenly at a load of 387 kN along with the peeling off and debonding between CFRP plates and masonry at both ends of the beam. Image 4-14 presents the crack pattern of Beam 5 at failure, where the failure can be regarded as flexural failure associated with anchorage failure. The typical modes of peeling off and debonding between CFRP plates and masonry surface are illustrated in Image 4-15 and Image 4-16, respectively.

#### **4.4.6 Beam 6**

Crack pattern in Beam 6 at a load of 150 kN is presented in Image 4-17. Two cracks at mid-span were observed at around 125 kN, one along the vertical mortar joint and the other splitting the masonry block at the middle. The latter developed very quickly upward and it reached the top layer of masonry blocks at a rather low level of load, (137 kN). Meanwhile, debonding initiated at the region close to the south support, and a stepped crack formed beside the primary flexure crack. At a load of 141 kN, another region of debonding was observed close to the north support. Both debonding regions progressed towards the ends of the beam.

Image 4-18 illustrates the distribution of cracks in Beam 6 when the load approached 350 kN. There was no major change in the crack arrangement except for an increase in the crack widths and the appearance of small inclined cracks at the mid-span of the beam.

Crack pattern in Beam 6 at failure is shown in Image 4-19. Similar to Beam 5, the failure happened abruptly with the CFRP plates peeling off from the masonry surface at both ends. It may be characterized as anchorage failure along with flexural failure. The typical mode of peeling off at the end of beam is shown in Image 4-20.

#### **4.4.7 Beam 7**

Similar to previous beams, the first crack of Beam 7 was detected along the vertical mortar joint at mid-span, as shown in Image 4-21. With an increase in the applied load, a few inclined or stepped cracks formed, all of which converged towards the primary flexural crack in the middle. Around 270 kN, debonding took place at the region close to north support, and developed along the CFRP plates. Image 4-22 shows the crack pattern at a load of 450 kN, and it can be seen that more inclined cracks occurred at the mid-span,

and the former cracks continued to extend. Whereas, the mid-span primary flexural crack ceased to develop upward. Crack pattern of Beam 7 at a load of 650 kN is illustrated in Image 4-23, where a fan-shaped crack zone was formed at the mid-span of the beam. Nevertheless, there is no primary diagonal crack found in the compression struts and all cracks were below the axes of compression struts. Image 4-24 is the crack pattern of Beam 7 at failure, and the related maximum load was 731 kN. As can be seen, a primary diagonal crack emerged rather late at a load of 725 kN due to web reinforcement employed, by which the compressive strength of masonry in the web was significantly improved. Similarly, Beam 7 failed by peeling off CFRP plates at both ends of the beam, and the failure was brittle and abrupt. Image 4-25 presents the typical zone where the peeling between the CFRP plate and the masonry surface happened.

#### **4.4.8 Beam 8**

The first crack of Beam 8 occurred along the mid-span vertical mortar joint at a load of 150 kN, as shown in Image 4-26. With increasing applied loads, this crack propagated upward rapidly until it reached the lower face of the most top layer of masonry at a load of 225 kN. During this increase in the load, four new vertical cracks were observed; two of them were along the mortar joint, the other two crossed the masonry blocks.

Image 4-27 shows the crack pattern at a load of 300 kN, in which it is noticed that the two main inclined cracks appeared on each side of the primary flexure crack at mid-span, and several discontinuous delaminations along the CFRP plates occurred at the mid-span and the region close to supports. When the load reached 450 kN, as seen in Image 4-28, the right side diagonal crack developed to the region near the bearing plate at the loading point. Meanwhile, lots of small inclined cracks emerged. On the other hand, the primary flexural crack at mid-span ceased to grow.

A primary diagonal shear crack, which is along the line joining the load point and the left support, appeared suddenly at the load of 550 kN, as illustrated in Image 4-29. During this load period, all the widths of inclined cracks increased, and the mid-span flexure crack started extending upward again. After the load reached 585 kN, one more diagonal crack in the right compression strut formed, which developed into the load zone. At the same time, a vertical CFRP sheet, which was crossed by this diagonal crack, debonded

suddenly and caused the failure of the beam, as presented in Image 4-30. The failure was abrupt and may be classified as a shear-compression failure. The crack pattern indicates that the significant amount of the load was transferred to both supports by the compression thrusts between the load and the reactions.

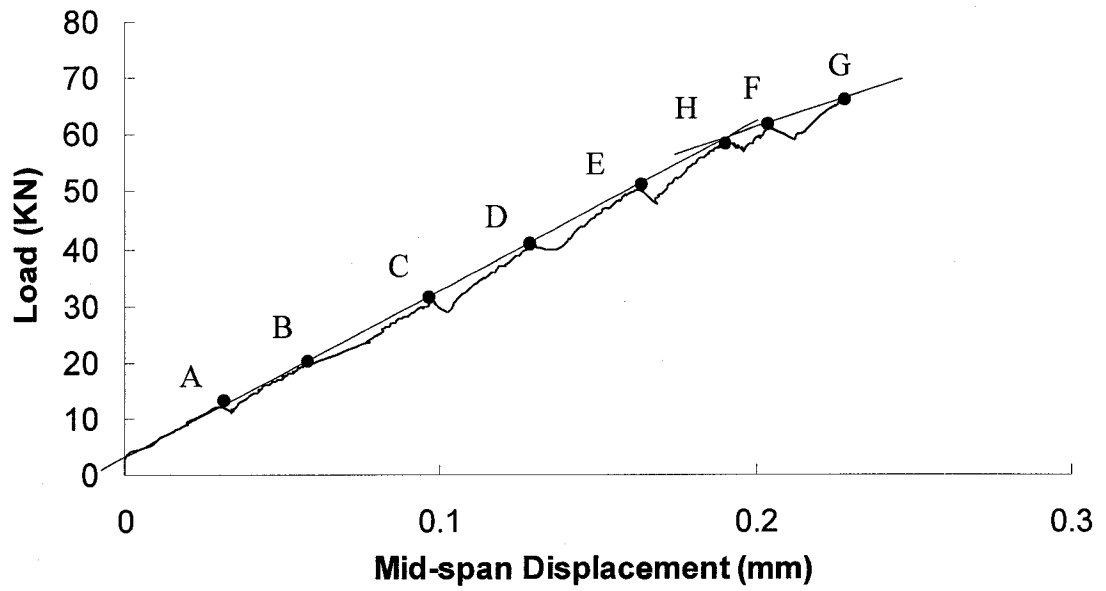


Figure 4-1 Load-Displacement of Beam 1

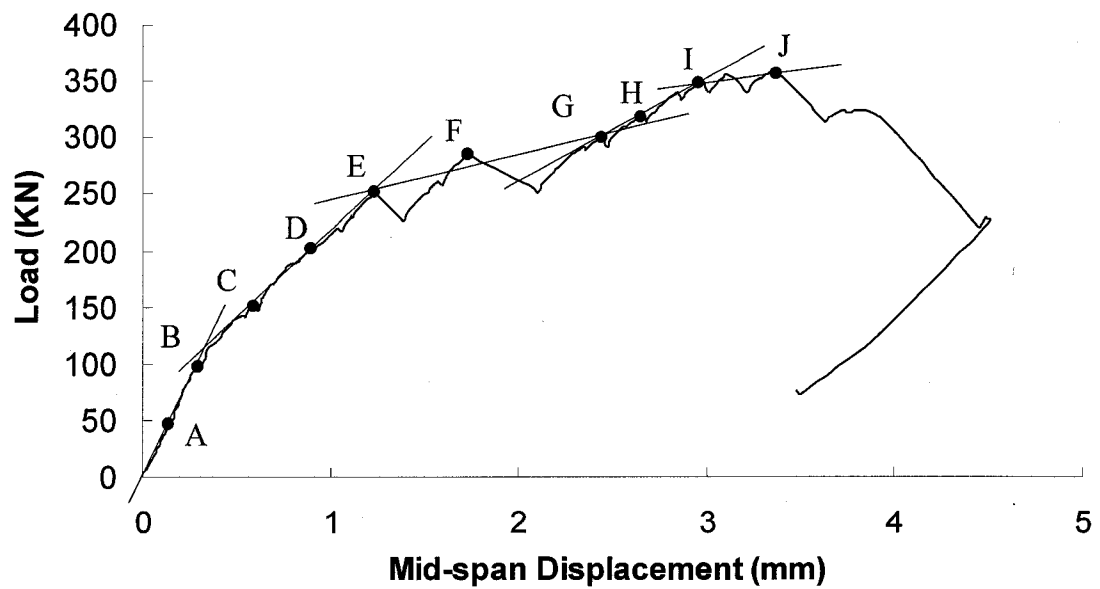
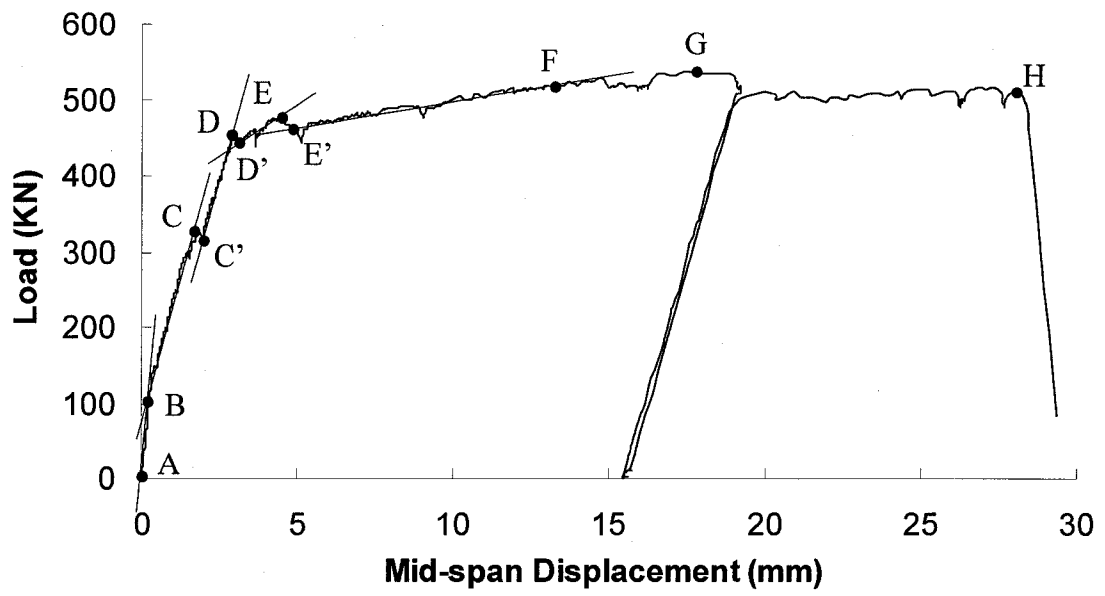
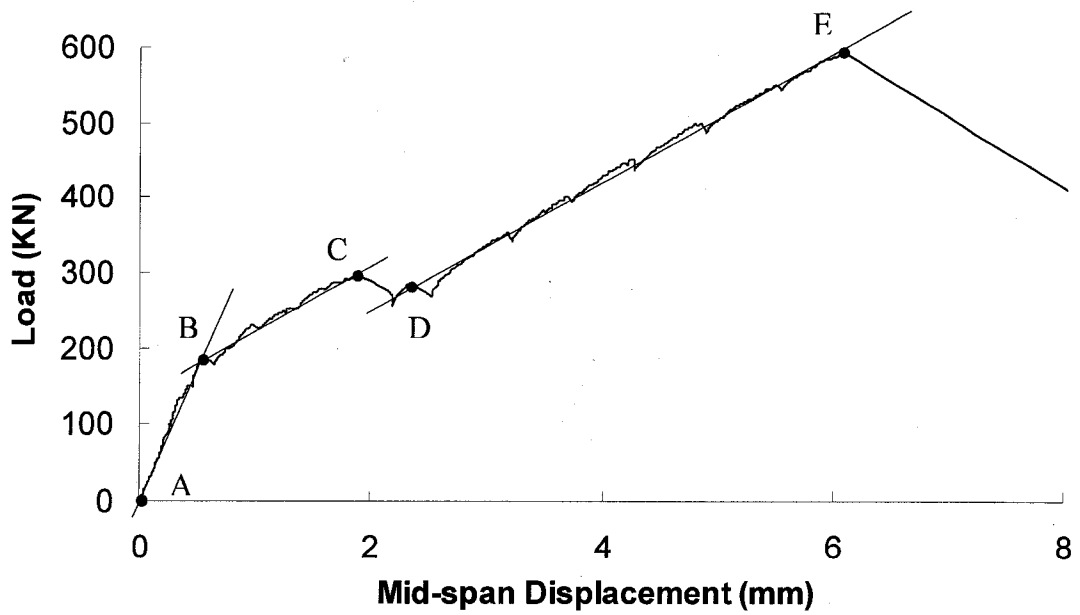


Figure 4-2 Load-Displacement of Beam 2



**Figure 4-3 Load-Displacement of Beam 3**



**Figure 4-4 Load-Displacement of Beam 4**

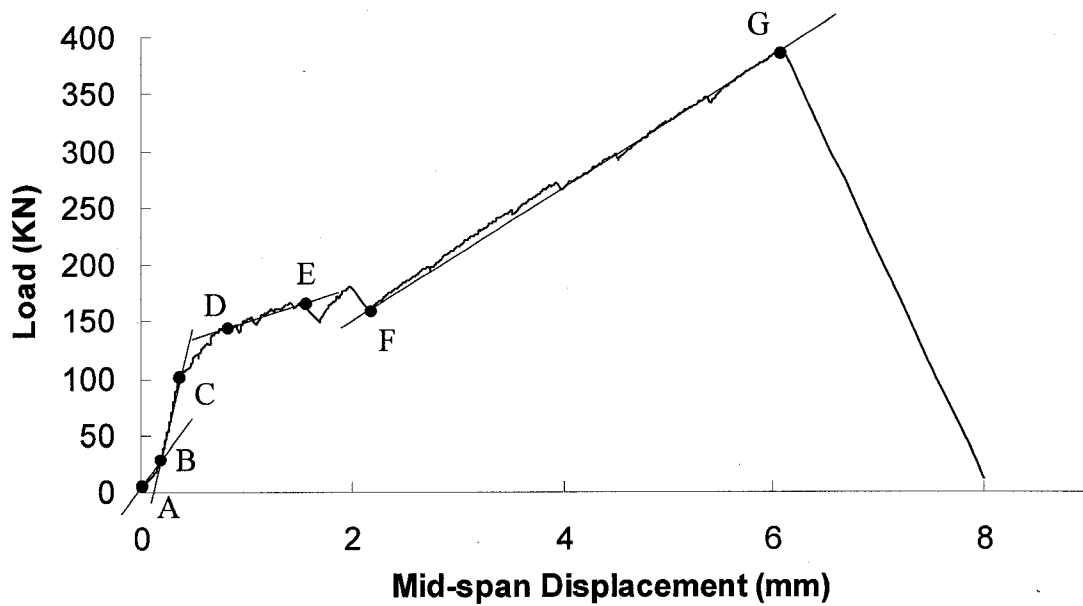


Figure 4-5 Load-Displacement of Beam 5

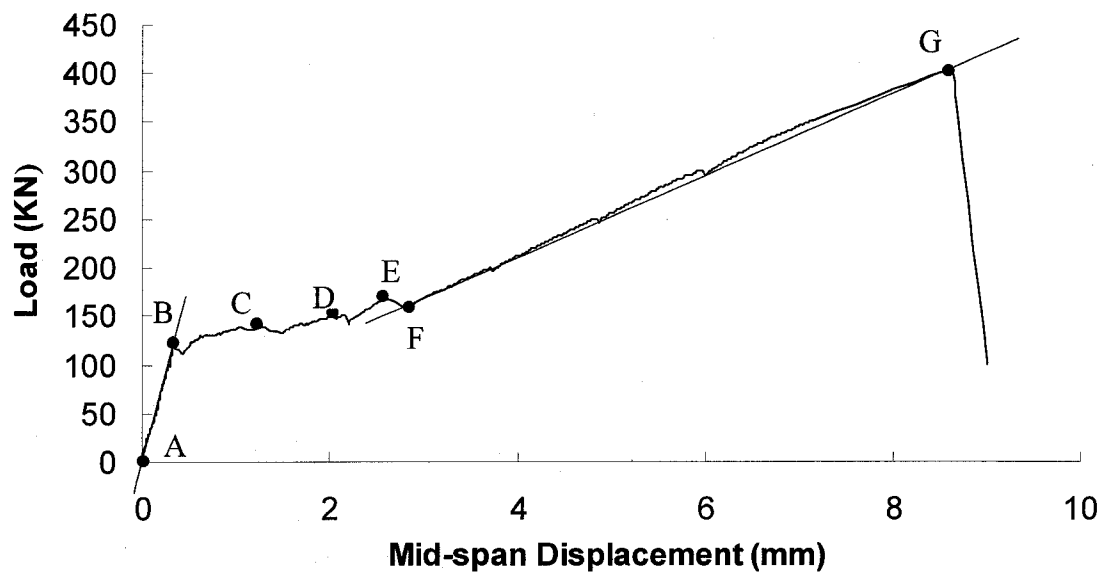


Figure 4-6 Load-Displacement of Beam 6

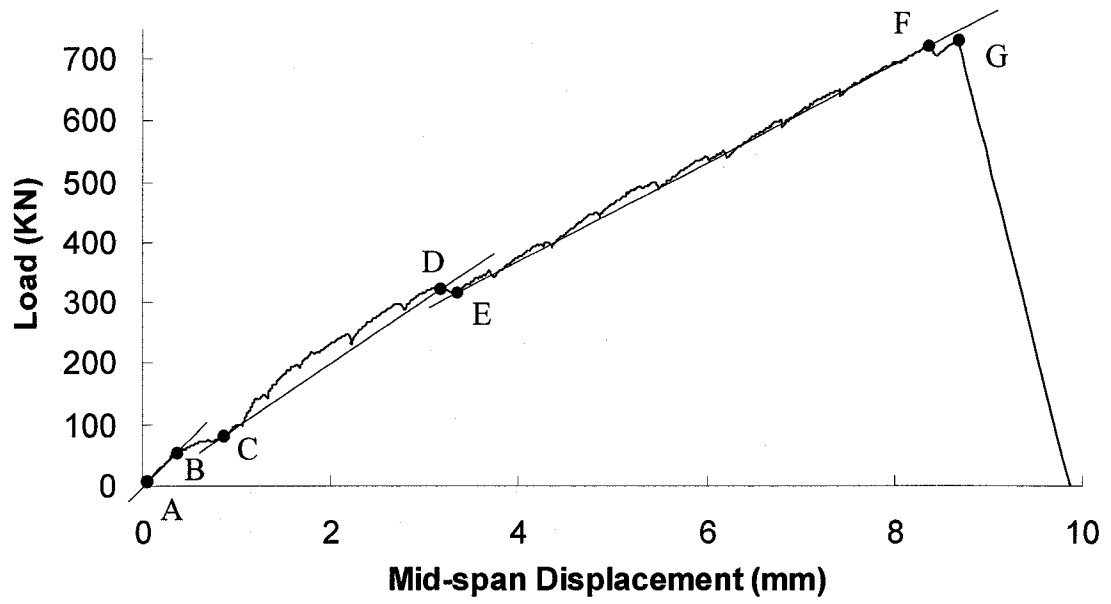


Figure 4-7 Load-Displacement of Beam 7

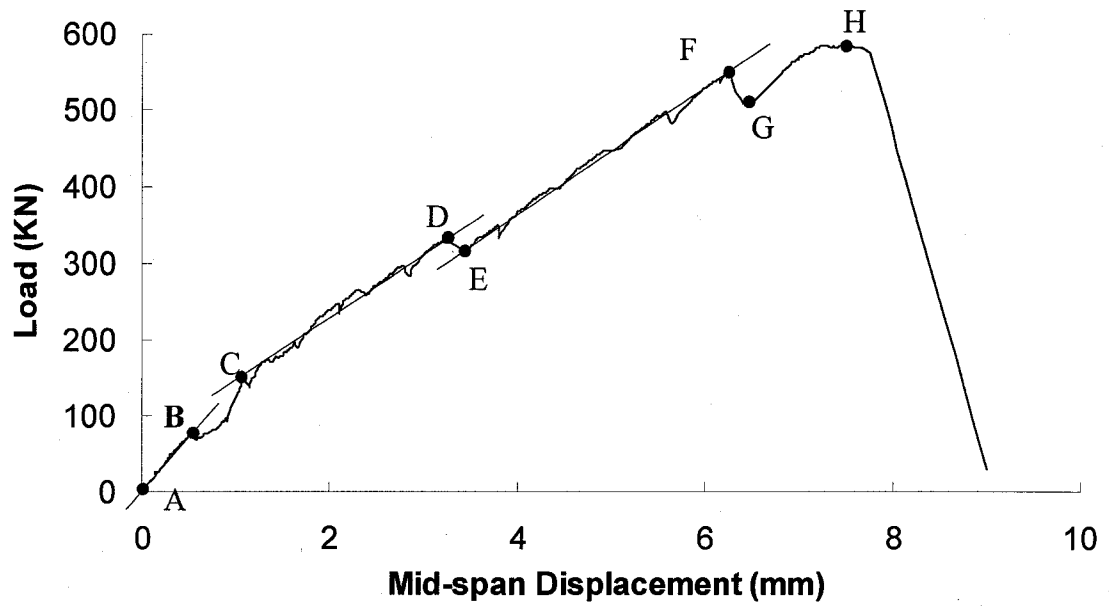
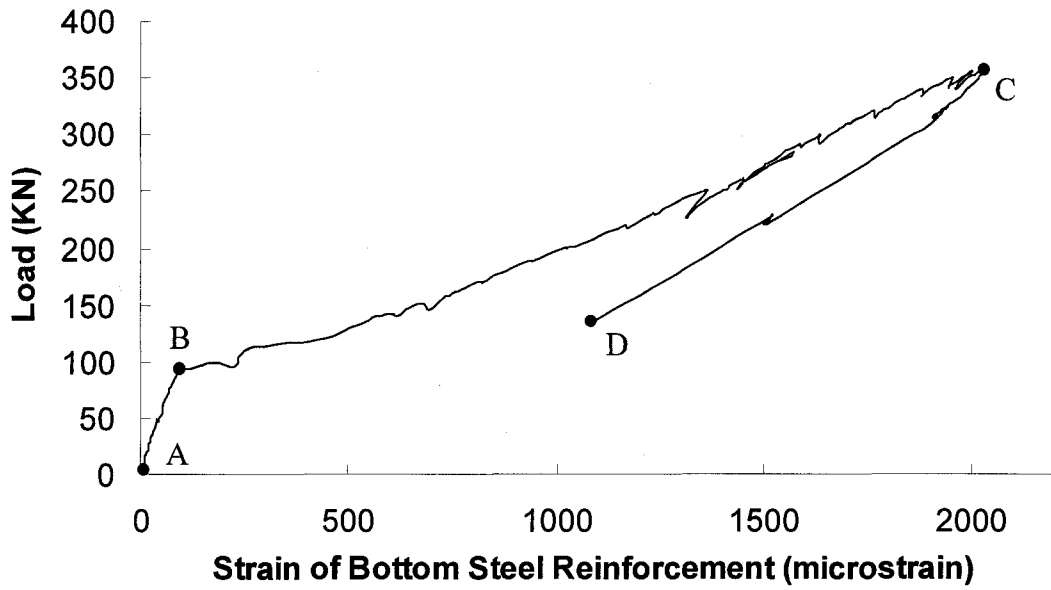
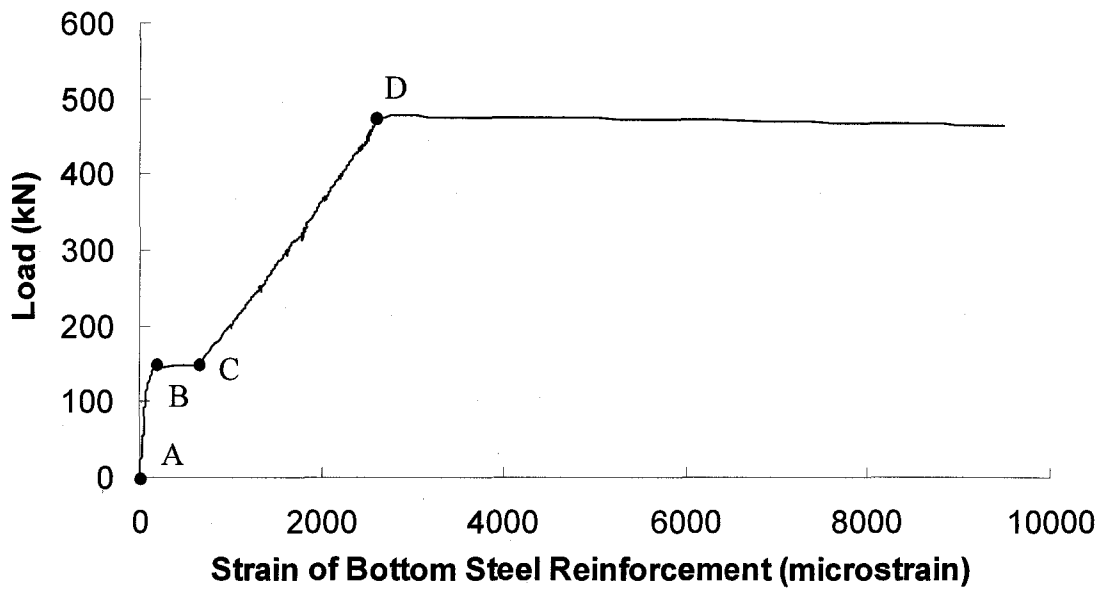


Figure 4-8 Load-Displacement of Beam 8



**Figure 4-9 Load - Strain on Bottom Steel Reinforcement of Beam 2**



**Figure 4-10 Load-Strain on Bottom Steel Reinforcement of Beam 3**

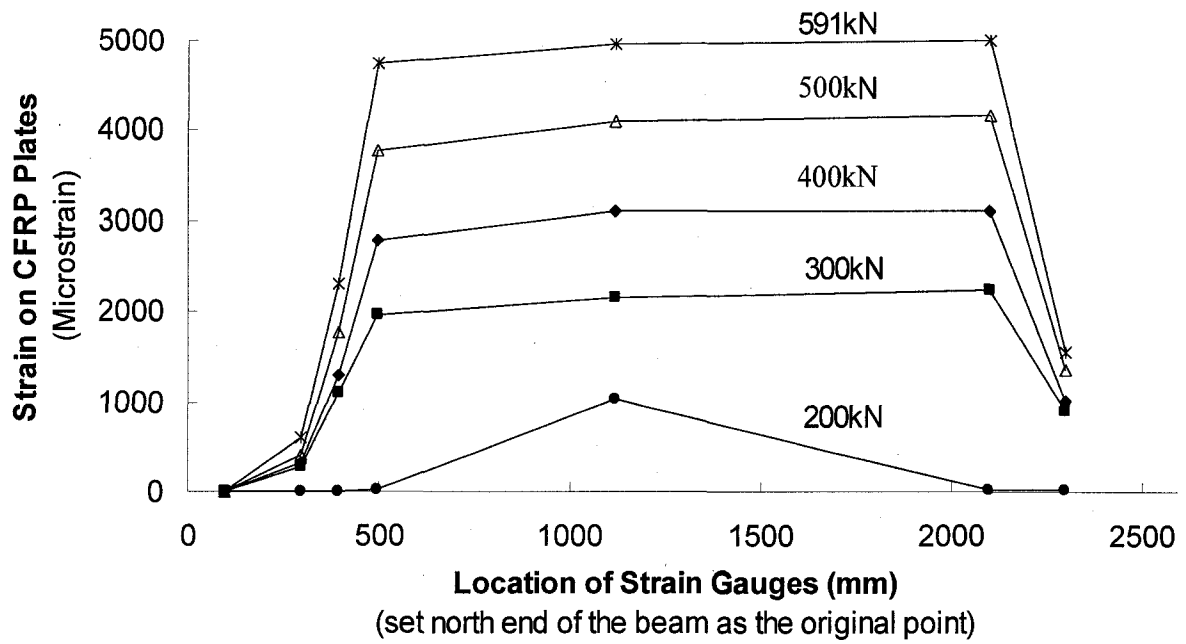


Figure 4-11 Load- Strain on CFRP Plates of Beam 4

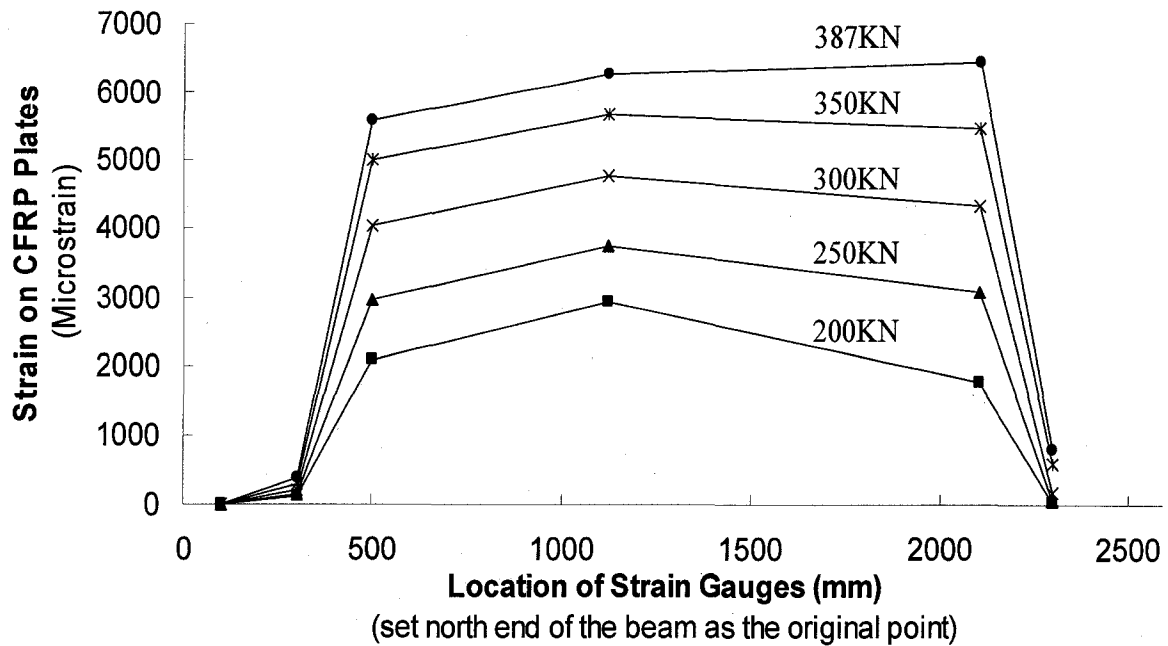


Figure 4-12 Load-Strain on CFRP Plates of Beam 5

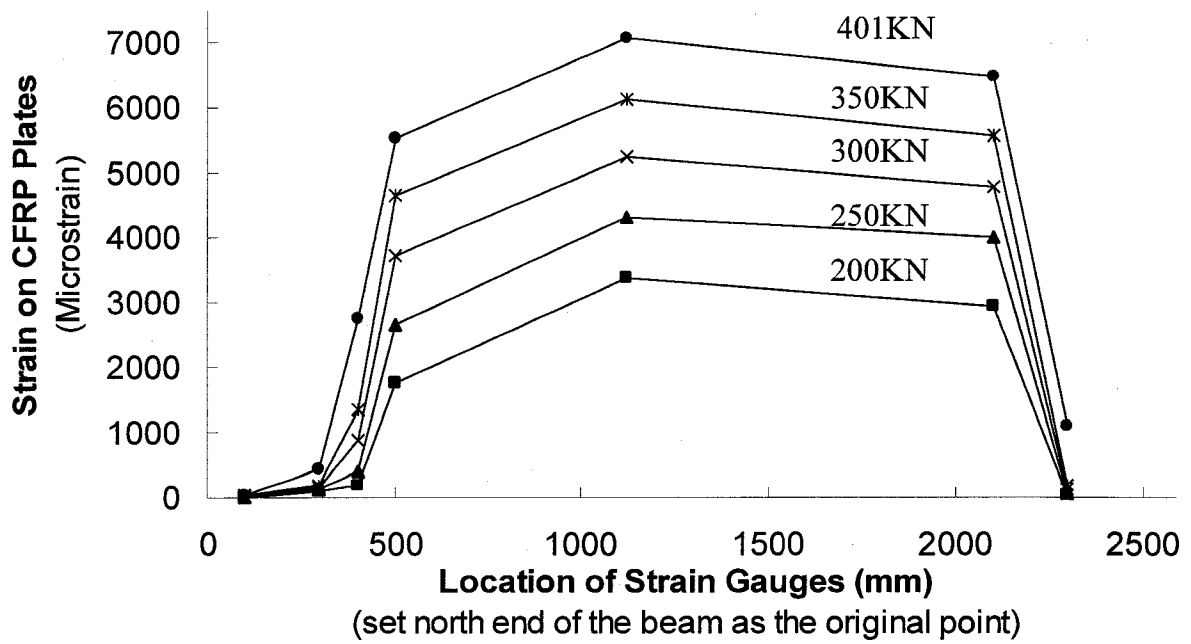


Figure 4-13 Load-Strain on CFRP Plates of Beam 6

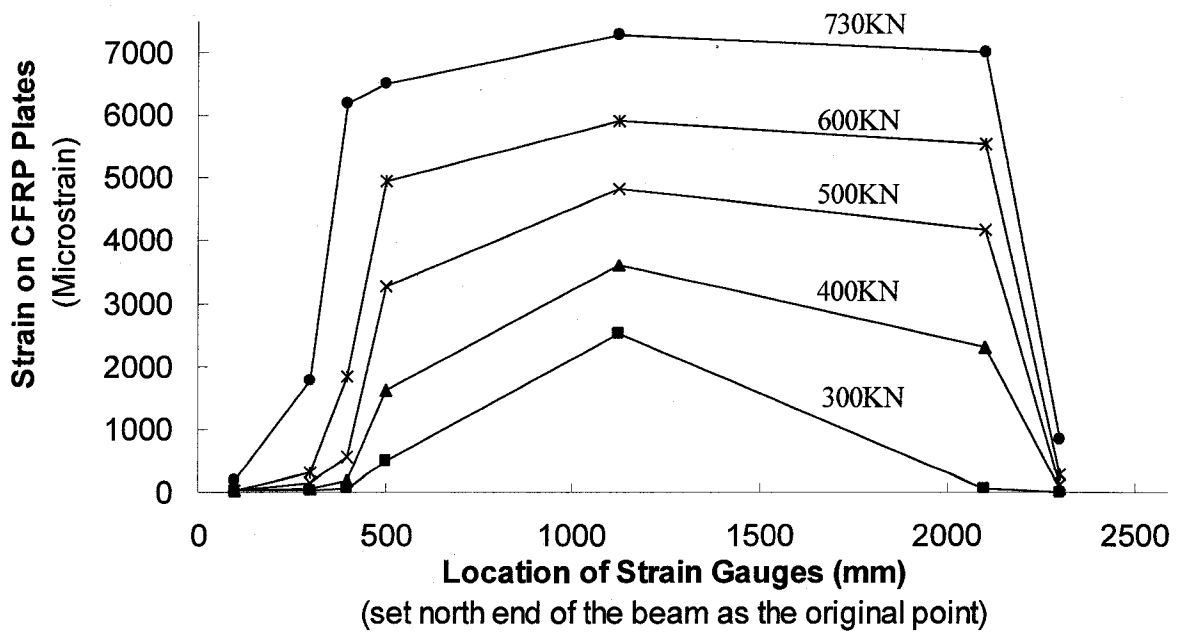
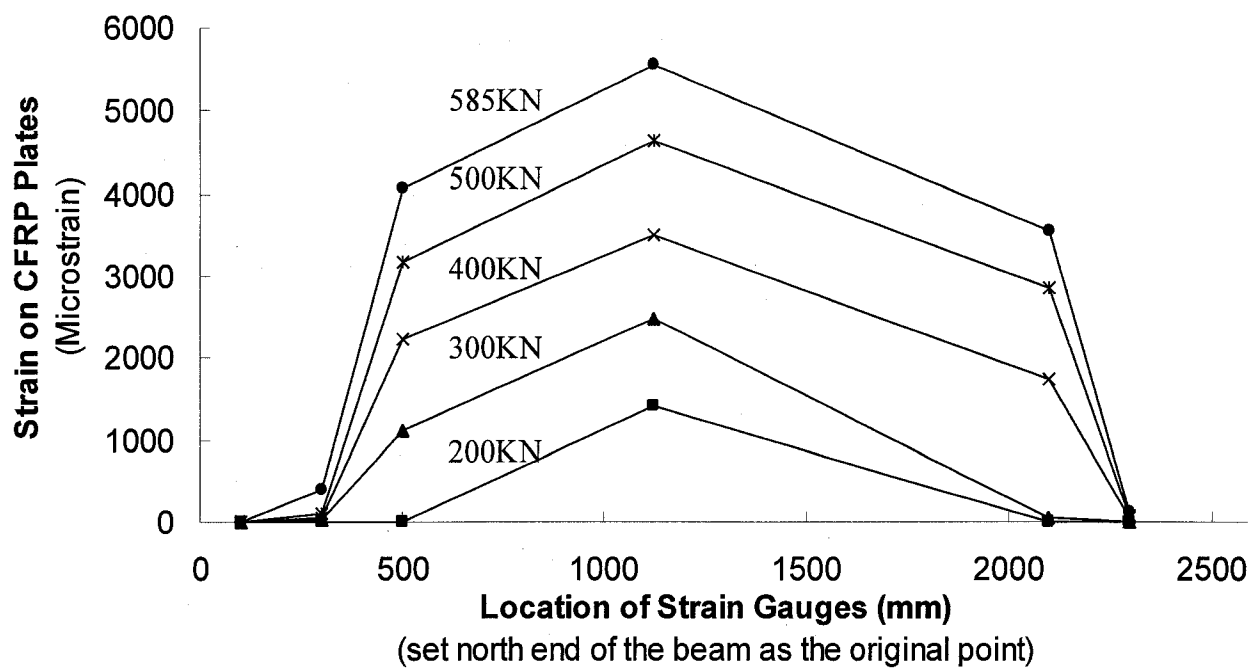
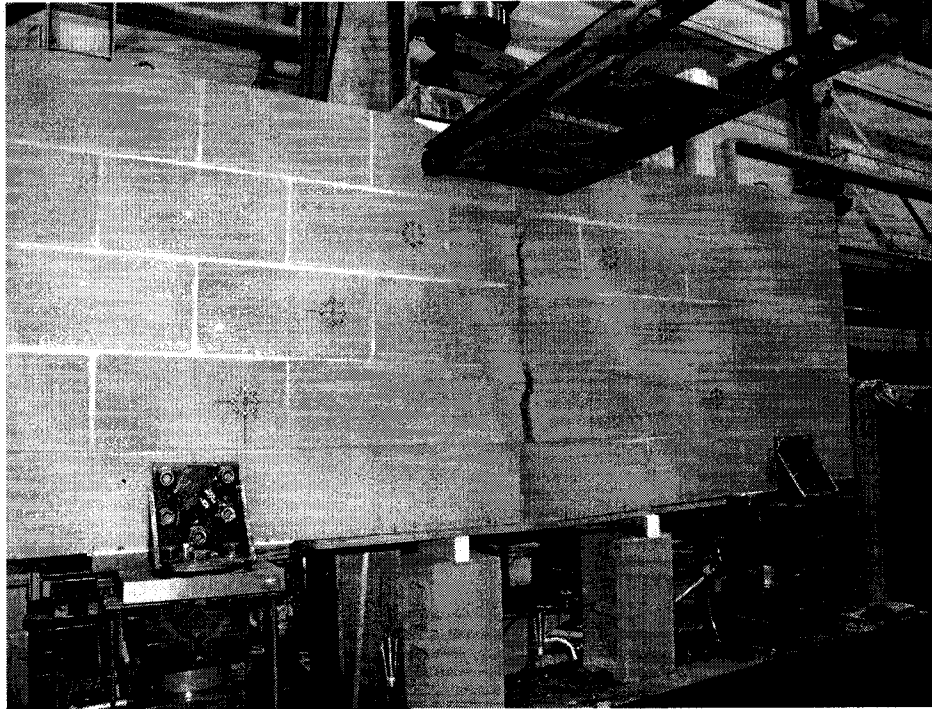


Figure 4-14 Load-Strain on CFRP Plates of Beam 7



**Figure 4-15 Load-Strain on CFRP Plates of Beam 8**



**Image 4-1 Crack Pattern of Beam 1**

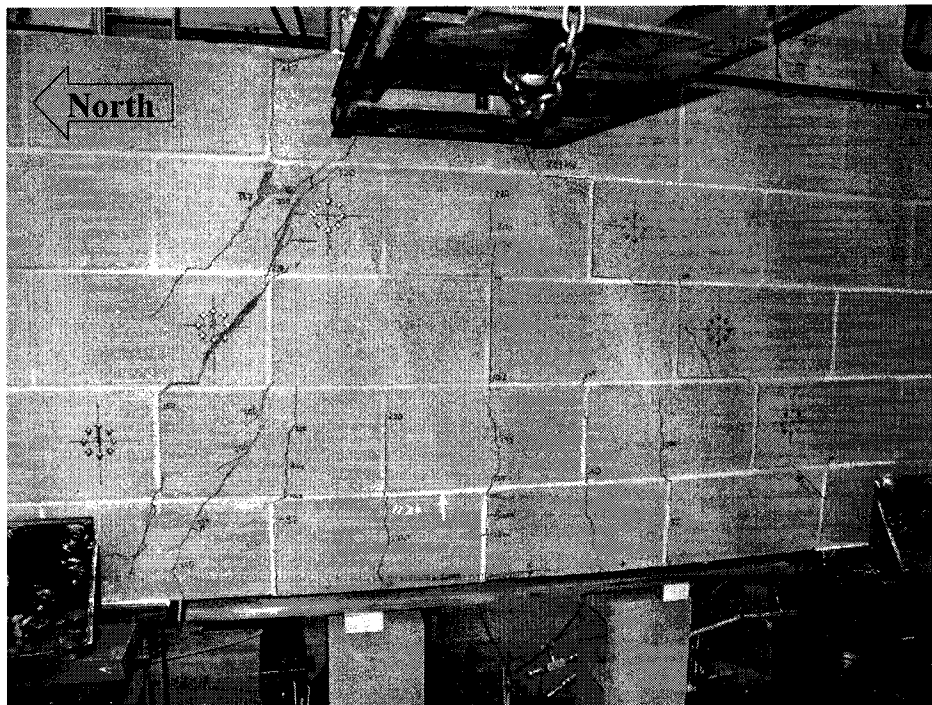


**Image 4-2 Crack Pattern of Beam 2**

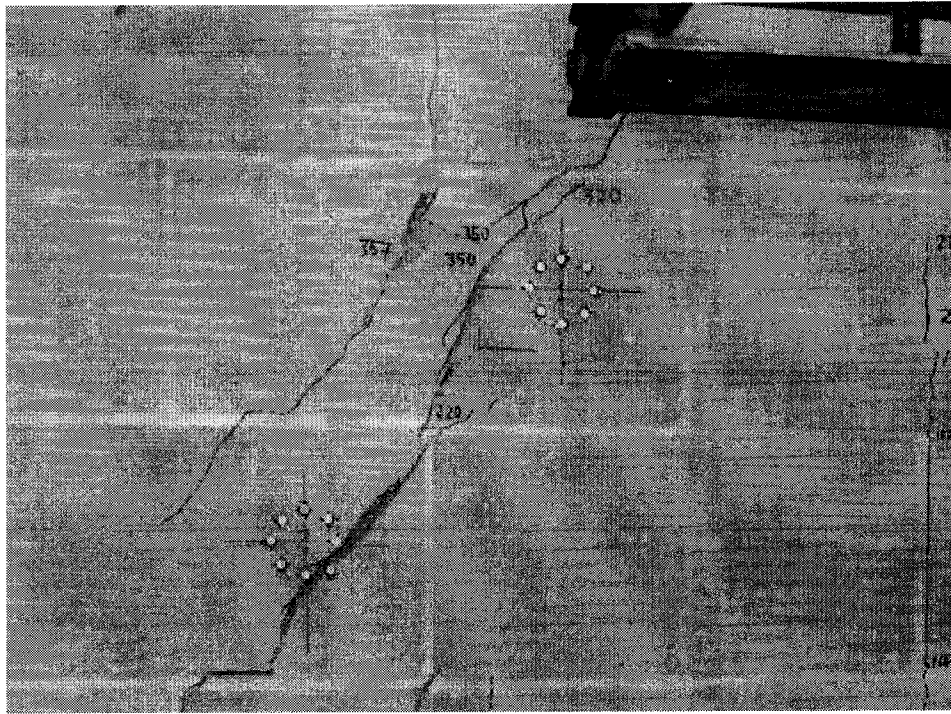


**Image 4-3 Spalling Area of Beam 2**

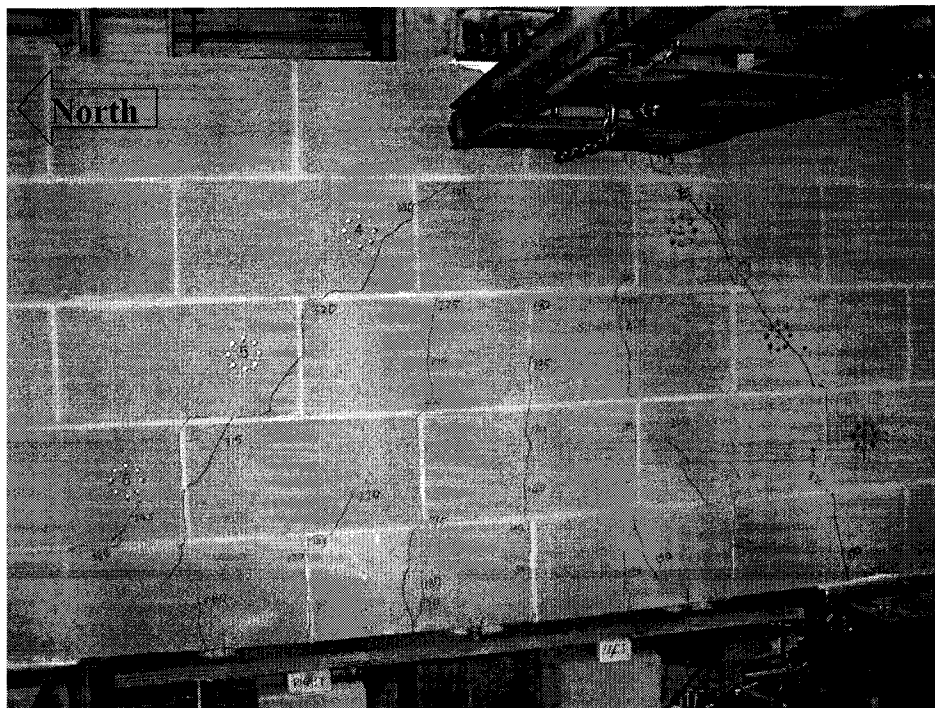


**Image 4-4 Crack Pattern of Beam 3 at the Load of 400 kN**

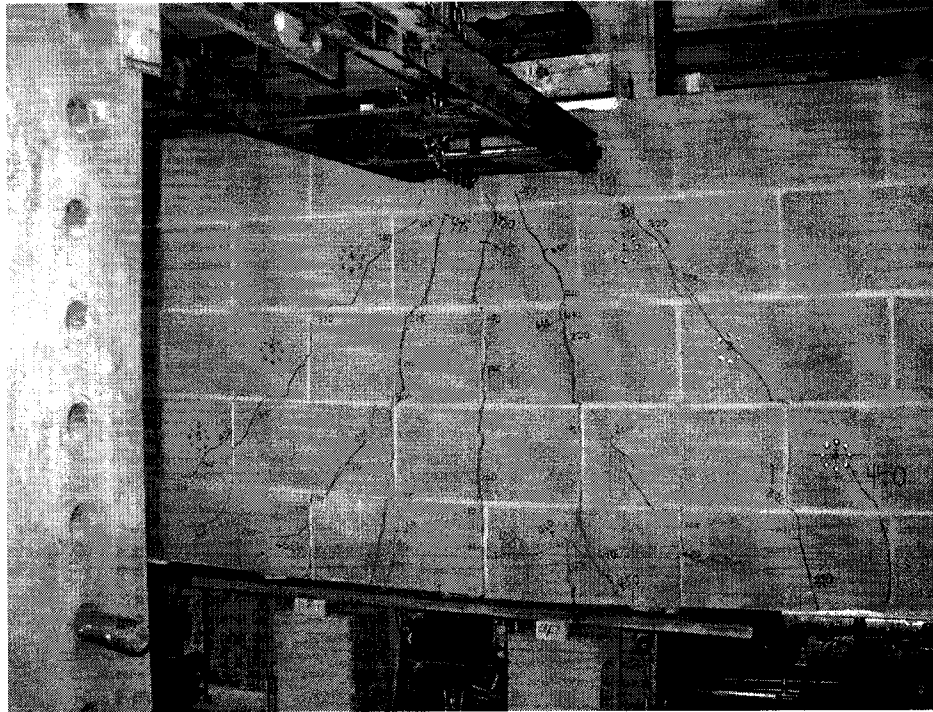


**Image 4-5 Crack Pattern of Beam 3 at the load of 480 kN**

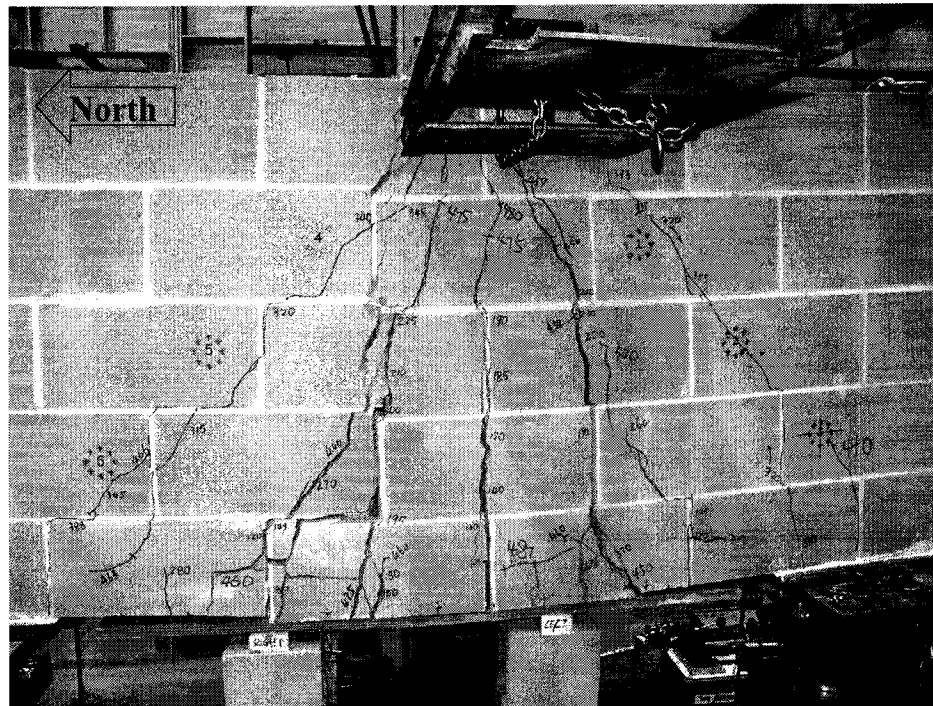


**Image 4-6 Crack Pattern of Beam 3 at Failure**

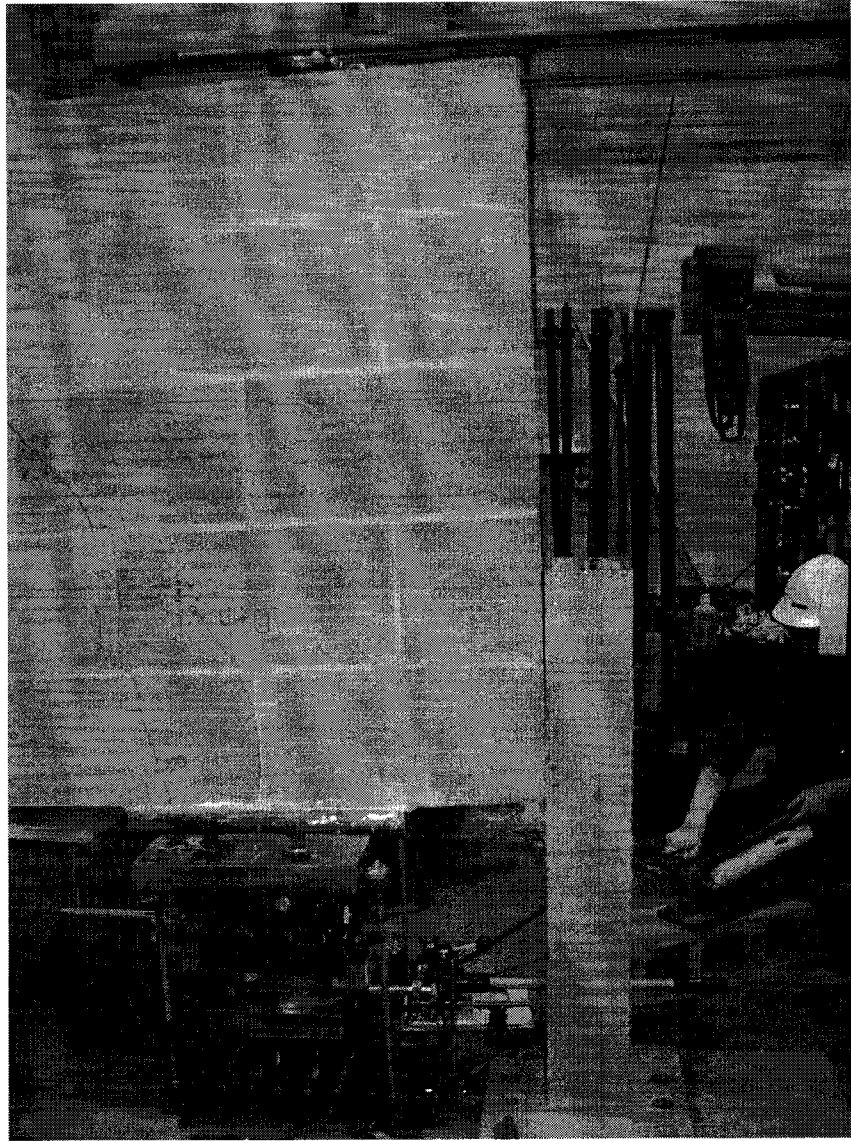


**Image 4-7 Contact Between the End of Beam 3 And South End Restraint**



**Image 4-8 Crushing at the Top Load Point for Beam 3**

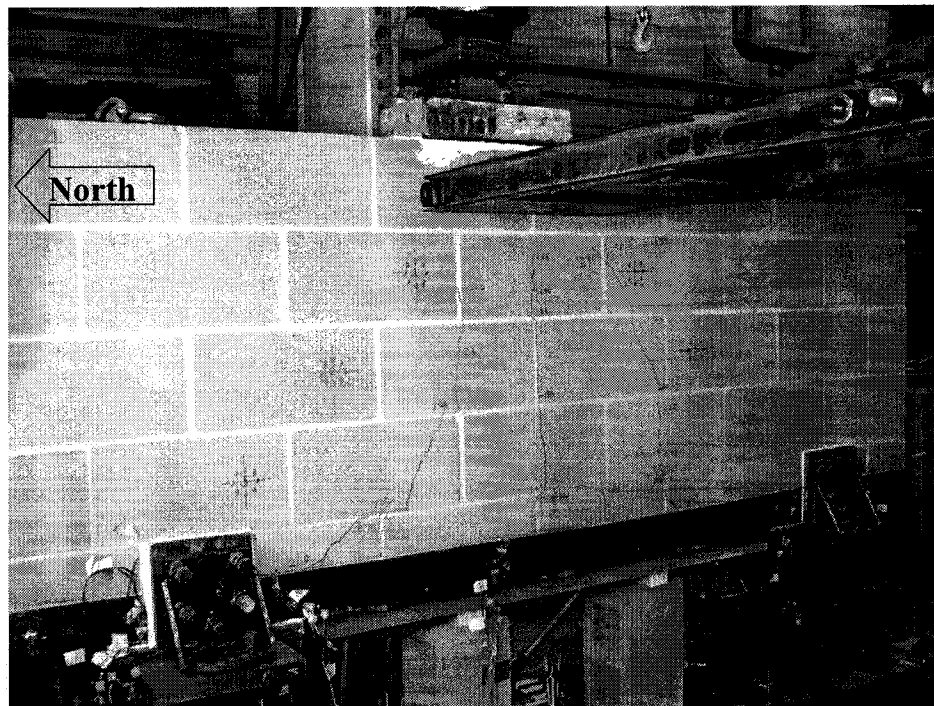


**Image 4-9 Crack Pattern of Beam 4 at the Load of 300 kN**



**Image 4-10 Crack Pattern of Beam 4 at the Load of 500 kN**



**Image 4-11 Crack Pattern of Beam 4 at Failure**

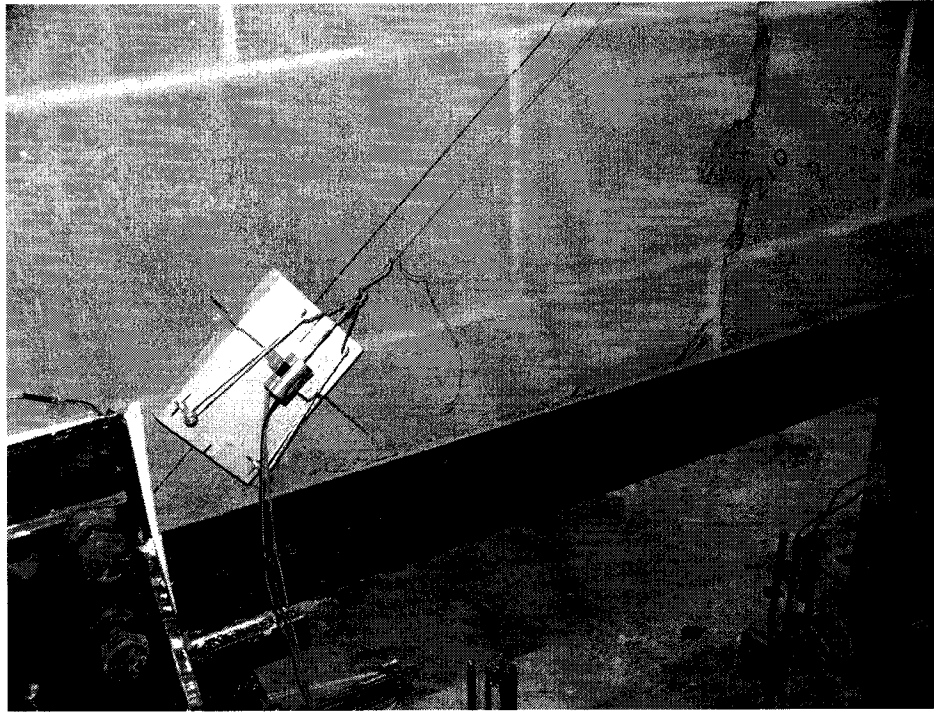


**Image 4-12 Debonding Between CFRP Plate and Masonry Surface of Beam 4**

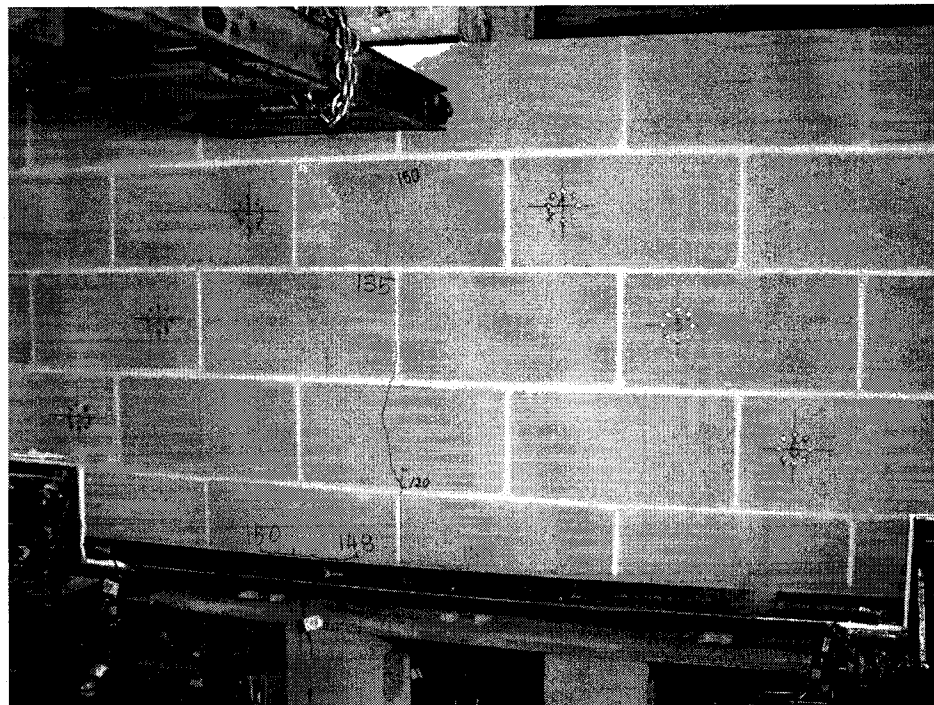


**Image 4-13 Crack Pattern of Beam 5 at the Load of 150 kN**

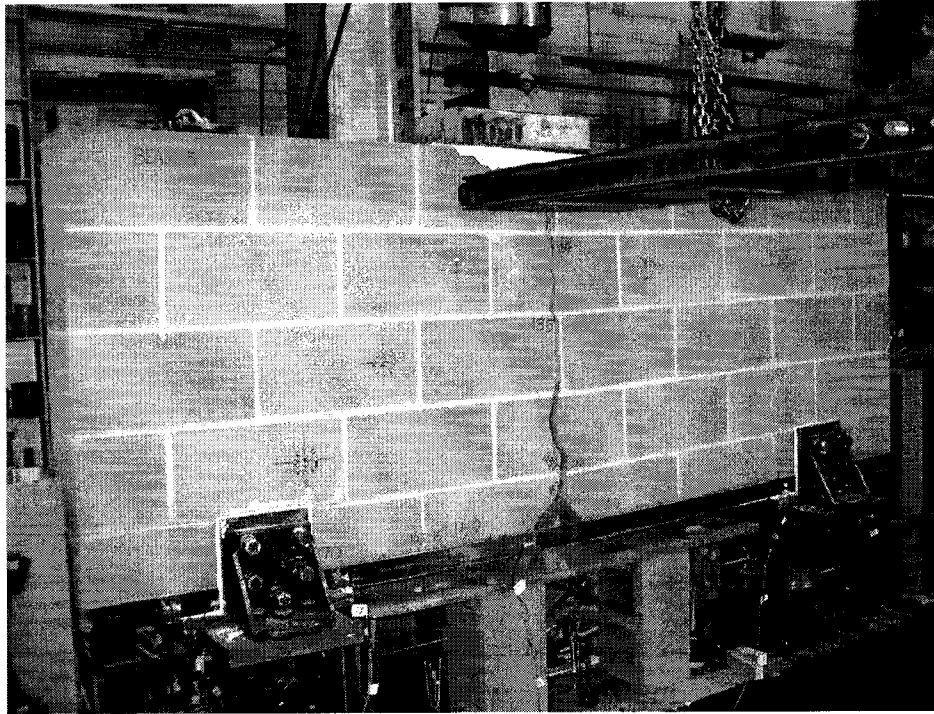


**Image 4-14 Crack Pattern of Beam 5 at Failure**



**Image 4-15 Peeling off at the End of Beam 5**

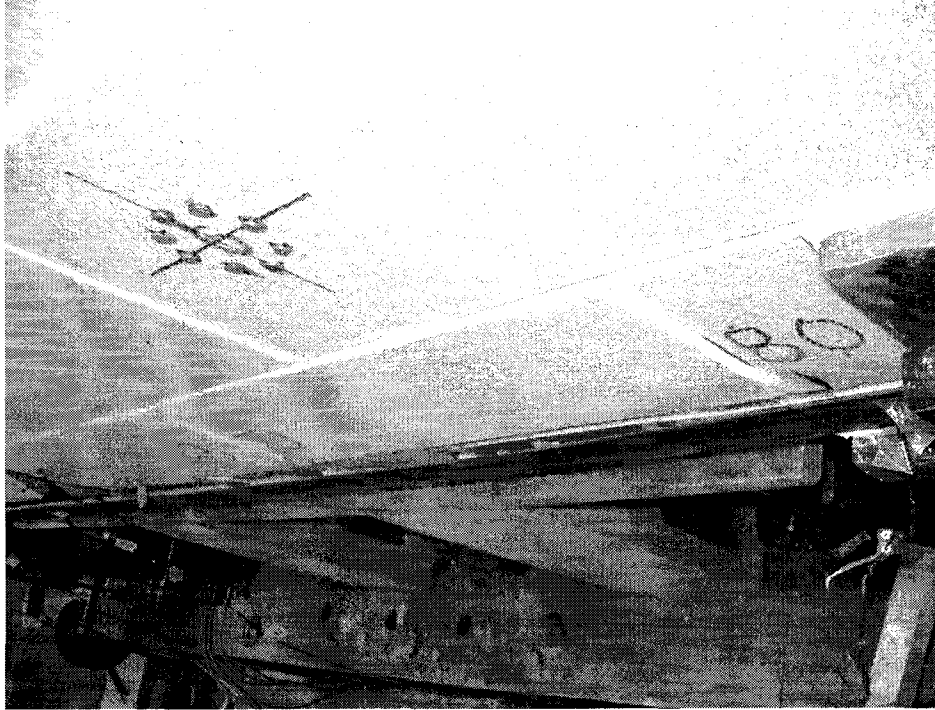


**Image 4-16 Debonding at the Mid-span of Beam 5**

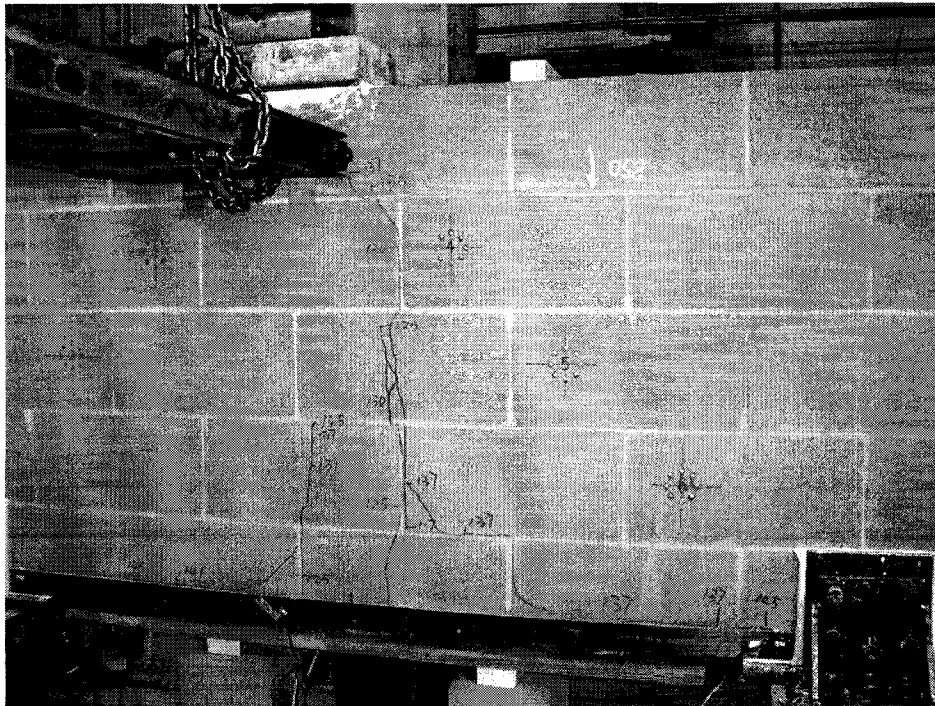


**Image 4-17 Crack Pattern of Beam 6 at the Load of 150 kN**

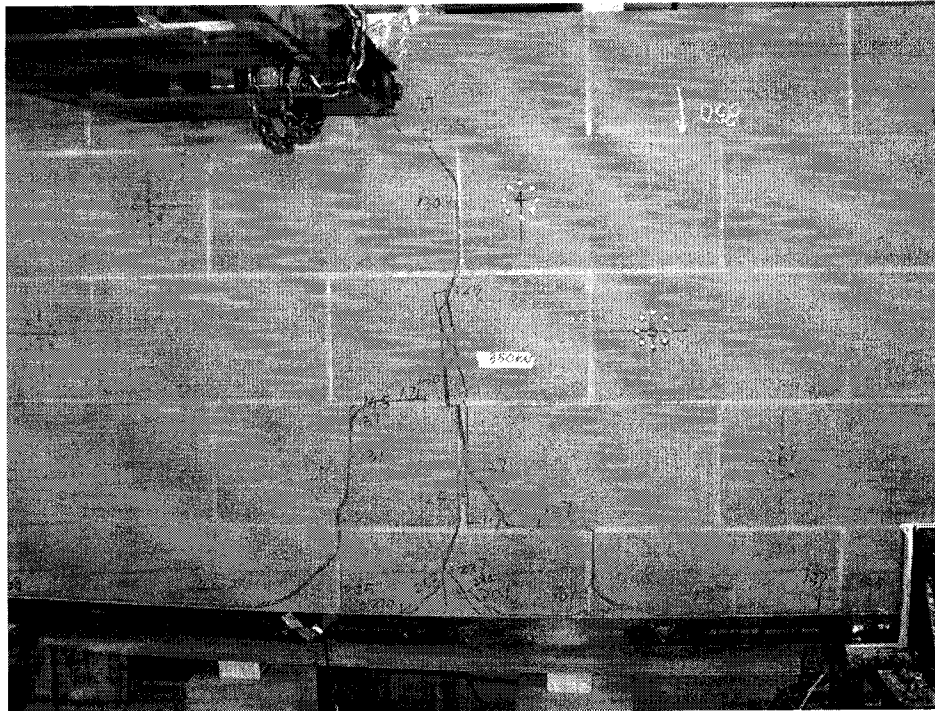


**Image 4-18 Crack Pattern of Beam 6 at the Load of 350 kN**



**Image 4-19 Crack Pattern of Beam 6 at Failure**



**Image 4-20 Peeling off at the End of Beam 6**

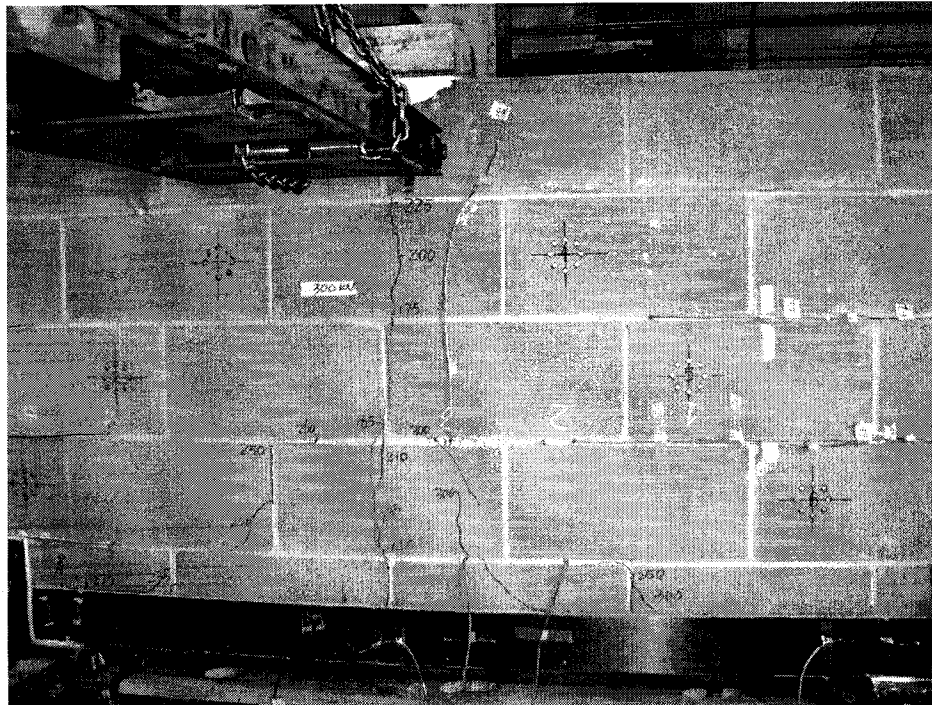


**Image 4-21 Crack Pattern of Beam 7 at the load of 300 kN**

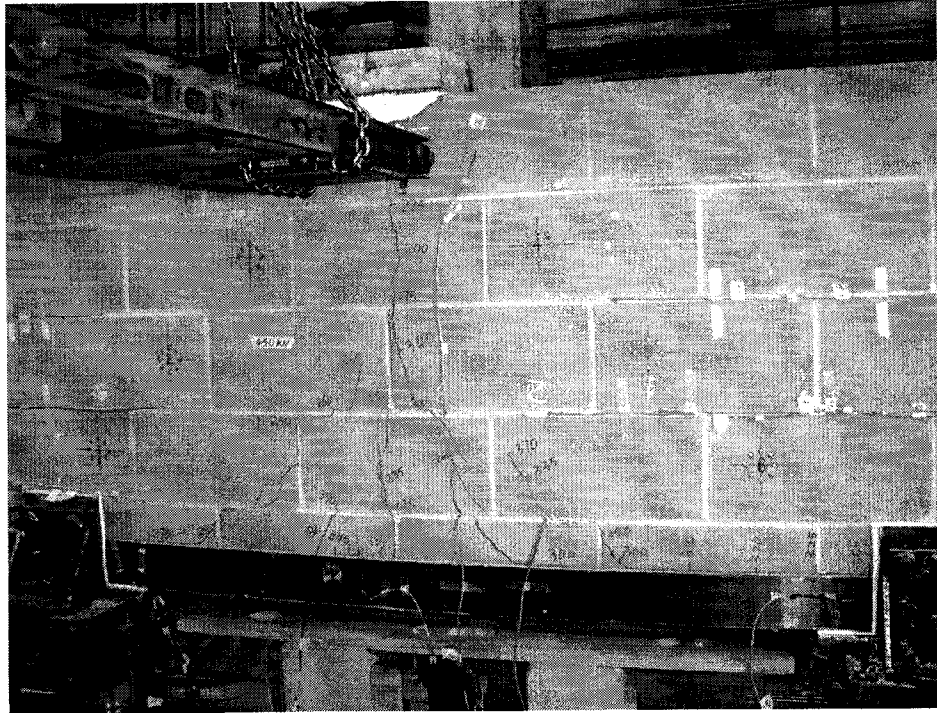


**Image 4-22 Crack Pattern of Beam 7 at the Load of 450 kN**

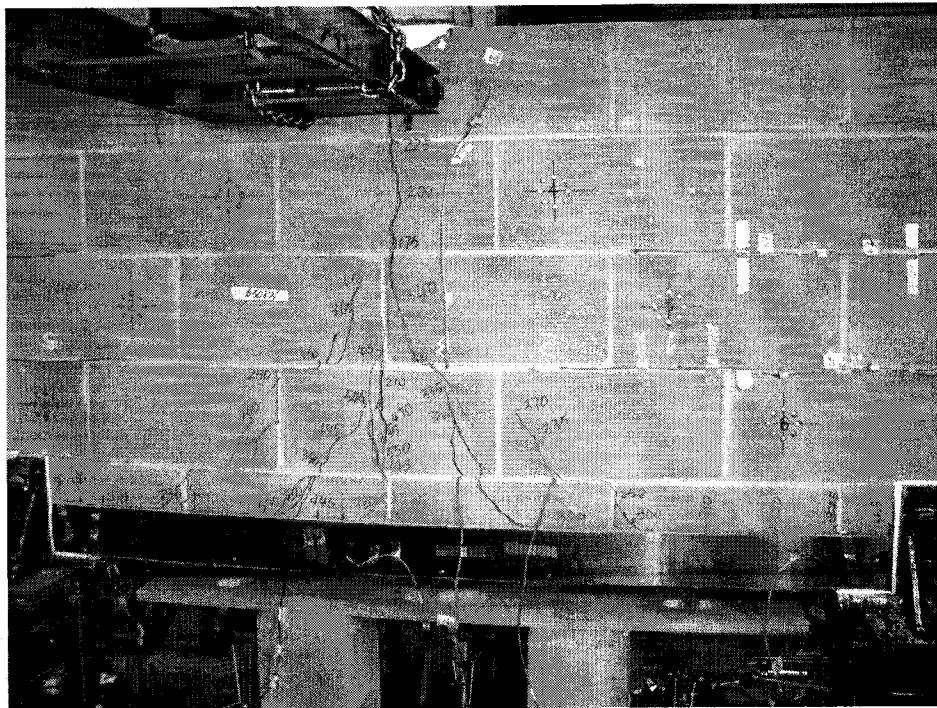


**Image 4-23 Crack Pattern of Beam 7 at the Load of 650 kN**

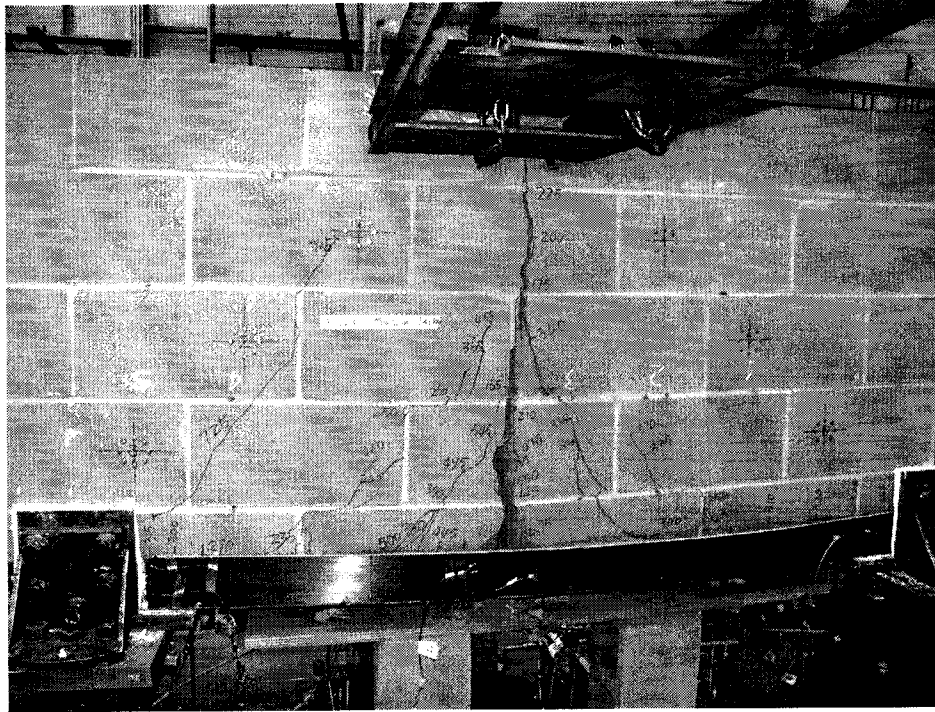


**Image 4-24 Crack Pattern of Beam 7 at Failure**

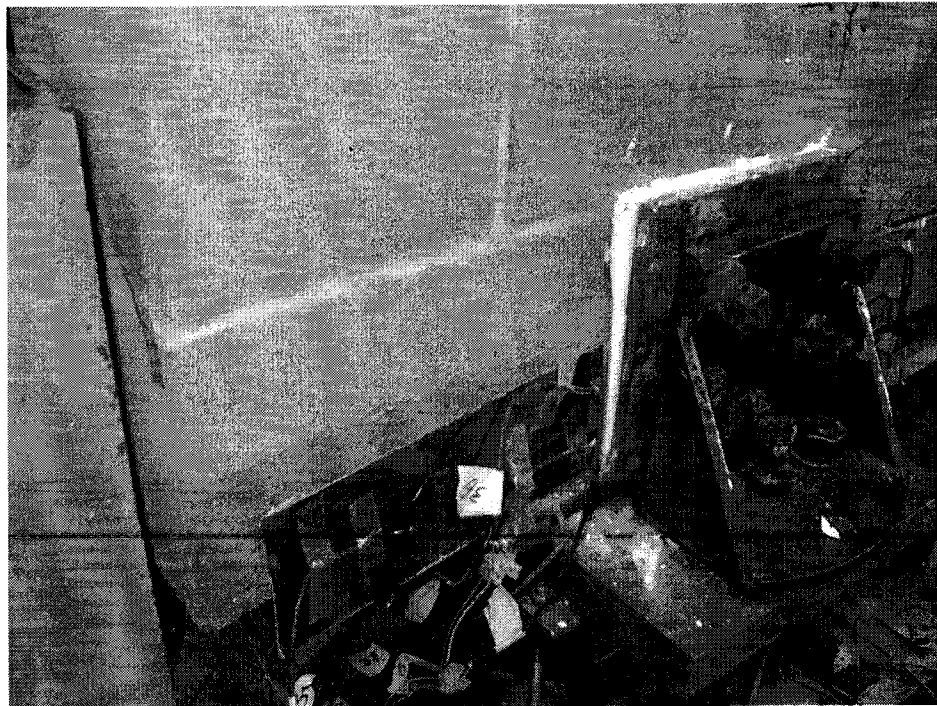


**Image 4-25 Peeling off at the End of Beam 7**

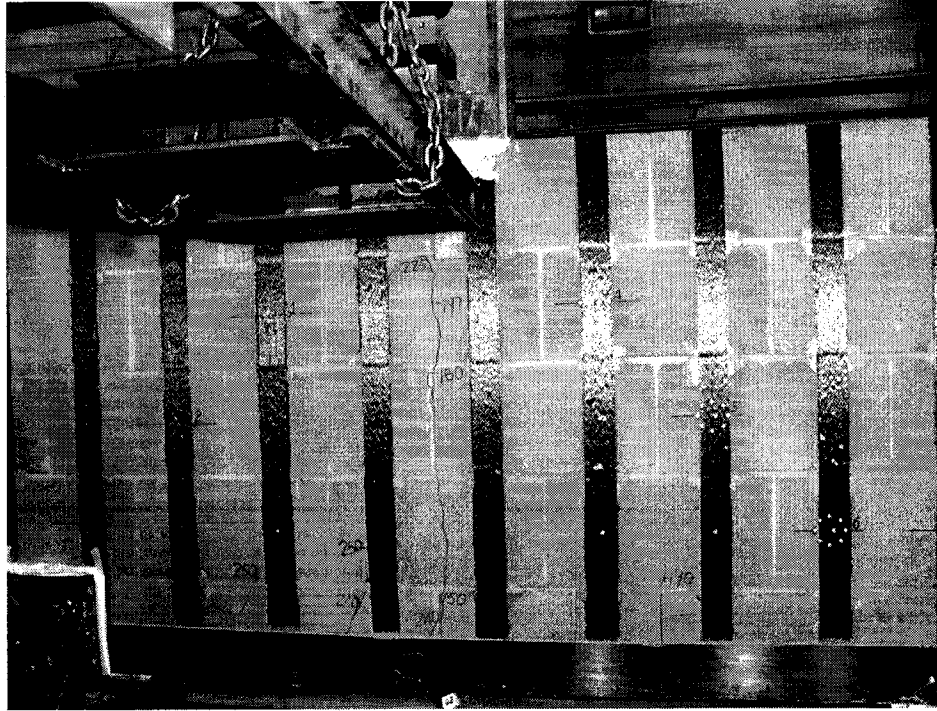


**Image 4-26 Crack Pattern of Beam 8 at the Load of 250 kN**



**Image 4-27 Crack Pattern of Beam 8 at the Load of 300 kN**

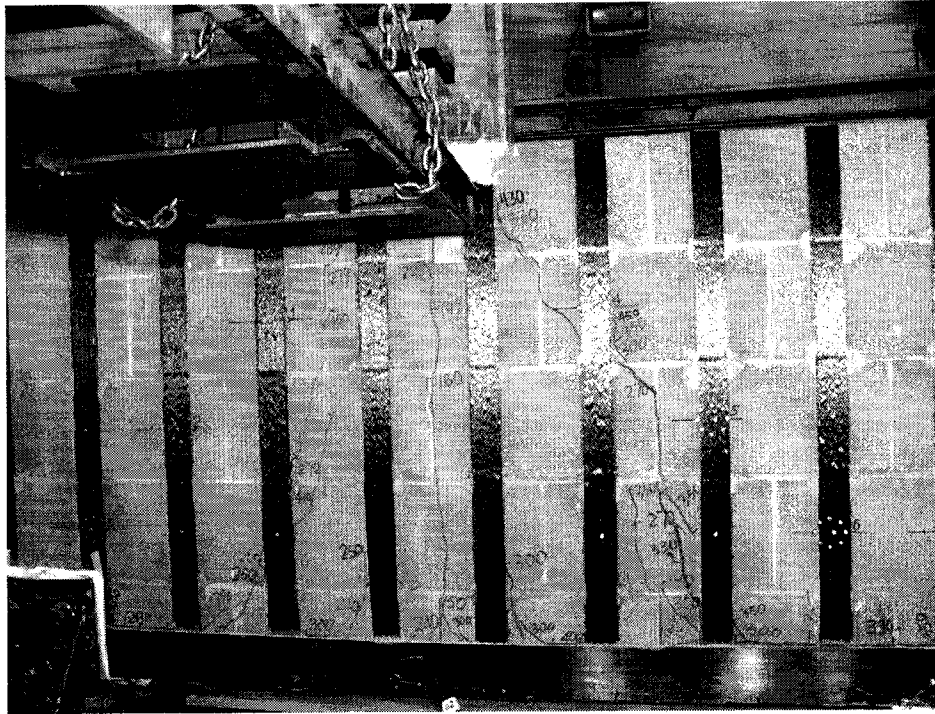


**Image 4-28 Crack Pattern of Beam 8 at the Load of 450 kN**

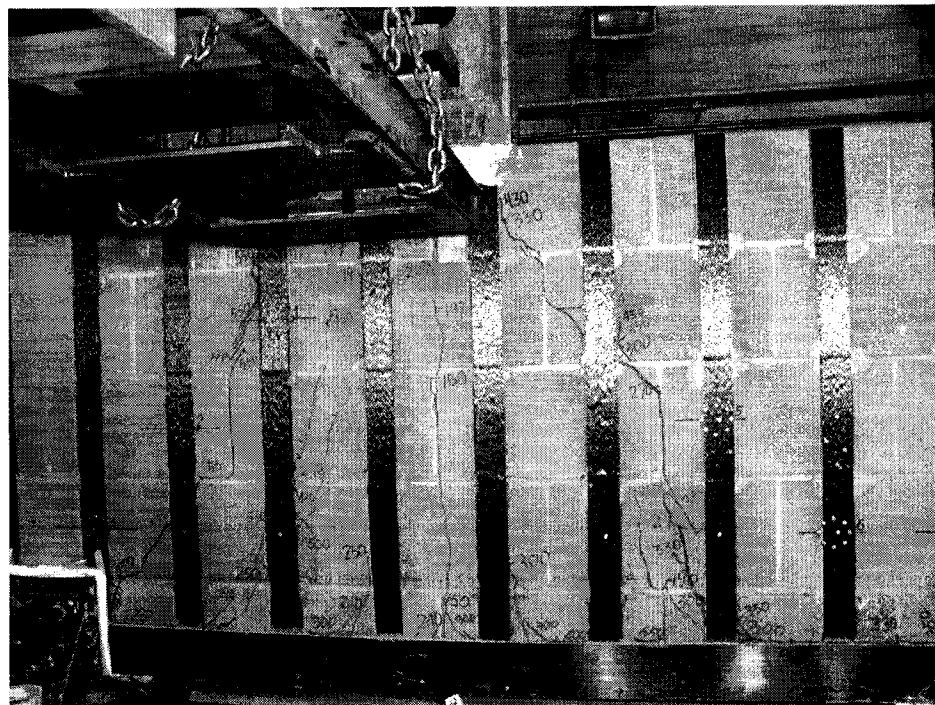


**Image 4-29 Crack Pattern of Beam 8 at the Load of 550 kN**

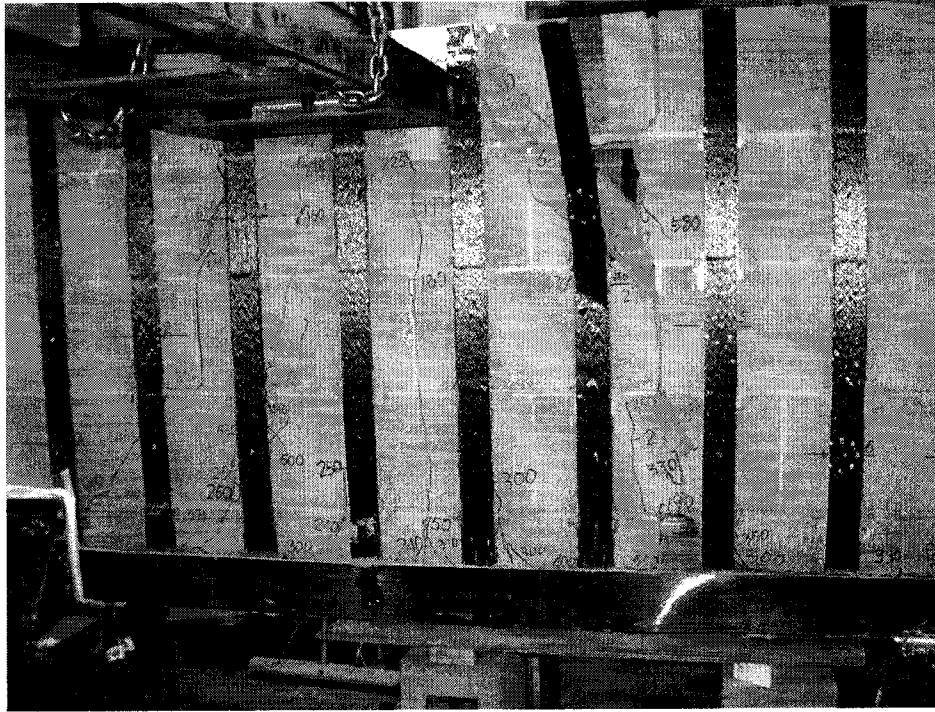


**Image 4-30 Crack Pattern of Beam 8 at Failure**

## 5. ANALYSIS AND DISCUSSION

### 5.1 Introduction

This chapter discusses the comparisons concerning the ultimate strength, ductility and stiffness of specimens strengthened with two different materials, i.e. steel reinforcement and CFRP plates. The effects of variables such as the amount and layout of strengthening materials as well as the arrangement of the anchorage system for CFRP plates are investigated based on the relationship of load-midspan displacement. Several mechanical models were utilized to analyze the behaviour of masonry deep beams and their predictions were compared with the test results. The feasibility of using externally bonded CFRP plates in place of internal steel reinforcement as a retrofit strategy for the masonry lintels is evaluated.

### 5.2 Discussion of Test Results

Test results of all specimens are presented in Chapter 4, and this section discusses test results from three main aspects, i.e. ultimate strength, ductility and rigidity, to estimate the structural characteristics. As described in Chapter 3, all specimens possess the same material and geometric properties and were subjected to identical loading conditions. The comparison of test results can be used to evaluate the behaviour of specimens. In order to have a clearer comparison, the load-midspan displacement curves shown in this section were plotted by removing some small undulations caused by pauses in the readings taken. Table 5-2 presents a comparison of test results for all specimens.

#### 5.2.1 Ultimate Strength

Based on the strengthening strategies for each specimen, a comparison can be carried out for two different parameters: reinforcement material and schemes of strengthening. The details of strengthening strategy and application of anchorage system for each beam were presented in Table 5-1.

##### *Reinforcement Material*

Two types of materials were used to strengthen the specimens: steel reinforcement and carbon fibre reinforced polymer (CFRP). Figure 5-1 and Figure 5-2 illustrate the load

versus mid-span displacement of specimens reinforced with similar reinforcement type but different strengthening materials. It can be noted from these two figures that the ultimate loads of the beams strengthened externally with CFRP plates are higher than those enhanced internally with steel reinforcement. Beams 2, 4, 5, and 6 were strengthened similarly at the bottom of the beams only. In comparison with Beam 2, the load capacities of Beams 4, 5, and 6 were improved by 66%, 8% and 12%, respectively. It is worth mentioning that Beams 5 and 6 failed due to deficient end anchors. Next, as shown in Figure 5-2, Beams 3, 7 and 8 were reinforced both longitudinally and in the web. Evidently, Beams 7 and 8 had a higher ultimate strength than Beam 3. The increments on load capacities are 36% and 9%, respectively. Beam 8 fractured prematurely with debonding of vertical CFRP sheets from the surface of the beam. Moreover, the load capacity of the beam strengthened with CFRP increased when the amount of CFRP plates augmented.

#### ***Arrangement of Reinforcement***

As mentioned in Chapter 3, the specimens investigated in this study were strengthened with two different methods: 1) strengthened at beam bottom and 2) strengthened at both beam web and bottom. It is apparent from Figure 5-3 that the load capacity of Beam 2 was much higher (by 433%) in comparison with Beam 1 due to the adoption of the bottom steel bars, and the ultimate strength of Beam 3 was significantly improved (by 50%) comparing with Beam 2 since the web steel reinforcement was employed as shown in Table 5-2. The same phenomenon can be observed again in Figure 5-4. The load capacity of Beam 7, which was reinforced at beam web and bottom, was higher by 23% in comparison with Beam 4. Nevertheless, the ultimate load of Beam 8 was slightly lower than that of Beam 4 even though Beam 8 was strengthened with web and bottom reinforcement. The explanation for this is that Beam 8 failed early by debonding of web CFRP sheets.

#### **5.2.2 Ductility**

The ductility of the beams was evaluated by means of the mid-span displacement at failure. Based on the test results, it is apparent that the ductility of all beams was influenced by the variation in the amount and type of strengthening materials and

reinforcing methods. Table 5-2 lists the mid-span displacements related to ultimate loads of eight beams. Here, Beam 2 was considered as the reference for the rest of beams instead of Beam 1 as Beam 1 had no reinforcement whatsoever.

### ***Reinforcement Material***

From Figure 5-1, it can be seen that the mid-span displacements at ultimate of Beams 4, 5 and 6, which were strengthened with CFRP plates, are greater than that of Beam 2 by 85%, 85% and 160%, respectively. The reason for the lower ductility in Beam 2 was that this beam failed by crushing of the masonry blocks in the strut region before the longitudinal bars yielded. The curves in Figure 5-2 demonstrate that Beam 3, which was strengthened with steel reinforcement both longitudinally and in the web, had a much higher ductility than Beams 7 and 8 both of which were strengthened with CFRP plates since the steel reinforcement possesses much more plasticity than carbon fibre reinforced polymer.

### ***Arrangement of Reinforcement***

Figure 5-3 and Figure 5-4 show the load-displacement curves of the specimens strengthened with the same material but different strengthening arrangements. It is obvious in Figure 5-3 that Beam 3 reinforced at both web and bottom possesses the greatest system ductility, followed by Beam 2, which was only reinforced flexure. Whereas, Beam 1 had negligible deflection at failure since there was no reinforcement material used. Similarly, in Figure 5-4, due to the presence of web reinforcement, the ductility of Beams 7 and 8 compared with that of Beam 4 was higher by 45% and 25%, respectively. It is apparent that if reinforcement were used at beam web and bottom at the same time, the deep beam could possess more ductility and store more energy.

### **5.2.3 Stiffness**

The stiffness of a beam is defined here as the force that causes a unit displacement at mid-span of the beam. Therefore, the slope of each curve plotted in Figure 5-1 to Figure 5-4 may be used to represent the stiffness of the beam at different loading stages.

### ***Reinforcement Material***

The beams shown in Figure 5-1 were reinforced longitudinally for flexure but with different reinforcement materials. The stiffness of the beams was rather indistinguishable when the load was less than 100 kN. With an increase in the load and the propagation of cracks, the stiffness of all the beams reduced, especially for Beam 5 and Beam 6. Beam 4 had almost the same slope as Beam 2 until the load of 357 kN. In addition, the stiffness of Beam 4 was higher than that of Beams 5 and 6 all the time. This suggests that the stiffness of a beam increases with an increase in the amount of CFRP plates.

It is evident that the slope of the load-displacement curve in Beam 3 was steeper than those of Beam 7 and 8 in Figure 5-2 when the load was under 476 kN. The reason was that the primary flexural cracks at mid-span of Beam 7 and 8 developed upward more rapidly than that of Beam 3. When the load was beyond 476 kN, the stiffness of Beam 3 was considerably reduced since the bottom steel reinforcement yielded. Whereas, Beams 7 and 8 display higher stiffness because of the higher strength of carbon fibre. Moreover, Beam 8 had almost an identical stiffness as Beam 7 until failure occurred. From the crack patterns shown in Chapter 4 (Image 4-21 and Image 4-27), the extensions of primary flexural cracks in both beams were nearly identical and these cracks extended to the bed mortar joint under the top layer of blocks when the load reached 225 kN.

### ***Arrangement of Reinforcement***

In Figure 5-4, all beams were externally strengthened longitudinally with the same amount of CFRP plates. Nevertheless, Beams 7 and 8 were strengthened at beam web also, and no strengthening scheme was used at the web of Beam 4. As it can be seen, the stiffness of Beam 4 is greater than those of Beams 7 and 8 when loads were less than 200KN. The explanation for this is that the diagonal cracks of Beam 4 appeared much earlier than those of Beams 7 and 8, and once the diagonals cracks occurred, the propagation of primary flexural cracks slowed down, which resulted in a slower degradation on the beam stiffness. When loads exceeded 290 kN, these three beams exhibited an basically identical stiffness until failure. From the test results, it seems that the application of vertical web reinforcement did not have any noticeable effect on the stiffness of the specimens.

#### 5.2.4 Other comparisons

It can be noted from Table 5-2 that the appearance of the first crack was postponed in beams strengthened with externally bonded CFRP plates compared to those reinforced with internal steel reinforcement. Further, the more the amount of CFRP plates used, the later the appearance of the first crack; Comparing Beams 3, 7 and 8 with Beams 2 and 4 listed in Table 5-2, the loads related to the appearance of the first diagonal crack were higher since the web reinforcement was also employed in these beams. The load at which debonding occurred for beams strengthened with 50 mm wide CFRP plates was about half that for the beams strengthened with 100 mm wide CFRP plates. The toughness of each beam up to peak load is illustrated in Figure 5-5. Beam 3 possesses the greatest toughness of 7945 N.m while Beam 1 registered only 8 N.m at the failure. Compared with Beam 4, Beam 7 and Beam 8 were able to dissipate more energy at the peak load due to the web reinforcement. It can be seen by comparing Beam 5 with Beam 6 that the earlier the use of the anchorage system, the more energy the beam could accumulate. Furthermore, the ultimate load was increased by only 3.6% even though the torque on each clipping bolt for Beam 6 was twice that of Beam 5.

#### 5.3 Behaviour of Masonry Deep Beams

CSA Standard A23.3-04 Cl.10.7.1 specifies that “Flexural members with clear span to overall depth ratios less than 2 shall be designed as deep flexural members taking into account a nonlinear distribution of strain....” Meanwhile, CSA Standard S304.1-94 Cl.12.3.6.1 designates those members, in which the effective depth exceeds 400 mm and the distance from the inner face of the support to the point of zero shear is less than  $2d$ , shall be considered as deep flexural members. For the investigation here, the clear span of beams, ' $l_n$ ' was 1400 mm, which is less than twice of overall depth of 990 mm. In addition, the shear span, ' $a$ ', was 520 mm and less than twice the effective depth of specimens (890 mm). Thus, the specimens are considered as deep beams, in which a considerable amount of the applied load is transferred directly to the supports by the compression struts between the load and the reactions.

From this study, it appears that the behaviour of reinforced masonry deep beams is

basically identical to that of reinforced concrete deep beams. Referring to the crack patterns exhibited in Chapter 4, except for Beams 5 and 6, which failed prematurely due to insufficient anchorage prior to the formation of diagonal cracks, the crack distribution of the other beams was basically identical to the typical crack pattern of the reinforced concrete deep beam apart from some inclined cracks in masonry deep beams propagating along the vertical and horizontal mortar joints. It is found out that the flexural cracks formed first at the mid-span of beams developed vertically upwards and became progressively wider with increase in the applied loads. At a certain load level, the diagonal cracks initiated in the regions close to supports and these cracks initially extended vertically, and then propagated towards the load point in diagonal direction. Furthermore, once the diagonal cracks appeared, these cracks grew more rapidly than the flexural cracks at mid-span. Thereafter, failure occurred along with the primary diagonal cracks fully developing throughout the compression struts. Similar to reinforced concrete deep beams, these masonry beams failed in shear-compression or crushing in the compression zone along with flexural failure.

## **5.4 Mechanical Model**

### **5.4.1 Introduction**

It is clear from the literature reviewed in Chapter 2 that there is no effective design method to evaluate the shear capacity of masonry deep beams yet. CSA Standard S304.1-94 Cl.12.3.6 only prescribes special provisions for deep shear spans from two aspects: 1) the area of transverse shear reinforcement shall not be less than  $0.002b_w s$  and  $s$  shall not exceed  $d/5$  nor 300 mm; 2) longitudinal reinforcing bars shall be distributed over the depth of the beam and the cross-section area of each layer bars shall be not less than  $0.002b_w s$ . There is no clear guideline for the design of deep shear masonry components. On the other hand, the predictions for the shear strength of reinforced concrete deep beams have been studied for many years. Based on the premise of that both reinforced masonry and concrete deep beams behave similarly under 3-point loading, the mechanical models used to predict the reinforced concrete deep beams may be suitable for the analyses of masonry deep beams. This section provides four mechanical models to analyze the deep beam behaviour and to predict the load capacity of the masonry deep

beams. The comparison between the predictions and test results is presented in this section as well.

#### 5.4.2 Load Capacity Prediction for Masonry Deep Beams

Four mechanical models were selected, namely, CSA S304.1-94, CSA A23.3-04, “Interactive Mechanical Model” provided by Tang *et al.* and a shear strength model for reinforced concrete deep beams proposed by Russo *et al.* The prediction for the load capacity of each specimen was made using these selected models. For the purpose of comparison, the safety factors in these mechanical models have been set to unity.

##### **MODEL No.1 ---CSA S304.1-94 Masonry Design for Buildings**

CSA S304.1-94 Cl.12.3.5 recommends that the shear resistance of shear members shall be determined from

$$V_r = V_m + V_s \quad (5.1)$$

where  $V_r$  = shear resistance

$V_m$  = shear resistance of masonry members provide by the masonry

$V_s$  = shear resistance provided by shear reinforcement

For continuously grouted hollow block masonry,  $V_m$  shall be calculated as follows:

$$V_m = 0.2\lambda\sqrt{f_m'}\left(1.0 - \frac{(d - 400)}{1500}\right)b_w d \quad (5.2)$$

Where  $\phi_m$  = resistance factor for masonry, here set  $\phi_m = 1$  for the purpose of investigation

$\lambda$  = factor to account for low density concrete masonry units

$f_m'$  = compressive strength of masonry, MPa

$b_w$  = web width of beam, mm

$d$  = distance from extreme compression fiber to centroid of tension reinforcement, mm

But  $V_m$  must not be greater than  $0.2\lambda\sqrt{f_m'}b_w d$ , or less than  $0.12\lambda\sqrt{f_m'}b_w d$ . If the masonry beam is not continuously grouted, equation 5.2 shall be multiplied by 0.6 to determine  $V_m$ .

Shear resistance provided by shear reinforcement  $V_s$  shall be calculated as

$$V_s = A_v f_y \frac{d}{s} \quad (5.3)$$

but not greater than  $0.36\lambda\sqrt{f'_m} b_w d$ .

in which,  $A_v$  = cross-section area of web reinforcement,  $\text{mm}^2$

$f_y$  = yield strength of steel reinforcement, MPa

$s$  = spacing of shear reinforcement measured parallel to the longitudinal axis of the member, mm

From the equations above, it can be seen that arch-action in deep beam is not taken into account for carrying the loads. The predictions of beams by using this model are presented in second column of Table 5-3. The predictions of load capacity for Beam 2, 4, 5 and 6 are same since these beams were strengthened without web reinforcement, and the load carrying capacity only based on the shear resistance of masonry members. Comparing with experiment results, it is apparent that the CSA S304.1 predictions are overconservative in this case.

#### **MODEL No.2---Strut-and -Tie model Recommended by CSA A23.3-04**

CSA A23.3-04 Cl.11.4 gives a method to investigate the reinforced concrete members by idealizing the reinforced concrete as a series of steel tensile ties and concrete compressive struts interconnected at node zones. The compressive strength of strut shall be calculated as the product of  $A_{cs}$ , the effective cross-section area of concrete strut, and  $f_{cu}$ , the compressive stress of strut. The value of  $A_{cs}$  shall be determined in accordance with Cl.11.5.2.2 and the value of  $f_{cu}$  shall be calculated as follows:

$$f_{cu} = \frac{f'_c}{0.8 + 170\varepsilon_1} \leq 0.85f'_c \quad (5.4)$$

in which

$$\varepsilon_1 = \varepsilon_s + (\varepsilon_s + 0.002) \cot^2 \theta_s \quad (5.5)$$

where  $\theta_s$  is the smallest angle between the compressive strut and the adjoining tensile ties and  $\varepsilon_s$  is the tensile strain in the tension tie. The tensile strength in the tension tie shall not

be larger than  $\Phi_c A_{st} f_y$ . Meanwhile, the stress in node regions shall be limited according to the Clause 11.4.4 in CSA A23.3-04. The Strut-and-Tie model described above is for concrete deep beams. In order to predict the capacities of masonry deep beams, the concrete compressive stress  $f_c$  in these equations is replaced by masonry compressive strength,  $f_m$ .

Table 5-3 shows the predictions of beam load capacities by using this model. In comparison with Model No.1, the predictions based on CSA A23.3-04 give better estimates of load capacities of these masonry deep beams.  $P_{test}/P_{model-2}$  values for Beam 3 and Beam 7 indicated that the predictions by Strut-and-Tie model considerably underestimated the load capacities of masonry deep beams strengthened with web reinforcement. The explanation for this is that the beneficial effect of web reinforcement on the compressive strength of diagonal strut is not taken into account in this method, whereas, in fact, the use of web reinforcement enhanced the strength of the web, and resulted in the specimens failing not by crushing in the compressive struts, but by flexure. On the other hand, the predictions for Beams 5 and 6 were higher than the test results since the bottom tension ties failed due to pull-out of the CFRP plates from the anchorage system before any crushing could commence in the compressive struts. In general, this method explains rationally the transfer of forces by assuming a Strut-and-Tie mechanical scheme in the deep beam even though this approach underestimates the load capacities of masonry deep beams strengthened with web reinforcement.

### **MODEL No.3---Interactive Mechanical Model Provided By Tang and Tan**

This method is named as the “Interactive Mechanical Model”, which is based on the strut-and-tie approach and is intended to properly account for the effect of transverse tensile stresses on the compressive strength of the diagonal strut. This model involves an interaction between the two failure modes, namely, splitting of diagonal strut due to tensile stress perpendicular to the diagonal strut and diagonal crushing of the strut due to compressive stresses in the diagonal direction. To simplify the calculation, an important assumption was made: the distribution of forces carried by the concrete section  $T_{ct}$ , the web reinforcement  $T_w$ , and the main reinforcement  $T_s$  are determined by the relative magnitudes of their respective capacities.

$$\frac{T_{ct}}{f_{ct}A_{ct}} = \frac{T_w}{f_{yw}A_w} = \frac{T_s}{f_y A_s}$$

The resistance of inclined strut to diagonal splitting  $V_{ds}$  is expressed as follows:

$$V_{ds} = f_{ct}A_{ct} \frac{1}{2 \cos \theta_s} + f_{yw}A_w \left( \frac{d_w - 0.5l_c}{z_s} \right) \frac{\sin(\theta_w + \theta_s)}{\cos \theta_s} + f_y A_s \tan \theta_s \quad (5.6)$$

where,

$f_{ct} = 0.5\sqrt{f_c}$  (SI) concrete tensile stress

$f_{yw}$  = yield strength of web reinforcement, MPa

$f_y$  = yield strength of longitudinal steel reinforcement, MPa

$A_w$  = area of web reinforcement, mm<sup>2</sup>

$A_s$  = area of longitudinal tension bars, mm<sup>2</sup>

$A_{ct}$  = area of concrete section along diagonal strut, mm<sup>2</sup>,  $A_{ct} = b_w z_s / \sin \theta_s$

$d_w$  = distance from beam top to intersection of web reinforcement with line connecting support center and load center, mm

$l_c$  = height of top node, mm

$z_s$  = lever arm of  $T_s$  to the center of the concrete stress block at the top load point, mm

$\theta_s$  = angle between longitudinal tension reinforcement and diagonal strut, degree

$\theta_w$  = angle between web reinforcement and horizontal axis of beams at intersection of reinforcement and diagonal strut, degree

If web reinforcement is provided uniformly throughout the beam depth,  $V_{ds}$  can be expressed as:

$$V_{ds} = f_{ct}A_{ct} \frac{1}{2 \cos \theta_s} + f_{yw}A_w \frac{\sin(\theta_w + \theta_s)}{2 \cos \theta_s} + f_y A_s \tan \theta_s \quad (5.7)$$

The strut capacity against diagonal crushing of concrete  $V_{dc}$  is denoted as:

$$V_{dc} = f_c' A_{str} \sin \theta_s \quad (5.8)$$

where

$A_{str}$  = cross-sectional area of the diagonal strut, mm<sup>2</sup>,  $A_{str} = b_w (l_a \cos \theta_s + l_b \sin \theta_s)$

$f_c'$  = concrete cylinder strength, MPa

Therefore, the predicted nominal shear strength  $V_n$  can be expressed as follows:

$$V_n = \frac{1}{\frac{1}{V_{ds}} + \frac{1}{V_{dc}}} \quad (5.9)$$

All equations presented are based on the premise that premature failure does not happen. Similarly, since this mechanical model was deduced derived for concrete, some adjustments related to the material properties shall be made. The compressive stress of masonry prisms,  $f_m'$ , is used to replace concrete compressive stress,  $f_c'$ , and the concrete tensile stress  $f_{ct}$  is replaced by the flexural tensile strength of masonry,  $f_t$ .

The computed strengths according to this mechanical model are listed in Table 5-3. This approach is based on the Strut-and-Tie model and accounts for the effect of the transverse stresses upon the load capacity of deep beams in the diagonal strut. From equation 5.7, the resistance of inclined strut to diagonal splitting  $V_{ds}$  includes contributions not only from web and tension reinforcement, but also from concrete tensile strength. Comparing the predictions of load capacities to measured test results indicates that this interactive mechanical model gives good predictions for deep masonry beams strengthened only with longitudinal reinforcement (externally or internally), as it can be seen that the values of  $P_{test}/P_{model-3}$  are 1.05 and 1.05 for Beams 2 and 4, respectively. In addition, these predictions stay on the conservative side. However, for Beams 3 and 7, which were reinforced both in the web and longitudinally, the values of  $P_{test}/P_{model-3}$  are 1.42 and 1.25, respectively. For these two beams, the predictions by this model were quite conservative. The experimental results for Beams 5 and 6 are slightly lower than the predicted values due to the insufficiency of the anchorage system at both ends.

#### **MODEL No.4---Mechanical Model Proposed by Russo *et al.***

This approach for deep reinforced concrete (RC) beams is also based on the strut-and-tie model and this design expression, equation (5.10), fits the test results of RC deep beams very well. The cross-sectional shear resistance of deep beams comprises two portions, namely, shear strength contribution provided by concrete and shear contribution given by web reinforcement. The design formula of shear strength for the deep RC beams can be expressed as:

$$v_{n,d} = 0.545(k\chi f'_c \cos \theta + 0.25\rho_h f_{yh} \cot \theta + 0.35 \frac{a}{d} \rho_v f_{yv}) \quad (5.10)$$

where

$\theta$  = angle between inclined strut and vertical direction, degree

$a$  = shear span length, mm

$d$  = effective depth of deep beam, mm

$k$  is derived from the classical bending theory for a single reinforced section

$$k = \sqrt{(n\rho_f)^2 + 2n\rho_f} - n\rho_f \quad (5.11)$$

with  $n$  the ratio of steel to concrete elastic moduli ( $= E_s/E_c$ ) and  $\rho_f$  the longitudinal reinforcement ratio ( $= A_s/bd$ ).

$\rho_h, \rho_v$  = horizontal and vertical web reinforcement ratios, respectively

$f_{yh}, f_{yv}$  = yielding strength of horizontal and vertical web reinforcements, MPa,

respectively and  $\chi$  is the nondimensional interpolating function expressed as

$$\chi = \left[ 0.74 \left( \frac{f'_c}{105} \right)^3 - 1.28 \left( \frac{f'_c}{105} \right)^2 + 0.22 \left( \frac{f'_c}{105} \right) + 0.87 \right] \quad (5.12)$$

This mechanical model takes into account the shear strength contributions provided by the Strut-and-Tie mechanism due to the diagonal concrete strut and the longitudinal main reinforcement, as well as the vertical stirrups and horizontal web reinforcement, as seen in equation (5.10). In order to utilize this model to predict the shear strength of masonry

deep beams, some modifications were made. First of all, the compressive strength of masonry,  $f_m'$ , takes the place of the compressive strength of concrete,  $f_c'$ . Secondly, the modulus of concrete,  $E_c$ , was replaced by the modulus of elasticity for masonry,  $E_m$ , which was calculated from equation 5.13:

$$E_m = 850 f_m' \quad (5.13)$$

Table 5-3 also lists the predicted results in accordance with this mechanical model. Compared with the experimental results, this analytical approach overestimated the shear strengths of masonry deep beams except for Beam 3. The reason probably is that this approach is derived on the basis of the material being concrete. Compared with the continuity of concrete, masonry is a composite structure comprising of masonry units, mortar joints and grout. When masonry members carry shear forces, mortar joints present rather low shear resistance so as to impair the shear capacity of the member.

## 5.5 Conclusion

Four mechanical models were examined in this section to predict the load capacities of seven masonry deep beams (not including Beam 1) strengthened with diverse strategies. The comparison between predictions based on different analytical models and the experimental results indicates that: Model-1 (CSA S304.1-94) is over conservative in predicting the shear strengths of deep masonry members; Model-2 (CSA A23.3-04) is better than Model-1, but still underestimates the shear capacities of deep masonry beams in some cases; Model-4 (Russo *et al.* 2005) somewhat overestimates the shear strengths of deep masonry beams; On the other hand, Model-3 provided by Tang *et al.* (2004) gives the best fit between the computed results and test data. However, the conclusion that the behaviour of deep masonry beams having either internal steel reinforcement or external CFRP material could be evaluated using this interactive mechanical model cannot be drawn because of the following reasons. This research is based on only eight deep masonry beams and some of these beams failed due to loss of the bond between CFRP plates and masonry surface due to the insufficiency of the anchorage system, such as in Beam 5, 6 and 8. Therefore, the test results in this study were not conclusive for this

kind of deep masonry members. Nevertheless, this research does provide a valuable datum for future study.

**Table 5-1 Reinforcing Method and Anchorage Application for Specimens**

<b>Beam Number</b>	<b>Method Reinforced</b>	<b>Anchorage Description</b>	<b>Torque on Each Clamping Bolt (FootPound)</b>
<b>Beam 1</b>	Without any reinforcement	_____	_____
<b>Beam 2</b>	Reinforced with 2 No.15 rebars longitudinally	_____	_____
<b>Beam 3</b>	Reinforced with 2 No.15 rebar longitudinally and 11 No.10 rebars in the web	_____	_____
<b>Beam 4</b>	Strengthened with 2-100mm CFRP plates longitudinally	Anchorage system used after debonding happened	50
<b>Beam 5</b>	Strengthened with 2-50mm CFRP plates longitudinally	Anchorage system used after debonding happened	50
<b>Beam 6</b>	Strengthened with 2-50mm CFRP plates longitudinally	Anchorage system used from the beginning of the test	100
<b>Beam 7</b>	Strengthened with 2-100mm CFRP plates longitudinally and reinforced with 11 No.10 rebars in the web	Anchorage system used from the beginning of the test	100
<b>Beam 8</b>	Strengthened with 2-100mm CFRP plates longitudinally and 22 pieces of 50mm wide CFRP fabric strips at spacing of 200mm in the web	Anchorage system used from the beginning of the test	100

**Table 5-2 Comparison of Test Results**

Specimen Number	Load at First Crack (kN)	Corresponding Deflection (mm)	Load at Debonding (kN)	Ultimate Load (kN)	Load Increase at Ultimate* (%)	Corresponding Deflection (mm)	Deflection Increase at Ultimate* (%)
Beam 1	60	0.2	—	67	—	0.22	—
Beam 2	84	0.24	—	357	—	3.3	—
Beam 3	85	0.2	—	536	50	17.3	424
Beam 4	136	0.35	202	592	66	6.1	85
Beam 5	120	0.53	148	387	8	6.1	85
Beam 6	117	33	137	401	12	8.6	161
Beam 7	145	1.27	270	730	104	8.7	164
Beam 8	150	1.18	280	585	64	7.5	127

\* Beam 2 is considered as the reference beam to make the comparison.

**Table 5-3 Predictions for Load Capacity of Specimens**

Beam Number	Predictions of Load Capacity				Test Results	Comparison with Test Results			
	$P_{model-1}$ (kN)	$P_{model-2}$ (kN)	$P_{model-3}$ (kN)	$P_{model-4}$ (kN)		$P_{test}$ (kN)	$P_{test}/P_{model-1}$	$P_{test}/P_{model-2}$	$P_{test}/P_{model-3}$
<b>Beam 2</b>	136	323	339	403	357	2.63	1.11	1.05	0.89
<b>Beam 3</b>	432	323	378	461	536	1.24	1.66	1.42	1.16
<b>Beam 4</b>	136	496	564	708	592	4.35	1.19	1.05	0.84
<b>Beam 5</b>	136	494	432	544	387	2.85	0.78	0.90	0.71
<b>Beam 6</b>	136	494	432	544	401	2.95	0.81	0.93	0.74
<b>Beam 7</b>	432	496	582	754	730	1.69	1.47	1.25	0.97
<b>Beam 8</b>	491	496	565	711	585	1.19	1.18	1.04	0.82

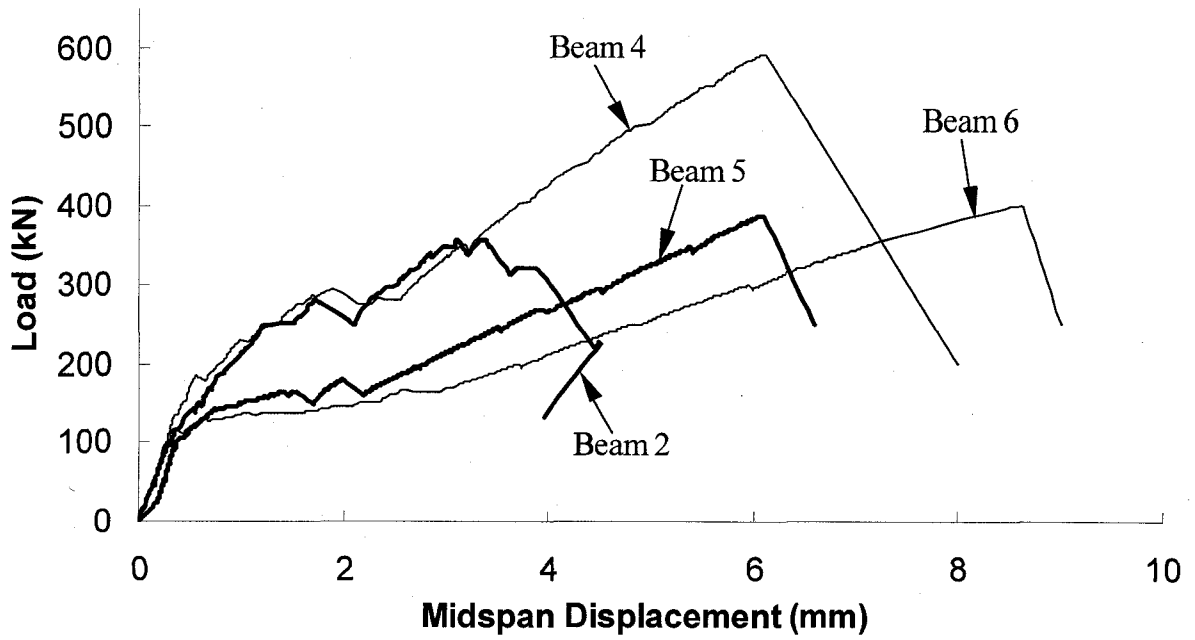


Figure 5-1 Load-Midspan Displacement Curves for Beam 2, 4, 5 and 6

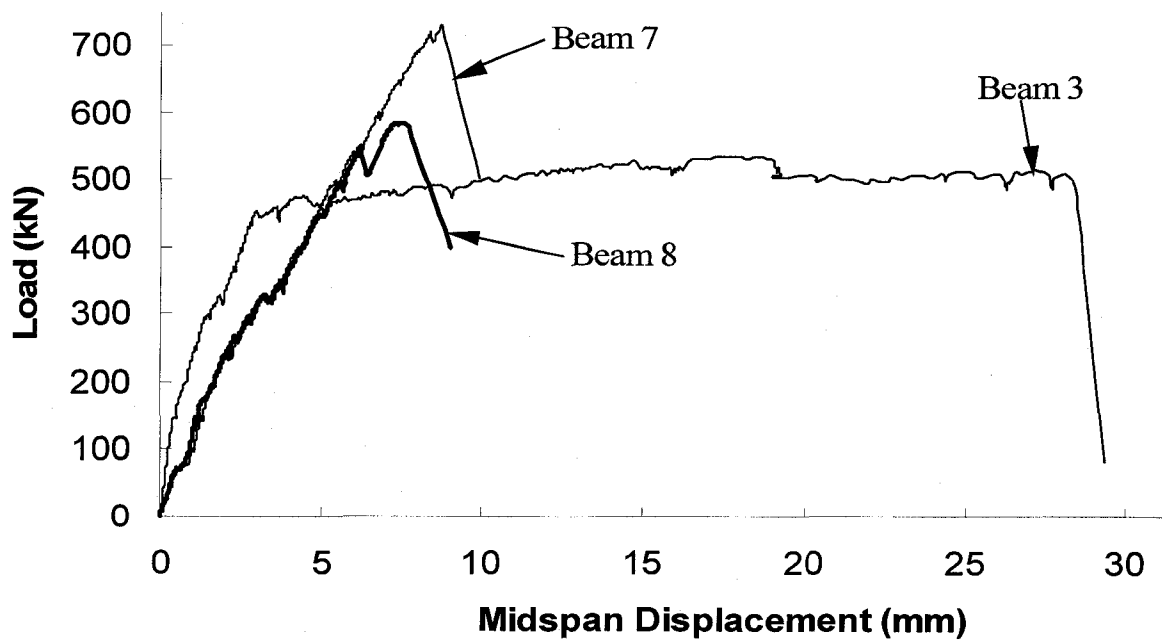
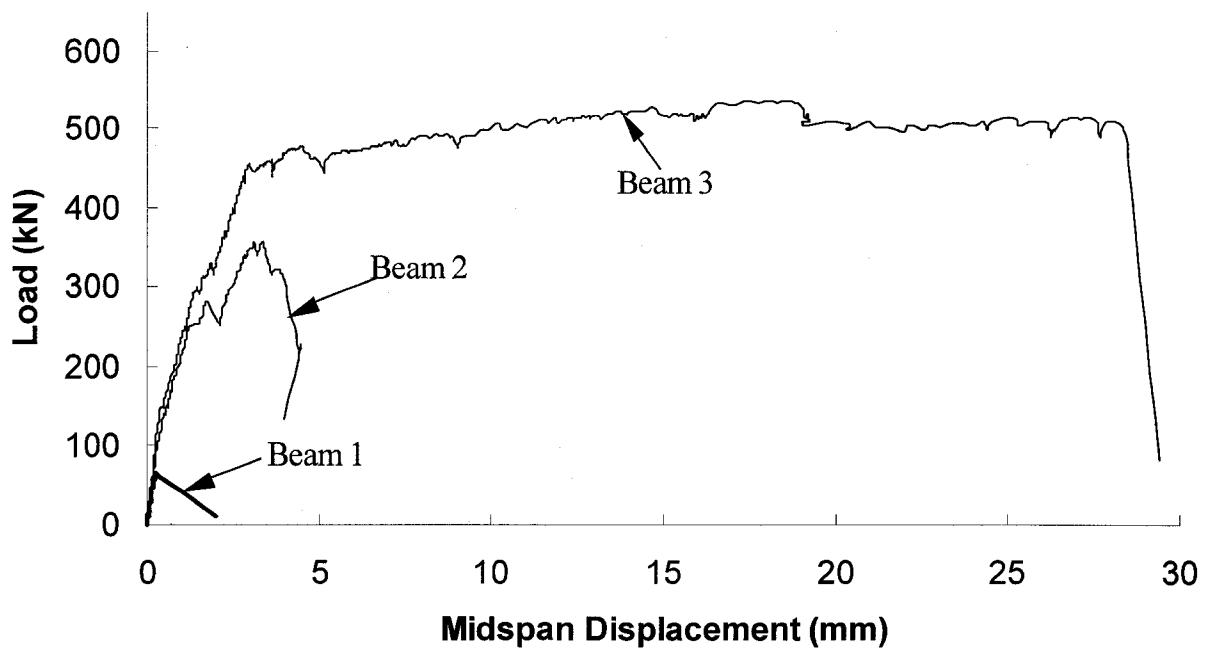
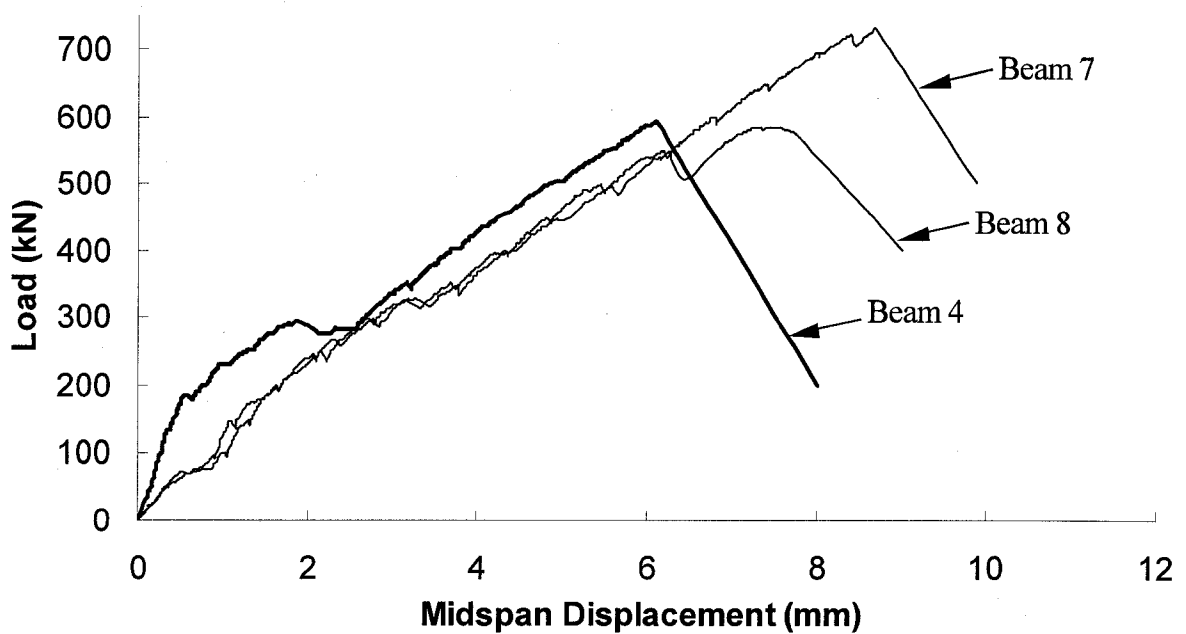


Figure 5-2 Load-Midspan Displacement For Beam 3, 7 and 8



**Figure 5-3 Load-Midspan Displacement for Beam 1, 2 and 3**



**Figure 5-4 Load-Midspan Displacement for Beam 4, 7 and 8**

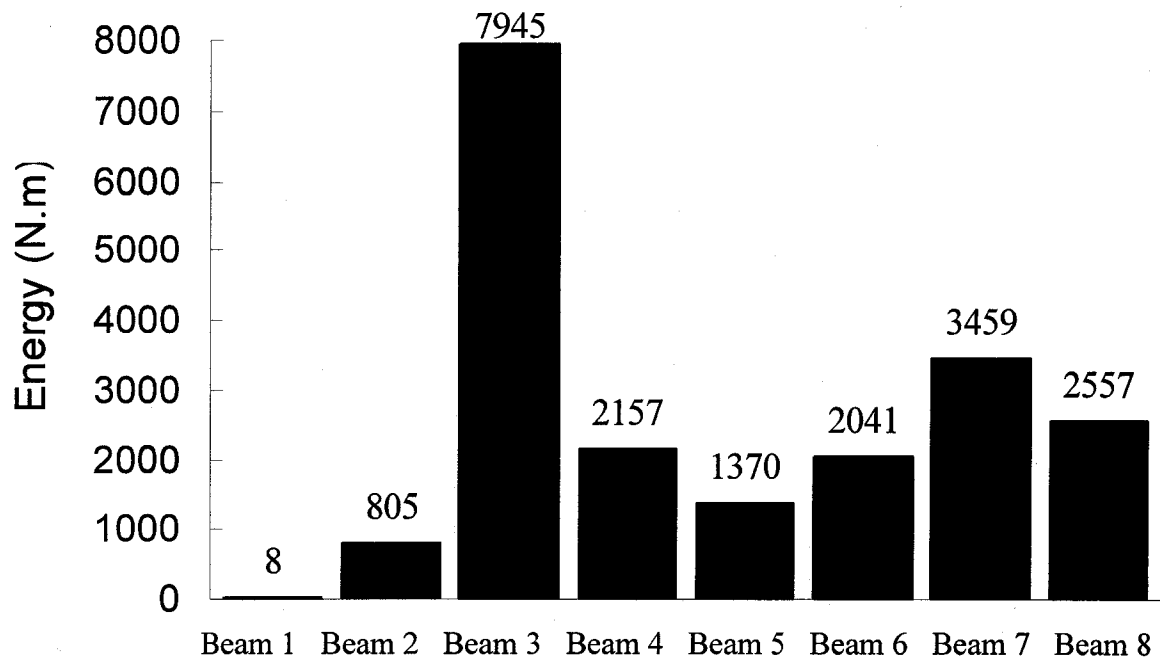


**Figure 5-5 Toughness of Specimens up to Peak Load**

## 6. SUMMARY, CONCLUSIONS AND RECOMMENDATIONS

### 6.1 Summary

The objective of this study was to investigate the flexural response of deep masonry beams strengthened with internal steel reinforcement and compare them with externally bonded Carbon Fibre Reinforced Polymer (CFRP) plates under a 3-point quasi-static loading. Whereupon, the feasibility of using externally bonded CFRP plates as an alternative to internal steel reinforcement to strengthen the constructed deep masonry lintels was evaluated.

Eight full-scale fully grouted deep masonry beam specimens were built and tested in the I.F. Morrison Structural Engineering Laboratory at the University of Alberta. A steel structural frame with a lateral bracing system was constructed to perform the vertical loading. For the sake of preventing CFRP plates from early debonding, a special anchorage system was assembled. All specimens possessed nearly identical geometric and material properties, and were tested under the same loading condition with Shear Span to Beam Span ratio  $a/l$  equal to 0.4.

Beam 1 served as the control beam and the other seven beams were enhanced with diverse strengthening schemes. Two main parameters namely, the amount and layout of reinforcing materials, were considered to investigate the behaviour of these specimens.

Based on the data collected, the behaviour of specimens was illustrated from several aspects, such as the relationship of load and mid-span displacement, strain behaviour of steel reinforcement and CFRP plates, system ductility, flexural & shear capacity, failure modes and crack patterns. Moreover, comparisons between specimens strengthened with different reinforcing strategies were carried out. At the end, four mechanical models were examined to compare the evaluation of load capacities for these specimens between predictions and test results.

### 6.2 Conclusions

According to the experimental results and analytical investigation, the following conclusions can be drawn:

The load-displacement response of masonry deep beams is similar to reinforced concrete deep beams. Furthermore, in conformity to test observations, the failure modes and crack patterns of masonry deep specimens are basically identified with reinforced concrete deep beams. Therefore, the overall behaviours of masonry deep beams can be analyzed using the Strut-and-Tie mechanical model. Nevertheless, the Strut-and-Tie model provided by CSA A23.3-04 was found to be very conservative to evaluate the shear capacity of masonry deep beams, especially, for the beams with web reinforcement.

The flexural and shear capacities of specimens were improved remarkably when the vertical web steel rebars or CFRP plates was employed. In addition, the system ductility of specimens was improved significantly as well.

Compared with the beams containing internal steel reinforcement only, use of externally bonded CFRP plates delayed the emergence of the first crack.

The load capacities of beams were improved significantly by using externally bonded CFRP plates.

Based on present test observations, delamination of CFRP laminates from underneath the masonry surface is the dominant failure mode for most CFRP strengthened beams. Consequently, it is necessary to provide adequate anchorage schemes at both ends of CFRP laminates.

Comparing the ductility of these specimens with each other indicates that the specimens strengthened with externally bonded CFRP plates possess less ductility than those strengthened with internal steel reinforcement.

Experimental results revealed that it is possible and practicable to use externally bonded CFRP plates to be an alternative of the internal steel reinforcement to retrofit the masonry deep beams. Also, this research provides valuable datum for future studies.

### **6.3 Recommendations**

The use of Carbon Fibre Reinforced Polymers in strengthening masonry structural members is a relatively new subject. Specifically, this research is the first in retrofitting masonry deep beams with only CFRP laminates. In order to acquire a better understanding of this topic, future study is required.

The high strength material used in this research was CFRP plates, whereas, for better understanding of the behaviour of masonry deep beams strengthened externally with high strength material, other forms of CFRP such as CFRP sheets and other type of laminates such as Glass Fiber and Aramid Fiber could act as the strengthening material to reinforce the masonry deep beams in future studies.

Based on present observations, delamination of CFRP laminates from underneath the masonry surface is the dominant failure mode for most of CFRP strengthened beams. Therefore, more research regarding stress distribution at the interface of masonry and laminate should be carried out.

Since the peeling-off and debonding are common premature failure modes for laminate strengthening schemes, the anchorage system should be taken good care of. Some related research needs to be conducted to assure that high strength materials can be brought into play fully.

It is well known that inclined web reinforcement can improve the shear capacity of reinforced concrete deep beams. But, there is a lack of variable layout of laminates on the web of masonry deep beams.

For evaluating the shear capacity of masonry deep beams, one of four mechanical models gives good predictions based only on test results of five specimens. Thus, more experimental data are required to verify the feasibility of this mechanical model.

## REFERENCES

1. ACI Committee 440. (2002) State-of the-Art Report on Fiber-Reinforced Plastic (FRP) Reinforcement for Concrete Structures (ACI 440R-96). American Concrete Institute, Farmington Hills, MI, 1996, P.65
2. Aguilar, Gerardo; B.Matamoros, Adolfo; J.Parra-Montesinos, Gustavo; A. Ramirez, Julio and K.Wight, James (2002). "Experimental Evaluation of Design Procedures for Shear Strength of Deep Reinforced Concrete Beams," AIC Structural Journal, Vol. 99, No. 4, July-August 2002, pp.539-548.
3. Aiello, M.A. and Sciolti, S.M. (2005). "Bond Analysis of Masonry Structures Strengthened with CFRP Sheets," Construction and Building materials 20 (2006) 90-100.
4. Albert, M.L.; Cheng, J.J.Roger. and Elwi, A.E. (1998). "Rehabilitation of Unreinforced Masonry Walls with Externally Applied Fiber Reinforced Polymers". Department of Civil & Environmental Engineering, University of Alberta, Edmonton.
5. American Society for Testing and Materials Standard D 3039/D 3039M-00(2000). "Standard Test Method for Tensile Properties of Polymer Matrix Composite Materials", American Society for Testing and materials, West Conshohocken, Pennsylvania.
6. American Society for Testing and Materials Standard C 1019-03 (2003). "Standard Test Method for Sampling and Testing Grout", American Society for Testing and Materials, West Conshohocken, Pennsylvania.
7. American Society for Testing and Materials Standard C 1552-03a (2004). "Standard Practice for Capping Concrete Masonry Units, Related Units and Masonry Prisms for Compression Testing", West Conshohocken, Pennsylvania.
8. American Society for Testing and Materials Standard C 140-03 (2003). "Standard Test Methods for Sampling and Testing Concrete Masonry Units and Related Units", West Conshohocken, Pennsylvania.
9. A23.3-04. "Design of Concrete Structures", Canadian Standards Association, 5060 Spectrum Way, Suite 100, Mississauga ON, Canada.
10. Bakir, P.G. and Boduroglu, H.M. (2005). "Mechanical Behaviour and Non-Linear Analysis of Short Beams Using Softened Truss and Direct Strut & Tie Models", Engineering Structures 27 (2005), pp.639-651.

11. Building Code Requirements for Masonry Structures (ACI 530-02/ASCE 5-02/TMS 402-02). ISBN 1-929081-13-8 (2002). Masonry Standards Joint Committee (MSJC).
12. Canadian Standard Association A165 Series-94 (1994). "CSA Standards on Concrete Masonry Units", Canadian Standards Association, Rexdale (Toronto), Ontario.
13. Chen, J.F. and Teng, J.G. (2001). "Anchorages Strength Models for FRP and Steel Plates Bonded to Concrete", *Journal of Structural Engineering*, Vol. 127, No. 7, July, 2001, pp. 784-786.
14. CIRIA. CIRIA Guide 2 (1977). *The Design of Deep Beams in Reinforced Concrete*. Construction Industry Research and Information Association, Ove Arup and Partners, London.
15. *Concrete Design Handbook, Second Edition* (1995), ISBN 1-896553-00-1, Cement Association of Canada, Ottawa, Ontario, Canada.
16. Foster, P.B; Gergely, J.; Young, D.T.; McGinley, W.M. and Corzo (2005), A. "FRP Repair Methods for Unreinforced Masonry Buildings Subject to Cyclic Loading". SP230: 7th International Symposium on Fiber-Reinforced (FRP) Polymer Reinforcement for Concrete Structures, pp289-306.
17. Glanville, John I.; hatzinikolas, Michale A. and Ben-Omran, Hamza A. (1996). "Engineering Masonry Design-Limit State Design", ISBN 1-55056-441-2, Winston House, Winnipeg.
18. Hsu, Thomas T.C. (1989). "Softened Truss Model Theory for Shear and Torsion", *ACI Structural Journal*, November-December, 1988, pp.624-635.
19. Hwang, Shyh-Jiann; Lu, Wen-Yao and Lee, Hung-Jen (2000). "Shear Strength Prediction for Deep Beams," *AIC Structural Journal*, Vol. 97, No. 8, May-June 2000, pp. 367-376.
20. Islam, M.R.; Mansur, M. A. and Maalej, M. (2002). "Shear Strengthening of RC Deep Beams Using Externally Bonded FRP Systems", *Cement & Concrete Composites* 27, pp. 413-420.
21. Kuzik, Marc D.; Elwi, Alaa E. and Cheng, J.J. Roger (1999). "Cyclic Behavior of Masonry Walls with GFRP", *Structural Engineering Report No. 228*, Department of Civil & Environmental Engineering, University of Alberta.
22. Lau, K.T.; Dutta, P.K.; Zhou, L.M. and Hui, D. (2001). "Mechanics of Bonds in an FRP Bonded Concrete Beam," *Composites: Part B* 32 (2001) 491-502.

23. Lorenzis, Laura De; Miller, Brian and Nanni Antonio (2001). "Bond of Fiber-Reinforced Polymer Laminates to Concrete," *ACI material Journal*, Vol. 98, No. 3, May-June 2001, pp. 256-264.
24. MacGregor, James G. and Bartlett, F.Michael (1988), "Reinforced Concrete-Mechanics and Design", First Canadian Edition, ISBN-0-13-101403-x. Scarborough, Ontario.
25. Magnusson, Bengt and Hervall, Arne (1984). "Strengthening Masonry Lintels," *Buiding Research & Practice*, vol. 12, No. 6, pp. 364-368.
26. Mau ST, Hsu TTC. (1989). Formula for The Shear Strength of Deep Beams. *ACI Structural Journal*, 1989; 86(5): 516-23.
27. Miao, Honglan; Cheng, J.J.Roger and Elwi, Alaa (2005). "CFRP Sheets Application to Masonry Shear Walls with Openings", Department of Civil & Environmental Engineering, University of Alberta, Edmonton.
28. Narayanan, R. and Darwish, I. Y. S. (1988). "Fiber Concrete Deep Beams in Shear", *ACI Structural Journal*, March-April 1988, pp.141-149.
29. Russo, Gaetano; Venir, Raffaele and Pauletta, Margherita (2005). "Reinforced Concrete Deep Beams-Shear Strength Model and Design Formula," *ACI Structural Journal*, Vol. 102, No. 3, may-June 2005, pp. 429-437.
30. S304.1-94. "Masonry Design for Buildings (Limit States Design)", Canadian Standards Association, Etobicoke, Ontario, Canada.
31. Tan, Kang-Hai; Kong, Fung-Kew; Teng, Susanto and Guan, Lingwei (1995). "High-Strength Concrete Deep Beams with Effective Spanand Shear Span Variations", *ACI Structural Journal*, July-August, 1995, pp. 395-405.
32. Tan, K.H.; Patoary, M.K.H. and Roger, C.S.K. (2003). "Anchorage Systems for Masonry Walls Strengthened with FRP Composite Laminates", *Journal of Reinforced Plastics and Composites*, Vol. 22, No. 15, 2003, pp. 1353-1371.
33. Tan, Kang-Hai; Teng, Susanto; Kong, Fung-Kew and Lu, Hai-Yun (1997). "Main Tension Steel in High Strength Concrete Deep and Short Beams", *ACI Structural Journal*, November-December, 1997, pp. 752-768.
34. Tang, C.Y., A.ASCE and Tan, K.H., M.ASCE (2004). "Interactive Mechanical Model for Shear Strength of Deep Beams," *Journal of Structural Engineering*, ASCE, Vol. 130, No. 10, October 1, 2004, pp. 1534-1544.
35. Wabo<sup>®</sup>Mbrace Composite Strengthening System with Carbon Fiber Reinforcement (2002). Watson Bowman Acme.

36. Xiong, G.J.; Ma, X. and Ji, Z. (2006). "Effect of Contact Pressure on Bond Strength of Fiber-Reinforced Polymer to Concrete", *Journal of Composites for Construction*, Vol. 10, No. 3, June 1, 2006, pp.275-278.
37. Yao, J.; Teng, J.G. and Chen, J.F. (2005). "Experimental Study on FRP-to-Concrete Bonded Joints", *Composites: Part B: Engineering* 36 (2005), pp. 99-113.
38. Yao, J.; Teng, J.G. and Lam, L. (2005). "Experimental Study on Intermediate Crack Debonding in FRP-Strengthened RC Flexural Members," *Advances in Structural Engineering*, Vol. 8, No. 4, pp.365-395.
39. Zhang, Zhichao; Hsu, Cheng-Tzu Thomas and Moren, Jon (2004). "Shear Strengthening of Reinforced Concrete Deep Beams Using Carbon Fiber Reinforced Polymer Laminates," *Journal of Composites of Construction*, ASCE, Vol. 8, No. 5, October 1, 2004, pp. 403-414.